INSTITUTE OF EXPERIMENTAL PHYSICS
DEPARTMENT OF PHYSICS
WARSAW UNIVERSITY

Computational modeling of epileptic seizures in the brain

by

Damiano Gentiletti

Advisor

Prof. Piotr Suffczyński

FEBRUARY 2022

Acknowledgments

I would like to thank my advisor, prof. Piotr Suffczyński, who accepted me as an intern in his lab, entrusted me with this project and devoted a high amount of time to our collaboration. I am deeply grateful for his patience throughout this journey, his immutably positive attitude, as well as the inspiring conversations we have been having, not only around science.

My acknowledgments to dr. Marco de Curtis and dr. Vadym Gnatkovsky from the Carlo Besta Neurological Institute in Milan: without their insight into the problem of human epilepsy, openness to share invaluable experimental data, and trust in computational models this work would not have been possible.

When I joined the Biomedical Physics Division at Warsaw University I was welcomed very warmly by prof. Jarosław Żygierewicz's team, who made me feel like I was part of their group since the very beginning. I am especially thankful to Marysia for her wisdom, emotional support and big heart.

I would like to wholeheartedly thank my loving Mother, who since my early age presented me education as a worthwhile endevour and encouraged me to pursue my passions without reserve, and my Father, for instilling in me the values of hard work, integrity and determination.

My appreciation also goes out to my friends Claudia, Valeria and Marcin, who have always been so close and supportive both in difficult and happy times: I feel blessed for all the beautiful moments shared with them and for the many more ahead.

Finally, my gratitude to Łukasz, for offering constant encouragement and understanding and for his precious presence in my life.

Abstract

In this work the problem of epileptic seizure generation, progression and termination is addressed from a computational perspective. Two computational models are introduced, discussed and analyzed, aimed to reproduce the experimental data recorded in the entorhinal cortex of the *in vitro* guinea pig brain. This preparation is considered to be a valid reference model of human focal epilepsy. The goal is to shed light into the pathological mechanisms responsible for the occurrence, evolution and cessation of focal epileptic seizures. In particular, the traditional view according to which epilepsy is caused by a chain reaction of synaptic excitation is challenged. Alternative hypotheses of epileptogenesis are presented and tested by means of computer simulations. Emphasis is put on the role of non-synaptic mechanisms (i.e., mechanisms independent of synaptic transmission) and intra- and extracellular concentration dynamics of K^+, Na^+, Ca^{2+}, and Cl^- ions. Simulations results confirm the experimentally driven supposition that inhibition prevails on excitation at the outbreak of epileptic episodes, and prove that ion concentration changes shape the different phases of a focal seizure. A novel antiepileptic therapy is also investigated, presenting a potentially feasible strategy leading to successful seizure control.

Abstrakt

Niniejsza Rozprawa porusza problem generacji napadów padaczkowych z perspektywy obliczeniowej. W Rozprawie opisano i przeanalizowano dwa realistyczne modele komputerowe mające na celu odtworzenie eksperymentalnych napadów padaczkowych zarejestrowanych w korze śródwęchowej mózgu świnki morskiej *in vitro*. Preparat ten jest uważany za ważny model zwierzęcy padaczki ogniskowej u ludzi. Celem Rozprawy było lepsze zrozumienie patologicznych mechanizmów odpowiedzialnych za inicjację, ewolucję i zanikanie ogniskowych napadów padaczkowych. W szczególności, w Rozprawie kwestionowany jest tradycyjny pogląd, zgodnie z którym padaczkę wywołuje reakcja łańcuchowa w synaptycznie połączonej sieci neuronów pobudzających. Za pomocą symulacji komputerowych testowane są alternatywne hipotezy dotyczące mechanizmów napadów padaczkowych, w których dominującą role odgrywają mechanizmy niesynaptyczne (tj. mechanizmy niezależne od transmisji synaptycznej) np. dynamika stężeń wewnątrz- i zewnątrzkomórkowych jonów K^+, Na^+, Ca^{2+} i Cl^-. Wyniki symulacji potwierdzają eksperymentalnie poparte przypuszczenie, że w momencie wybuchu napadu padaczkowego, paradoksalnie, przeważa aktywność neuronów hamujących i dowodzą, że zmiany stężenia jonów kształtują różne fazy napadu ogniskowego. W oparciu o model zaproponowana jest również nowa terapia antynapadowa polegająca na regulacji stężenia jonów w otoczeniu neuronów i przywracająca układ do stanu równowagi.

Contents

List of Figures

List of Tables

Chapter 1

Introduction

1.1 The nervous system

The highest mental activities and behavioral characteristic of humans, such as learning, language and the perception of emotions, are mediated by the nervous system: thanks to this intricate collection of interacting biological structures we are able to move, think, remember, learn, speak and feel. In vertebrate species the nervous system is made up of two main parts: the central nervous system (CNS) and the peripheral nervous system (PNS). The CNS contains the brain and the spinal cord, and it is so named because it coordinates and influences the activity of all parts of the body. The brain is the major functional unit of the central nervous system; at the cellular level it is composed by a special type of cell, called neuron. The function of neurons is to send electrical signals – the action potentials – to other neurons located in the same or in a different brain region, and to receive feedback from them. The communication between neurons is made possible by specific biological complexes called synapses. Malfunction of the brain and of other nervous system components can be caused by different factors, such as genetic defects, physical damage, infection or ageing.

We can be motivated to deepen our knowledge of the nervous system, and the brain in particular, for a variety of reasons. First, the human brain is an enigmatic organ and it is considered to be the most complex dynamic object in the universe. This makes it an inexhaustible source of wonder, not only for the scientific community but for anyone who is fascinated by the world surroundig them. We can also be driven by an urge to understand and justify human actions, or to predict individuals' reactions in different contexts. Finally, by broadening our knowledge of the brain we can gain deeper insight into its pathological behavior and explain the origin and advancement of many nervous diseases, such as epilepsy. This may ultimately lead to the development of therapeutic strategies allowing treatment of the pathological conditions.

1.2 Epilepsy

Epilepsy is one of the most common cerebral diseases. This is evident from the graph in Fig. 1.1, which illustrates the estimated number of U.S. residents suffering from some of the main neurological disorders: epilepsy ranks 3rd in terms of incidence. As a brain pathology, epilepsy is characterized by *epileptic seizures*. An epileptic seizure has been defined as a brief episode of signs or symptoms due to abnormal excessive or synchronous neuronal activity in the brain (Fisher, 2005 [1]). Epilepsy has afflicted humankind since early history. In ancient times it was referred to as the "sacred illness" [2], and was associated in the Greek mythology with the moon goddesses Selene and Artemis, who punished those who upset them by inflicting the disease. It was later on believed to be a form of demonic possession, which led to social persecution and stigma of the affected subjects. Only in the 19th century did epilepsy cease to be perceived as a "disorder of the spirit" and started to be recognized as a physical condition.

Epileptic seizures are classified based on their physical localization in the brain: they are called *focal*, if the source from which they originate is restricted to a particular brain region, or *generalized* if the source is spread over different cerebral areas. Seizures can manifest through different symptoms: a patient experiencing an attack may cry out, fall to the floor unconscious, move uncontrollably, or drool. Seizures often end by rhythmic body jerks at decreasing frequency, which are related to the decreased interburst interval (IBI), as will be shown in Chapter 4. When the seizure is over, the subject regains consciousness but feels exhausted and dazed. The symptoms described are characteristic

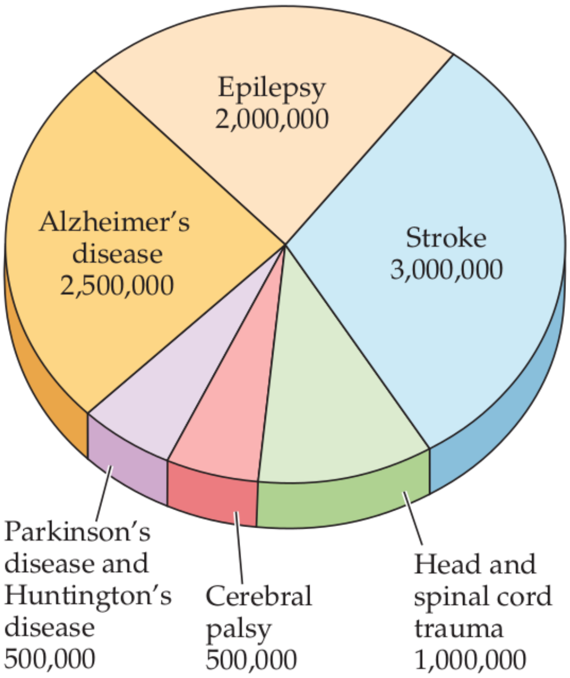

Figure 1.1: Incidence of the major brain disorders in the U.S. (data from Hirtz et al., 2007 [3].). Epilepsy ranks 3rd in terms of incidence.

of a particular kind of epileptic seizures, named *tonic-clonic* seizures, and are most commonly associated to epilepsy. Nevertheless, this is only one of the possible clinical scenarios, and different seizures may be associated to a different set of symptoms. Epilepsy cannot usually be cured, but medication can control seizures effectively in about 70% of the cases [4]. The remaining portion of epileptic cases is represented by subjects who will continue to experience seizures even with the best available treatments. This condition is referred to as *intractable epilepsy*.

Fig. 1.2b shows a sample of electrical activity in the brain during a human focal seizure (Truccolo, 2011 [5]) recorded by means of microelectrodes implanted in the participant's brain and localized in the three points marked in Fig. 1.2a by yellow circles (single "ECoG" electrodes) and red square (microelectrode array). The trace named "LPF" (*local field potential*) is recorded by the microelectrode array, and results from the sum of the electrical currents flowing from multiple neurons nearby the red square. The local field potential spectrogram is shown in the bottom panel. Seizure starts at time 0 ms, as indicated by the red vertical line.

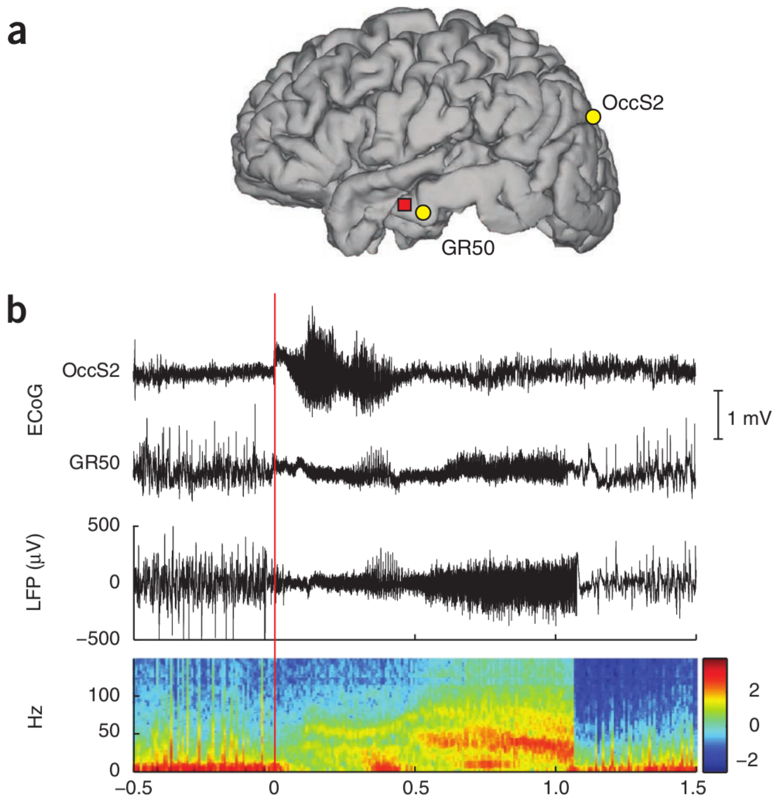

Figure 1.2: Example of electrical activity observed in the human brain during focal epilepsy. Panel a: position of the microelectrodes used for the recordings in the participant's brain. The yellow circles represent single electrodes, while the red square indicates the microelectrode array for local field potential measurement. Panel b: single "ECoG" electrodes and LFP voltage traces and LFP frequencies spectrum. Time (horizontal axis) is expressed in seconds. Source: Truccolo et al., 2011 [5].

1.2.1 Traditional view on epileptogenesis

"Epileptogenesis" is the process through which a normal brain develops epilepsy. Traditionally, epileptic seizures are thought to be initiated by a reinforcement of excitation coupled with a decrease of inhibition in the brain neuronal networks. This concept is well illustrated in Fig. 1.3. The blue links between distinct neuronal cells indicate excitatory connections, while the red line is a single inhibitory connection. In the scenario represented in the left panel the excitatory and inhibitory forces balance out and no seizure is generated. However, when excitation prevails on inhibition as in the right panel (thicker blue line versus thinner red line), equilibrium is disrupted and epileptic discharges can develop. A possible chain of events matching the excitation/inhibition imbalance concept is shown in Fig. 1.4A. A pyramidal neuron (excitatory cell) is synaptically connected to other cells of the same type. When the pyramidal

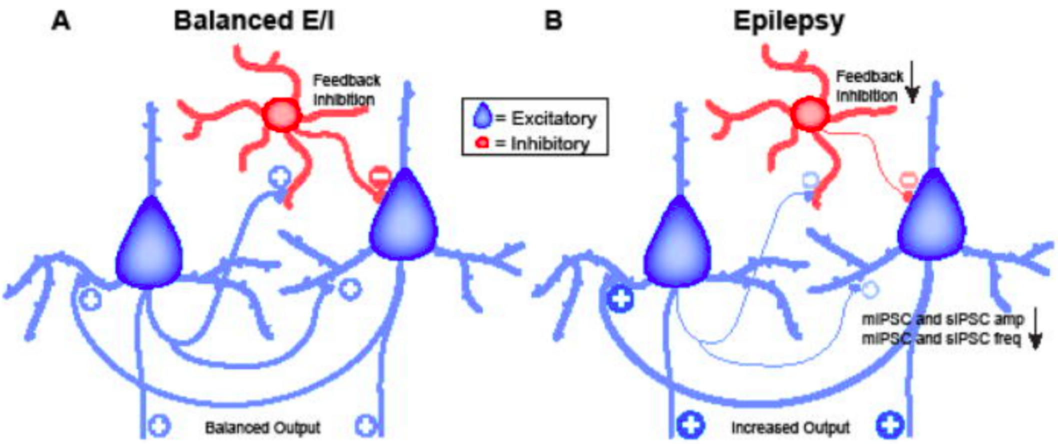

Figure 1.3: According to the traditional view, epilepsy is caused by an alteration of the excitation/inhibition balance in brain neuronal networks. Panel A: the balance between excitation (blue line) and inhibition (red line) is preserved and no seizure is generated. Panel B: the loss of equilibrium in favour of excitation (thicker blue line versus thinner red line) may result in the development of an epileptic discharge. Source: Tatti et al., 2017 [7].

neuron starts firing, provided that the output stimulation is large enough to trigger a response, the neighbouring neurons are also excited (1.4B). Each of these cells in turn activates its targets, resulting in the recruitment of a large network (1.4C). The population pattern can then evolve into synchronous firing, a condition which is typically associated with epileptic seizures. The sequence of events here described reminds of a chain reaction. As pointed out by Jefferys et al. in [6], such mechanism needs a minimal number of cells to produce an epileptic seizure: if the initial population is not large enough, the successful recruitment of the majority of neurons into firing is not guaranteed.

1.2.2 Challenges to the traditional view

Whether the traditional view reflects the real mechanisms leading to the manifestation of epileptic seizures has never been proved. On the contrary, it has been shown that seizure-like discharges may occur even in the absence of synaptic transmission ([8]; [9]; [10]). Fig. 1.5 shows a striking example of non-synaptic epileptic activity ([11]): the electrical signal was recorded from a rat hippocampal slice put in a solution containing calcium in low concentration. Under such conditions synaptic transmission is blocked, being calcium ions necessary for the normal functioning of synapses [12]. Interestingly, despite

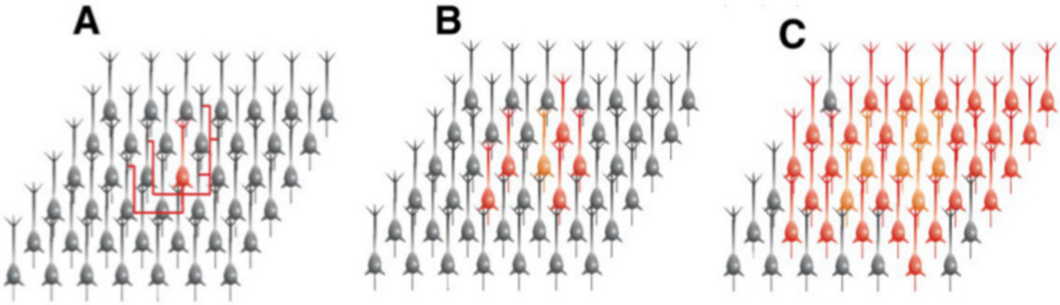

Figure 1.4: Possible chain of events leading to epileptic discharges in a neuronal network. Panel A: a pyramidal cell is connected to other neurons of the same kind by means of excitatory synapses. Panel B: if the output stimulation received from the first cell exceeds the firing threshold, target neurons are also activated. Panel C: excitatory cells are progressively recruited into epileptic activity and the discharge propagates. Source: Jefferys et al., 2012 [6].

the lack of direct communication between cells, the development of seizure-like activity was observed in the slice. Synaptic transmission is therefore not essential for epileptogenesis.

Synaptic connections have also been shown not to be strictly necessary for the spatial propagation of epileptic discharges. This has been demonstrated experimentally by Durand et al. [13] in 2010 with the procedure outlined in Fig. 1.6. Epileptic seizures were induced on a rat hippocampal slice by means of a low-calcium solution. Electrical activity was then measured in two different sites of the slice by means of electrodes, and the cross-variance between the signals evaluated. As shown in the top panel, signal correlation indicates a high degree of synchrony between the two sites. The slice was subsequently cut in two parts, producing a mechanical lesion separating the recording sites and resulting in the disruption of synaptic transmission. Despite the physical removal of connections, the signals were still synchronized to some extent (panel b) as long as the two portions were kept close to each other. When the two regions were put apart (panel c), synchrony among the signals was lost. Surprisingly, successive repositioning of the two synaptically-disconnected parts side by side restored synchrony (bottom panel). This result proves that synaptic transmission is not required for epileptic seizures propagation between areas. Hence, there must exist mechanisms of different origin allowing for seizure discharges

Figure 1.5: Seizure-like activity generated in a rat hippocampal slice put in a low-Ca^{2+} solution. Despite the block of synaptic transmission, epileptic discharges occurred, pointing to the potential role of non-synaptic mechanisms in epileptogenesis. Source: Haas et al., 1984 [11].

to spread and synchronize across the brain tissue. A possible form of communication within the nervous system distinct from synaptic transmission is represented by the so called *ephaptic coupling* (from the Greek term "ephapsis", "to touch"), which is based on the idea that adjacent ("touching") nerve cells may communicate through the exchange of ions or local electric fields [14]. Following this line of thinking, Zhang et al. [15] have demonstrated in 2014 that interactions between nerve cells mediated by electric fields are in fact sufficient to entail the propagation of epileptiform activity. As will be later shown in this work, exchanges between neurons may also originate from ion fluxes spreading through the extracellular medium surrounding them.

1.3 Computational neuroscience

One of the possible approaches to the study of the nervous system's physiological and pathological behavior is represented by computational neuroscience. The goal of this discipline is to investigate the processes taking place in the nervous system components using mathematical models and theoretical analysis. As an interdisciplinary science, it attempts to build a bridge between neuroscience and computer science, mathematics, and physics. The impulse to develop computational neuroscience was given in 1952 by the research work of Hodgkin and Huxley [16], which aimed to describe the genesis and propagation of the action potential in the squid giant axon through mathematical techniques. The methods Hodgkin and Huxley employed set the basis for future advances and inspired many other mathematical representations of neurobiological mechanisms. Nowadays computational models are used to study the

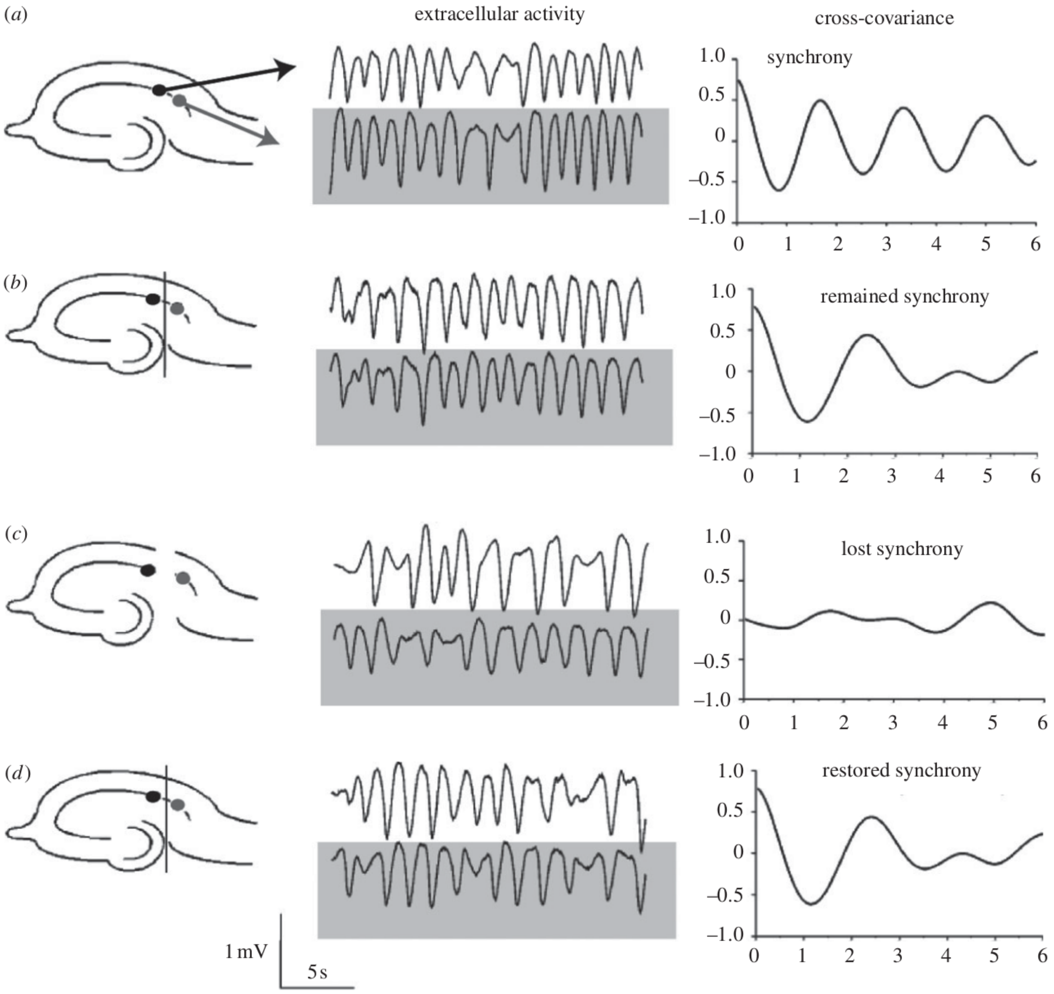

Figure 1.6: Synchrony of epileptiform activity across a mechanical lesion. The activity is induced on the rat hippocampal slice by means of a low-calcium solution and is recorded at two different sites. (a) Before the cut: a high degree of synchrony between the signals is observed. (b) A mechanical cut is made separating the recording sites, synaptic connections between the cells are disrupted. The signals are still synchronized to some degree when the portions are kept close to each other. (c) The two regions are put apart, synchrony is lost. (d) After repositioning the two parts side by side, synchrony is restored. Source: Durand et al., 2010 [13].

activity of a large number of neuronal structures, and provide invaluable support in understanding both normal and altered brain conditions. In particular, computational models are useful because:

- They can support theories based on data. Realistic simulations of anatomical functions can be performed in order to either confirm or deny experimental hypotheses.
- They can facilitate the interpretation of experimental data and be helpful to predict the system's evolution and behaviors.

- They allow to isolate single components and to study their activity independently of the rest of the system. This kind of analysis is often necessary to uncover the real mechanisms governing biological phenomena.

- The limitations imposed by physical reality may in some cases hamper or impede the realization of certain experiments. In such situations, computational models mimicking the original setup can be implemented to eliminate the constraints and create a virtual environment in which the experiments can be simulated.

1.3.1 Modeling approaches

It is possible to distinguish between different approaches to computational modeling in neuroscience. For single cells, a possible technique consists of dividing the concept neuron into a finite number of interconnected anatomical compartments (e.g. [17]). The behavior of each compartment is then described by an approppriate set of differential equations. Although morphologically accurate, such a method can be computationally demanding if the total number of compartments is elevated. Model cells tend therefore to be heavily simplified and reduced to single-compartment representations in which just one macroscopic cylinder approximates the whole neuron (e.g. [18]). Single-compartment models are easily generalizable and very useful to build populations of interacting cells; their overly simplified structure, however, does not allow to recreate the real spatial distribution of crucial physical quantities, such as ion conductances. A third approach is represented by *lumped models*, which are used to simulate large neuronal networks. The idea behind lumped modeling is to simplify the description of the global network by considering only a certain number of discrete entities, belonging to the network itself and approximating its behavior. A lumped neuronal model does not recreate single cells, but subpopulations of neurons of a given type believed to carry the main properties of the whole system. The computational model implemented by Jansen and Rit in [19] to simulate a cortical neuronal population is an example of lumped model.

1.4 Motivation of this work

A better comprehension of the factors regulating seizure outburst, progression and termination might help to define new therapeutic strategies for drug-resistant epileptic patients. Unfortunately, both the complexity of the brain's structure and the practical challenges connected to gathering real, accurate data from patients make the task of investigating the processes governing seizure-like events very difficult to accomplish. To the best of the author's knowledge, to this day no clinical techniques nor mathematical model have been successful in unraveling the misteries of epilepsy. Nevertheless, the substantial relevance of new experimental findings on epileptogenesis supports and motivates an urge of exploring synaptic and non-synaptic mechanisms more in depth.

In an attempt to shed light on the real causes of epilepsy, a number of computational models have been developed [20]. A common feature to most of the representations is the assumption that intra- and extracellular ion concentrations are constant both in time and space. Although this choice may be justified by the sake of simplicity, it does not necessarily reflect the reality. It has indeed been shown that ion concentrations can remarkably deviate from their baseline levels during periods of increased neuronal discharges, such as epileptic seizures (Raimondo et al., 2015 [21]). Ion concentration fluctuations can significantly impact a number of neuronal processes. In particular, changes in the extracellular K^+ concentration have been directly correlated with the occurrence of epileptic seizures (Frohlich et al., 2008 [22]). According to the "potassium accumulation hypothesis", proposed by Fertziger and Ranck in 1970 [23], intense neuronal discharges elevate the extracellular K^+ concentration, thus reducing potassium currents that hyperpolarize the cells membrane potential. This in turn increments neuronal firing, causing a further increase in the emission of K^+ into the extracellular space. Such a positive feedback mechanism has been suggested to play a major role in seizures generation.

To demonstrate the importance of ion concentration fluctuations in epilepsy, a large amount of experimental data on ion dynamics associated with seizure activity has been accumulated. Surprisingly such findings are usually not reproduced via ion dynamics incorporation into computational models, with few notable exceptions, e.g., Durand and Park, 2005 [24], Kager et al., 2008 [25], Krishnan and Bazhenov, 2011 [26], Wei et al., 2014 [27]. These highly realistic representations have been successful in convincingly proving the impact of ion concentrations changes on epileptic behavior. However, seizure patterns associated with ion dynamics observed in different models may be not homogenous and dependent on the specific model settings, which makes the results difficult to generalize.

The aim of the present work is to delve into the role of ion concentration dynamics in epileptic seizure generation, progression and termination. This is accomplished with the aid of two computational models reproducing the epileptic behavior observed in the entorhinal cortex of the *in vitro* isolated guinea pig brain [28], an experimental preparation considered to be a valid animal model of human focal epilepsy. Both models incorporate a number of ion dynamics mechanisms recreating biological processes. Simulation results are compared to the experimental traces and ion contributions to epileptic activity and its termination are discussed. The hypothesis that at seizure onset inhibitory networks activity prevails on excitation is also tested through the models.

The two computational models here presented are of increasing complexity. The simpler model is made up of just two neurons: an inhibitory interneuron and an excitatory pyramidal cell. The neurons communicate with each other by exchanging ions through a common extracellular space. Despite its topological simplicity, the model can recreate seizure patterns strongly resembling those observed in the *in vitro* guinea pig brain. Epileptic discharges, however, involve large populations of interacting neurons which may exhibit synchronous activity. This behavior cannot be captured by a reduced model consisting of two representative units [29], motivating therefore the realization of a second, more complex, application. Such an extended model incorporates four pyramidal cells and one interneuron, to reflect the fact that in hippocampal circuits interneurons are present in lower number than principal cells [30]. Each cell is endowed with multiple intra- and extracellular compartments and ion dynamics is implemented. Following the same approach adopted by Durand et al. in [13], exchange of ions between extracellular spaces is modeled. Additional features not present in the first version are included in the extended setup, which is thus able to simulate a virtual environment more resemblant to the real one. Both models have been implemented using the NEURON simulator and the NMODL framework.

1.5 Thesis structure

Following the introduction, in Chapter 2 the *in vitro* isolated guinea pig brain preparation and the experimental traces serving as biological reference for the developed computational models are described in detail. The computational models are presented in Chapter 3 (minimal model) and Chapter 4 (extended model). Simulation results are compared to the experimental data and discussed. In Chapter 4 a potential strategy to control seizures is tested. Chapter 5 elaborates on the models limitations and summarizes the main insights gained from the study; possible future computational extensions are also suggested.

Chapter 2

Experimental data and hypothesis

The *in vitro* isolated guinea pig brain (shown in Fig. 2.1) is an experimental preparation employed at the Istituto Neurologico Carlo Besta of Milan, Italy. Seizure-like discharges mimicking seizure patterns in humans are induced in the entorhinal cortex (EC) through the application of *proconvulsant drugs* (i.e., drugs leading to epileptic seizures), such as bicuculline ([31], [32]). Intra- and extracellular voltages and extracellular potassium concentration are then recorded and data is collected.

2.1 The *in vitro* isolated guinea pig brain

To obtain the experimental model young adult guinea pigs are first anesthetized with sodium thiopental, the heart is exposed, and the animal is perfused through the ascending aorta with a saline solution. The brain is then carefully dissected out under hypothermic conditions and placed in an incubation/recording chamber. The extracellular electrical activity is recorded from the medial EC with glass pipettes. Intracellular recordings are performed with sharp electrodes. The signals obtained are amplified by means of a multichannel differential amplifier and an intracellular amplifier. The extracellular potassium concentration is recorded using ion-selective electrodes. Bicuculline methiodide is arterially perfused to induce seizure activity. The experimental protocol is approved by the Ethics Committee on Animal Care at the Istituto Neurologico Carlo Besta. Every effort to reduce both animal suffering and the number of

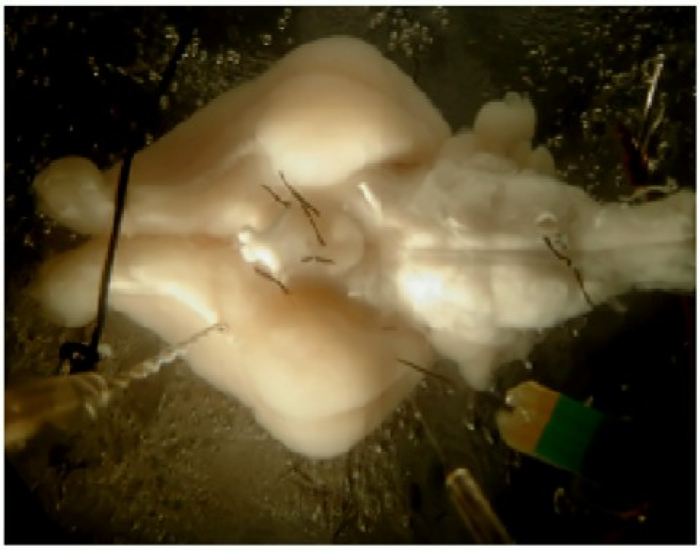

Figure 2.1: The *in vitro* isolated guinea pig brain employed at the Istituto Neurologico Carlo Besta of Milan, Italy. Intracellular voltage and extracellular potassium concentration traces are recorded in the entorhinal cortex during periods of induced epileptic activity. Seizures are induced by arterial perfusion of bicuculline methiodide, which has a proconvulsant effect. Image courtesy of Marco de Curtis, Istituto Neurologico Carlo Besta.

animals used is made. For more details about the methods employed to isolate the guinea pig brain, see: De Curtis et al., 1991 [33]; De Curtis et al., 1998 [34]; Muhlethaler et al., 1993 [35]; Gnatkovsky et al., 2008 [28]; Trombin et al., 2011 [36].

The most important advantage of *in vitro* isolated guinea pig brain over other *ex vivo* models, such as brain slices, is perhaps represented by its "in toto" nature: the entire brain, carefully removed and perfused via the vascular system, not only contains more intact neuronal connections, but preserves nearly complete connectivity in both local and long-range neuronal networks [37]. This allows the study of epileptic activity under circumstances much closer to the *in vivo* situation and with complete experimental access to the brain. Recordings with the same degree of accuracy would be very difficult to obtain from a living animal, since artifacts caused by mechanical movements would severely hamper data quality.

It has been observed that the seizure-like discharges induced in the experimental preparation closely resemble the activity seen in human focal epilepsy [38]. Fig. 2.2 shows a comparison of the LFP signal recorded during focal

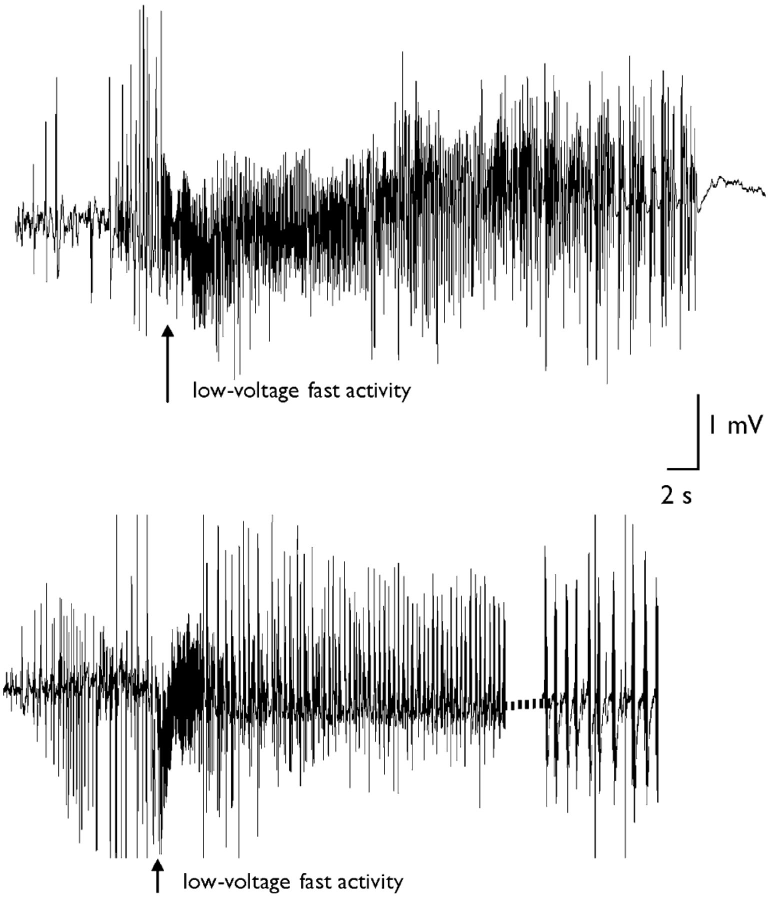

Figure 2.2: Human focal epilepsy recordings (top panel) are compared to experimental seizure recordings in the isolated guinea pig brain (bottom panel). In both cases, low-voltage fast activity characterizes seizure onset. The similarity shared by the traces suggests that the *in toto* brain preparation can be used as a valid model of human focal epilepsy. Source: De Curtis et al., 2009 [38].

seizures in the hippocampus of a patient with temporal lobe epilepsy (upper trace) and in the hippocampus of the *in vitro* isolated guinea pig brain (bottom trace). Strikingly, the seizure-like event induced in the preparation closely replicates human epileptic activity, hence justifying the validity of the *in toto* brain as a model of human focal epilepsy.

2.2 Seizure-like events *in vitro*

Experimental evidence suggests that seizures induced in the *in vitro* guinea pig brain EC evolve in time following a specific pattern (De Curtis et al., [38], and Gnatkovsky et al., [28]). This is depicted in Fig. 2.3, which shows the LFP signal (second panel from top), as well as intracellular voltage traces recorded

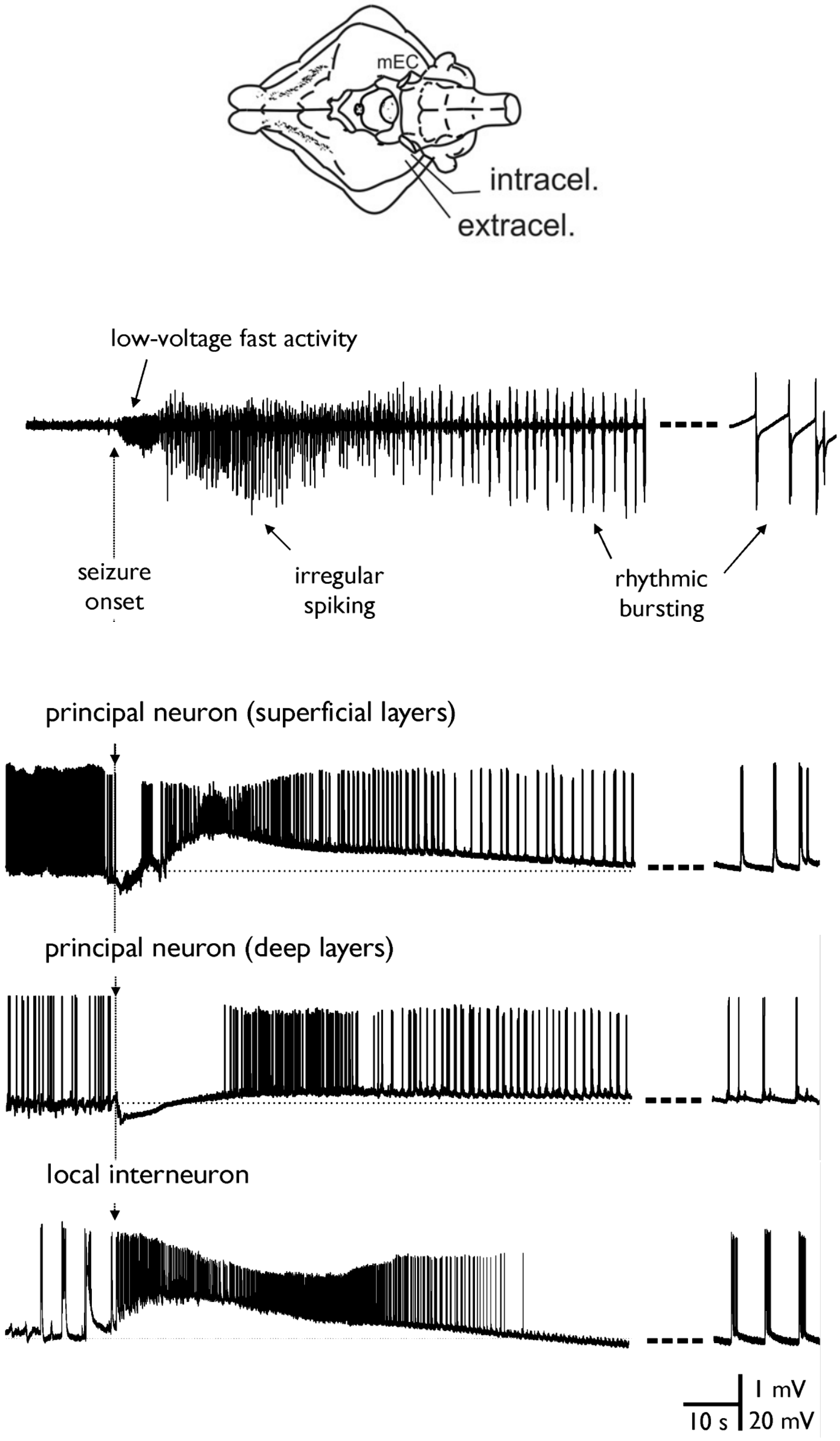

Figure 2.3: Experimental traces recorded in the entorhinal cortex of the *in vitro* isolated guinea pig brain. Top panel: schematic representation of the *in toto* brain showing the position of the intra- and extracellular electrodes in the medial part of the EC (mEC). Middle panels: LFP signal and intracellular voltage traces of two pyramidal cells in the superficial and deep EC layers. Bottom panel: intracellular voltage trace of a local interneuron. Seizure onset is associated with increased firing of the interneuron and transient cessation of activity in the pyramidal cells. Subsequently, principal cells resume tonic spiking, that progressively transforms into bursting. Source: Trombin et al., 2011 [36] (*in toto* brain representation); De Curtis et al., 2009 [38] (experimental traces).

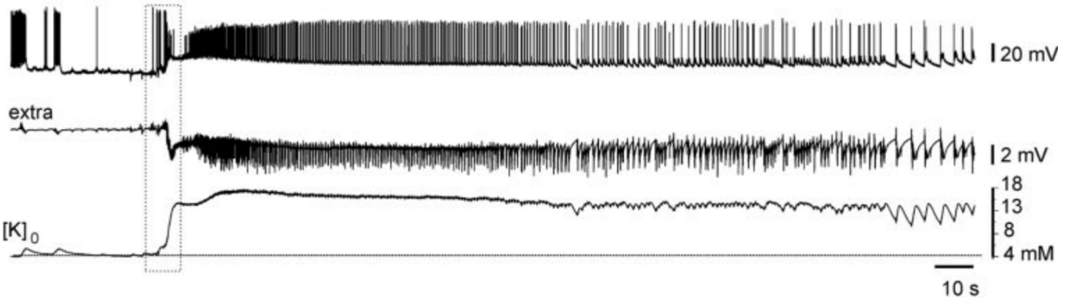

Figure 2.4: Simultaneous recordings of a principal neuron in superficial layers (top trace), LFP signal (here labelled as “extra”, standing for “extracellular potential”, middle trace), and changes in extracellular K^+ concentration during a seizure-like event in the guinea pig brain. At seizure onset (outlined by the dashed box) the extracellular potassium concentration rises sharply and remains high throughout the whole duration of the event. Source: Gnatkovsky et al., 2008 [28].

from an inhibitory interneuron (bottom panel) and two pyramidal cells in the EC superficial and deep layers (middle panels). Seizure onset is characterized by strong firing of the interneuron, coupled with the total absence of activity in pyramidal cells. As introduced in Chapter 1, this is in net contrast with the traditional view, which ascribes the main cause of epileptic discharges to a prevalence of excitation over inhibition. On the contrary, in the *in toto* preparation it is inhibition to be reinforced at seizure onset, and the intense firing of the interneuron inhibites principal excitatory neurons, which become silent for some time. Simultaneously, the extracellular potassium concentration sharply increases with respect to its baseline level (Fig. 2.4). These changes correlate with low-voltage fast oscillations (20–30 Hz) in the LFP signal. The elevated level of potassium concentration in the common extracellular space makes in turn pyramidal cells more excitable, and within a few seconds they resume firing, leading to a transient phase of enhanced neuronal excitation referred to as *irregular spiking* (the relation between extracellular potassium concentration and neuronal excitability is examined in Section 2.3). As the seizure progresses, clearance mechanisms (described in detail in subsequent chapters) start acting on extracellular potassium, causing the potassium concentration to slightly decrease and spiking activity to slow down in all cells. Later on during the epileptic event tonic firing undergoes a transition towards the *rhythmic bursting* pattern. This is coupled with neuronal activity synchronization and, eventually, seizure termination. The full sequence of events is summarized in

Fig. 2.5.

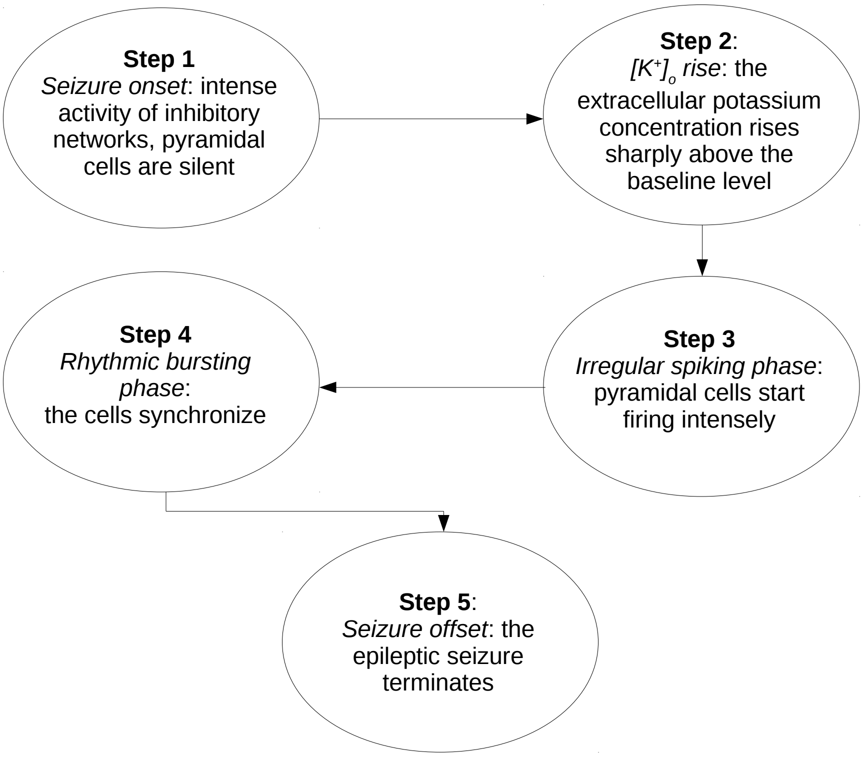

Figure 2.5: The hypothetical chain of events taking place during seizures-like events in the *in vitro* isolated guinea pig brain.

2.2.1 Data for this study

The experimental data considered in this thesis is shown in Fig. 2.6. The sample voltage and extracellular potassium traces were obtained during three different experiment realizations (32 total repetitions). A total number of 30 principal neurons (24 in EC superficial layers II to III and 6 in deep layers V to VI) and 10 interneurons located in the superficial (500 μm) EC were employed in the full experiment, as described in Gnatkovsky et al., 2008 [28]. The cells were identified from their response to a hippocampal input driven by stimulation of the olfactory area. Thirteen of the 30 principal cells were further morphologically identified as stellate or pyramidal cells. Bicuculline methiodide (50 μM) was arterially perfused for 3 min to induce seizure activity in the preparation. Ictal (i.e., epileptic) events typically initiated with fast activity at 20 to 30 Hz in LFP signals (27 out of 32 experimental trials). All trials were performed at a temperature of 32 ^{o}C.

The recorded epileptic episode follows the pattern described above: seizure onset is associated with cessation of activity in the selected principal cell (Fig. 2.6, top panel) and increased firing of the sample interneuron (Fig. 2.6, middle panel). Subsequently, the pyramidal cell resumes its activity, which gradually changes into firing of bursts as the seizure progresses. The recorded extracellular K^+ concentration (Fig. 2.6, bottom panel) increases rapidly at the beginning of the fast interneuronal discharge and remains elevated throughout the course of the seizure. The strong preictal firing in the pyramidal cell (second 0 to 13) is an artificially triggered response, produced by the injection of a steady depolarizing current via the intracellular recording electrode, to better show the effect of synaptic inhibition at seizure onset (see [28] for details).

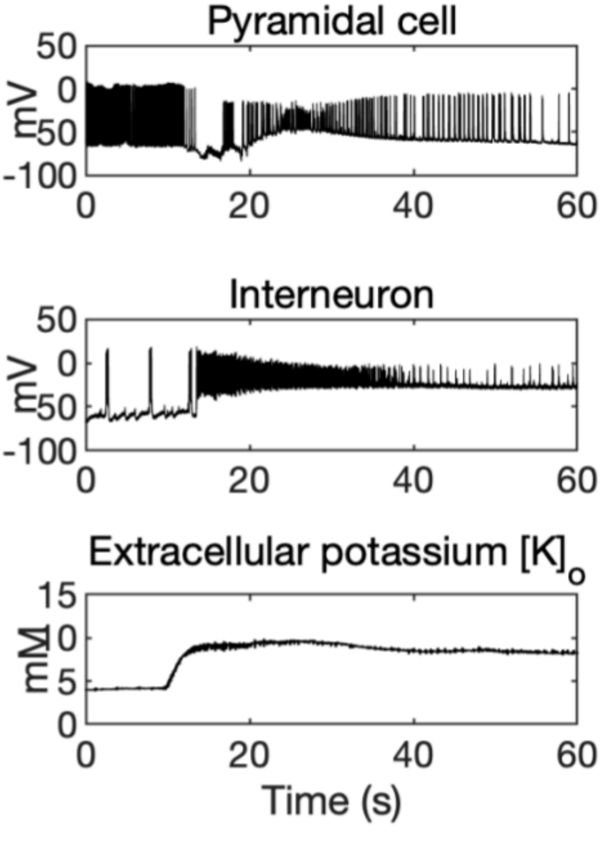

Figure 2.6: Experimental recordings obtained in the EC of the *in vitro* isolated guinea pig brain during three different trials (32 total repetitions). Top panel: selected principal cell intracellular voltage; middle panel: selected interneuron intracellular voltage; bottom panel: extracellular potassium concentration. Courtesy of Marco de Curtis, Istituto Neurologico Carlo Besta.

2.3 The double relation between $[\mathrm{K}^+]_o$ and neuronal activity

The extracellular potassium concentration plays a central role in seizure generation because it is directly related to neuronal excitability. This can be proven considering the *Goldman-Hodgkin-Katz voltage equation* for the resting membrane potential:

$$V_m = \frac{RT}{F} \ln \left(\frac{P_{\mathrm{K}}[\mathrm{K}^+]_o + P_{\mathrm{Na}}[\mathrm{Na}^+]_o + P_{\mathrm{Cl}}[\mathrm{Cl}^-]_i}{P_{\mathrm{K}}[\mathrm{K}^+]_i + P_{\mathrm{Na}}[\mathrm{Na}^+]_i + P_{\mathrm{Cl}}[\mathrm{Cl}^-]_o} \right) \tag{2.1}$$

where V_m is the neuron resting membrane potential in volts, R is the ideal gas constant (joules per degree per mole), T is the temperature in the Kelvin scale, and F is Faraday's constant (coulombs per mole). $[X]_i$ and $[X]_o$ denote respectively the intra- and extracellular concentrations in millimolar for ion species X. P_X is the permeability of the cell membrane to ion species X, measured in m/s. In the typical mammalian neuronal cell at rest the ion concentrations have the values reported in Table 2.1 (Johnston and Wu, 1995, [12]), and the resting membrane potential is ∼ -66 mV.

Ion species	Intracellular (mM)	Extracellular (mM)
K^+	140	5
Na^+	10	145
Cl^-	4	110
Ca^{2+}	1×10^{-4}	2.5

Table 2.1: Intra- and extracellular ion concentrations in a typical mammalian neuronal cell at rest.

From equation (2.1) it follows that, if the extracellular potassium concentration increases, the resting membrane potential is shifted towards the positive direction. This causes the neuron to become more excitable, since the higher the resting potential, the closer the cell is to its spiking threshold. The relation between the resting potential and the extracellular potassium concentration is shown in Fig. 2.7, where contribution of other ions is considered fixed and V_m is plotted as a function of just $[\mathrm{K}^+]_o$. This is feasible, since P_{K} is typically higher than P_{Na} and P_{Cl}, e.g., in the squid giant axon at rest the ratio of permeabilities is $P_{\mathrm{K}} : P_{\mathrm{Na}} : P_{\mathrm{Cl}} = 1 : 0.03 : 0.1$ [12]. It is evident that even a slight increase

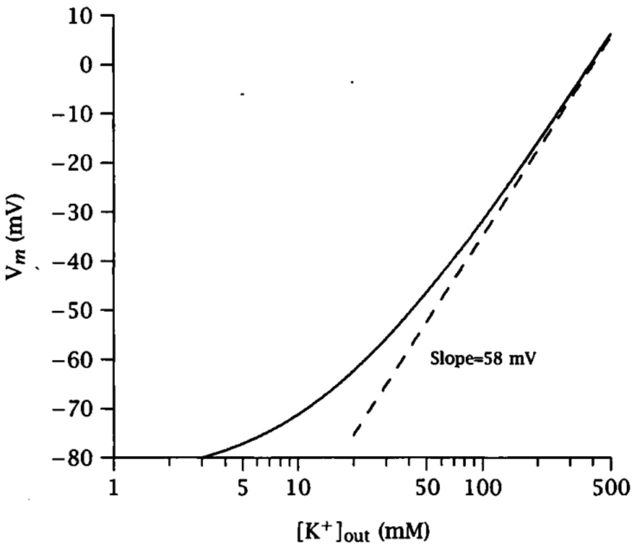

Figure 2.7: Extracellular K^+ concentration changes impact significantly cell excitability. The solid curve represents the resting membrane potential given by the Goldman-Hodgkin-Katz equation, and the dashed line the Nernst reversal potential for K^+. As $[\mathrm{K}^+]_o$ increases the two curves approach each other. Potassium concentration values are given in logarithmic scale. Source: Johnston et al., 1995 [12].

of extracellular potassium produces a remarkable shift of the resting potential towards positive values. As $[\mathrm{K}^+]_o$ keeps increasing,

$$V_m \approx \frac{RT}{F} \ln \left(\frac{P_\mathrm{K}[\mathrm{K}^+]_o}{P_\mathrm{K}[\mathrm{K}^+]_i} \right) = (58 \text{ mV}) \times \log \frac{[\mathrm{K}^+]_o}{[\mathrm{K}^+]_i}, \tag{2.2}$$

which is the *Nernst reversal potential* for K^+. This means that at elevated levels of $[\mathrm{K}^+]_o$, V_m and the potassium reversal potential have similar values, which is reflected by the approaching solid and dashed lines in Fig. 2.7.

It is therefore proven that $[\mathrm{K}^+]_o$ changes significantly cell excitability. It is nonetheless true that, conversely, neuronal activity affects the extracellular potassium concentration, which makes the relation between these two components reciprocal. It is indeed well known that during action potentials generation, after the sodium channels in the cell membrane open to allow Na^+ ions to flow in and depolarize the membrane, the potassium channels also open, making K^+ flow out into the extracellular space and thus repolarizing the cell (Fig 2.8). Neuronal activity is in fact the primary cause of the extracellular potassium concentration increase. Hence there exists a positive-feedback relationship between $[\mathrm{K}^+]_o$ and neuronal excitability.

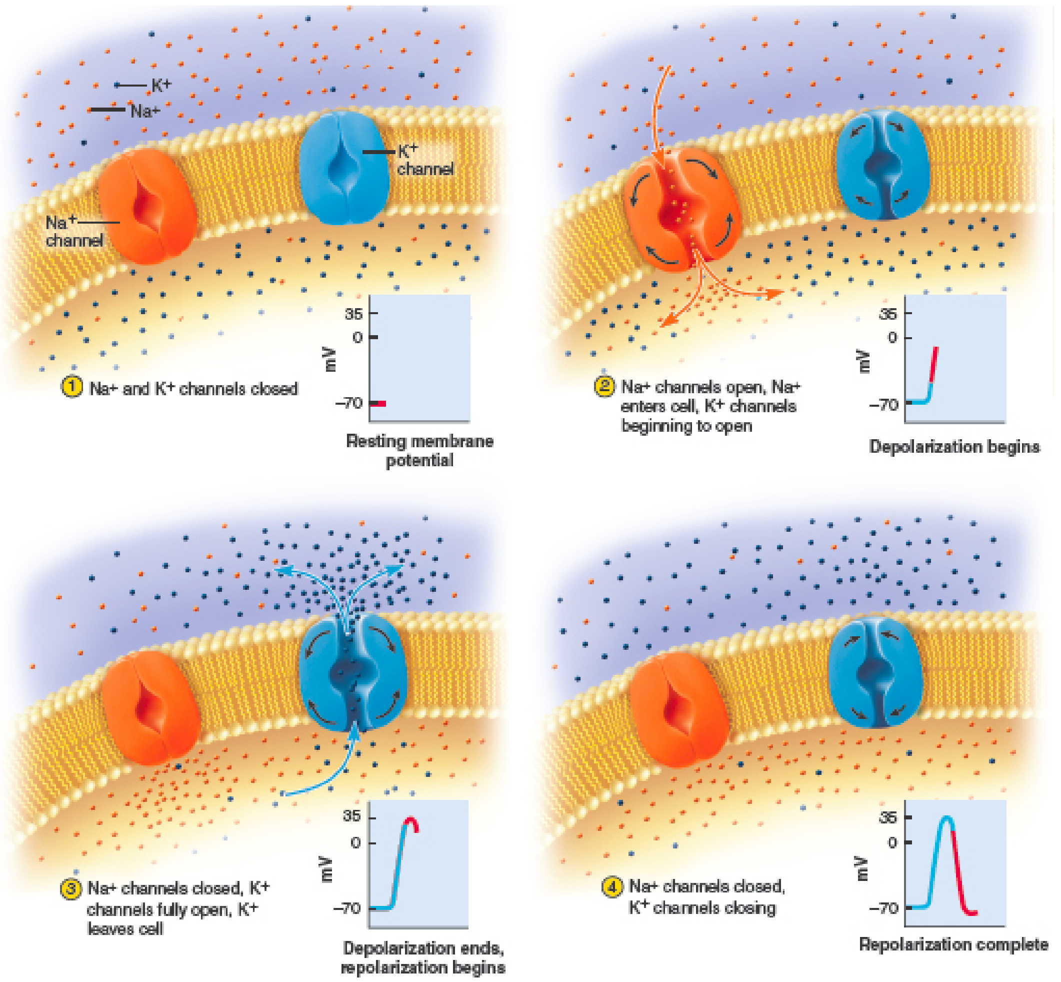

Figure 2.8: Neuronal activity is the first cause of increase of the extracellular potassium concentration. At rest both Na^+ and K^+ channels are closed (top-left panel). When action potentials are generated, the sodium channels open allowing sodium ions to flow inside the neuron and depolarize the membrane (top-right panel). When the action potential peak is reached, the sodium channels close and the potassium channels open (bottom-left panel), letting K^+ ions flow out and repolarizing the membrane (bottom-right panel). Source: A&P Review (n.d.). Pinterest. Retrieved November, 2020, from `https://pl.pinterest.com/pin/111745634493919606`

Chapter 3

The minimal model

The minimal computational representation consists of two multi-compartmental model cells, reproducing a pyramidal neuron and an inhibitory interneuron in the guinea pig brain entorhinal cortex surrounded by a common extracellular space (ECS), which is in turn enclosed by a bath representing the rest of the brain. The size of the ECS is estimated by the extracellular volume fraction α, defined by the ratio

$$\alpha = \frac{V_o}{V_i} = \frac{\text{Extracellular space volume}}{\text{Intracellular space volume}} \tag{3.1}$$

Changes of intra- and extracellular ion concentrations of K^+, Na^+, Ca^{2+} and Cl^- due to ion fluxes are incorporated. The fluxes are generated by a number of synaptic and non-synaptic mechanisms, such as: membrane currents, inhibitory synaptic currents, Na^+-K^+ pump, K^+ and Cl^- cotransporter KCC2 in the pyramidal cell, glial buffering of extracellular K^+, diffusion of K^+, Na^+ and Cl^- between the ECS space and the bath, diffusion between compartments of the same cell. All model equations are integrated in the NEURON environment with a fixed integration step of 0.05 ms. At each simulation step voltages, currents and ion concentrations are computed. The model structure is shown in Fig. 3.1.

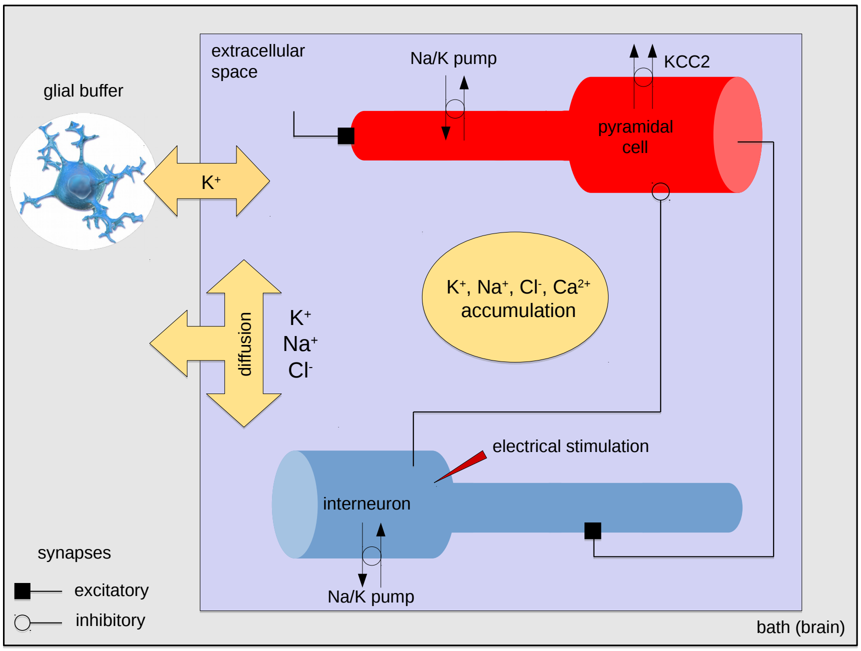

Figure 3.1: Minimal model structure. Two model cells, reproducing a pyramidal cell and an interneuron in the entorhinal cortex, are synaptically coupled and share a common extracellular space, which is surrounded by a bath accounting for the rest of the brain. The model includes a number of synaptic and non-synaptic mechanisms: synaptic currents, Na^+/K^+ pump in both cells, KCC2 cotransporter in the pyramidal cell, glial buffering of extracellular K^+ ions, and diffusion of K^+, Na^+ and Cl^- both between compartments and between the extracellular space and the bath. Interneuron firing at seizure onset is triggered via an externally input current applied to the soma.

3.1 Cells morphology

Model cells morphology is based on the work of Fransén et al., 2002 [39], where a pyramidal neuron and an interneuron are reduced to six equivalent cylinders: the pyramidal cell consists of one compartment representing the soma, three representing the apical dendrites and two the basal dendrites, and the interneuron is made up of a compartment representing the soma, three representing principal dendrites, and two the remaining dendrites. For the sake of simplicity, in the present model the dendrites of both cells were lumped together, and Rall's rule was applied to obtain the equivalent cylinders dimensions ([40] and pages 88–89 of [12]). The resulting pyramidal cell and interneuron models are therefore made up of just two compartments: one representing the soma and one the dendritic tree. In the model principal cell the somatic cylinder has length 20 μm and diameter 15 μm, the dendritic cylinder has length 450 μm and diameter 6.88 μm. In the model interneuron the soma has length 20 μm

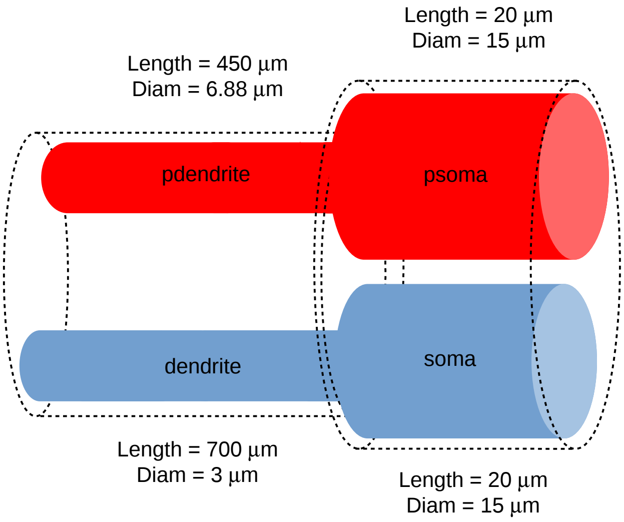

Figure 3.2: Multi-compartmental model cells used in the simulations: model pyramidal cell (top) and model interneuron (bottom). Common extracellular space indicated by the dashed lines. Picture not in scale. “psoma” and “pdendrite” stand respectively for pyramidal soma and pyramidal dendrite.

and diameter 15 μm, and the dendrite has length 700 μm and diameter 3 μm. The shared extracellular space also consists of two compartments, one around the somas and one around the dendrites. Each extracellular cylinder communicates with the corresponding intracellular compartment and the neighbouring extracellular segment. Model cells morphology is shown in Fig. 3.2.

3.2 Passive electrical properties

In all model compartments initial ion concentrations are as in Table 3.1.

Ion species	Intracellular (mM)	Extracellular (mM)
K^+	135	3.5
Na^+	10	140
Cl^-	3.5	135
Ca^{2+}	5×10^{-5}	2

Table 3.1: Initial intra- and extracellular concentrations for all ion species in all model cells.

The reversal potentials of Na^+ (E_{Na}), K^+ (E_K), Ca^{2+} (E_{Ca}), and Cl^- (E_{Cl})

are given by Nernst equation:

$$E_X = 2.3\frac{RT}{zF}\log\left(\frac{[X]_o}{[X]_i}\right) \tag{3.2}$$

where $[X]_i$ and $[X]_o$ represent respectively the intra- and extracellular concentrations in millimolar (mM) for ion species X, F is Faraday's constant, R is the gas constant, z is the valence of the species X (1 for K^+ and Na^+, 2 for Ca^{2+}, and -1 for Cl^-), and $T = 32$ ^{o}C as defined by the experimental setup. Leakage currents are modeled for Na^+, K^+ and Cl^- ions. They are implemented in all model compartments and have the following canonical expressions:

$$I_{Na,Leak} = g_{Na,Leak} \times (V_m - E_{Na}) \tag{3.3}$$

$$I_{K,Leak} = g_{K,Leak} \times (V_m - E_K) \tag{3.4}$$

$$I_{Cl,Leak} = g_{Cl,Leak} \times (V_m - E_{Cl}) \tag{3.5}$$

The initial resting membrane potential is set to -65 mV in both cells. In the pyramidal neuron the initial potassium and chloride concentrations are chosen so as to ensure KCC2 thermodynamic equilibrium, i.e., $[K^+]_o[Cl^-]_o = [K^+]_i[Cl^-]_i$ (Payne et al., [41]). In this way, the potassium and chloride cotransporter currents are initially zero, contributing to membrane potential stability at the beginning of the simulation. In both model neurons the specific axial resistance is set to $R_a = 100$ Ohm×cm and the specific membrane capacitance is $C_m = 1$ μF/cm^2, as in Fransén et al. [39]. It should be noted that under background excitatory synaptic input, ion concentrations and membrane potentials slightly deviate from initial equilibrium conditions.

3.3 Active currents

In the *in silico* pyramidal cell the following active membrane currents are modeled: transient Na^+ current and K^+ rectifier current responsible for action potentials (I_{NaT} and I_{Kdr}, respectively) in both compartments; persistent Na^+ current I_{NaP} in the soma; high-threshold Ca^{2+} current I_{CaL} in both compartments; calcium-dependent K$^+$ current I_{KAHP} in both compartments; fast calcium- and voltage-dependent K$^+$ current I_{KC} in both compartments; non-inactivating muscarinic K$^+$ current I_{KM} in the soma. The interneuron model has the I_{NaT} and I_{Kdr} currents responsible for action potentials in both compartments. All active currents are modeled according to Fransén et al. [39]. Changes to some parameter values have been applied in order to compensate for the non-synpatic mechanisms introduced in the present model.

3.4 Synaptic transmission and external stimulation

The pyramidal cell and the interneuron are synaptically coupled, as shown in Fig. 3.1. An inhibitory synapse is placed in the middle of the pyramidal cell soma and an excitatory synapse is placed in the middle of the interneuron dendrite. The synaptic conductances are modeled with a double-exponential function of the form:

$$g(t) = g_{max}\left(\frac{e^{-\frac{t}{\tau_2}} - e^{-\frac{t}{\tau_1}}}{\tau_2 - \tau_1}\right) \tag{3.6}$$

where τ_1 and τ_2 are the rise and decay time constants respectively, taking values 2 ms and 6 ms for all synapses, and g_{max} is the peak synaptic conductance, which equals 0.0015 μS for the inhibitory synapse and 0.0005 μS for the excitatory one. The excitatory postsynaptic currents (EPSC) reversal potential is set to 0 mV. In order to investigate the impact of chloride concentration changes on inhibitory synaptic transmission, the inhibitory GABA$_\mathrm{A}$ postsynaptic currents are made mediated by chloride ions. Since the GABA$_\mathrm{A}$ receptor pore conducts both Cl$^-$ and bicarbonate (HCO$_3^-$) in a 4:1 ratio [42], E_{GABAA} calculated using the Goldman-Hodgkin-Katz equation for these ion species equals:

$$E_{\mathrm{GABAA}} = \frac{RT}{F}\ln\left(\frac{4[\mathrm{Cl}^-]_i + [\mathrm{HCO}_3^-]_i}{4[\mathrm{Cl}^-]_o + [\mathrm{HCO}_3^-]_o}\right) \tag{3.7}$$

For simplicity, bicarbonate concentrations are assumed to be constant and equal to $[\mathrm{HCO}_3^-]_i = 15$ mM and $[\mathrm{HCO}_3^-]_o = 25$ mM, as in Doyon et al., 2011 [43]. With these settings, the unitary postsynaptic potentials (PSPs) have amplitudes at the soma of ∼2.3 mV (excitatory PSPs) and of ∼1 mV (inhibitory PSPs). A synaptic inhibitory response is generated in the postsynaptic cell when the presynaptic membrane potential in the soma crosses the threshold of -10 mV. In addition, the pyramidal cell receives a background input via an excitatory synapse placed in the dendrite and activated by a Poisson spike train with ∼66 Hz rate. To reproduce the enhanced interneuronal firing at seizure onset, the interneuron is stimulated through the injection of a depolarizing current into the soma at second 13. The current ramp has an initial amplitude of 1.3 nA, and then linearly decreases towards 0.5 nA at the end of the simulation (second 60).

3.5 Non-synaptic mechanisms

3.5.1 Ion accumulation in intra- and extracellular spaces

Due to transmembrane currents, ions accumulate in both intra- and extracellular spaces during seizures [21]. This means that ion concentrations are dynamic entities varying in time. In the model ion concentrations changes in a given compartment are governed by the following first-order differential equation

$$\frac{d[X]}{dt} = \frac{\sum I_X}{z \times F \times V} \tag{3.8}$$

where $[X]$ is the concentration of ion species X (intracellular or extracellular), $\sum I_X$ is the net ion transmembrane flux, F is Faraday's constant, V the compartment volume, and z the valence of species X. It is easy to notice that for positive z, if $\sum I_X > 0$ the right-hand side of the equation is positive, and therefore the concentration $[X]$ increases; conversely, if $\sum I_X < 0$ the right term is negative and $[X]$ decreases. Ion accumulation is modeled for K^+, Na^+, Ca^{2+}, and Cl^-.

3.5.2 Active transport of ions

The membrane of most brain cells is equipped with proteins capable of pumping ions from one side of the membrane to the other [12]. Of those macromolecule species, at least two regulate the extracellular potassium concentration, and hence play an important role in seizure dynamics: the Na^+-K^+ pump and the potassium-chloride KCC2 cotransporter.

The Na^+-K^+ pump is probably the most important ion transporter in biological membranes, pumping three Na^+ ions out of the cell for every two K^+ ions pumped in. It is present in virtually all brain cells, and is the primary cause of the maintenance of the Na^+ and K^+ concentration gradients across the membrane. In the model the Na^+-K^+ pump is recreated by two Na^+ and K^+ currents simulating the pump regulatory action, which have the mathematical expressions (Kager et al., 2000 [44]):

$$\begin{aligned} I_{Na} &= 3 \times I_{max} \times flux([\mathrm{Na}^+]_i, [\mathrm{K}^+]_o) \qquad (3.9) \\ I_K &= -2 \times I_{max} \times flux([\mathrm{Na}^+]_i, [\mathrm{K}^+]_o) \qquad (3.10) \end{aligned}$$

where

$$flux([\mathrm{Na}^+]_i, [\mathrm{K}^+]_o) = \left(1 + \frac{Km_K}{[\mathrm{K}^+]_o}\right)^{-2} \times \left(1 + \frac{Km_{Na}}{[\mathrm{Na}^+]_i}\right)^{-3} \qquad (3.11)$$

and the parameter $I_{max} = 0.0013$ mA/cm^2. K_m is Michaelis' constant, defined as the ion concentration at which an enzyme reaches half of its maximal activity (Roberts et al., [45]). The Michaelis' constant values for Na^+ and K^+ are as in Kager et al., 2007 [46]: $Km_K = 2$ mM and $Km_{Na} = 10$ mM.

In adult hippocampal pyramidal cells the intracellular Cl^- concentration is maintained low by means of the potassium-chloride cotransporter KCC2, mediating the transport of K^+ and Cl^- across the membrane (Payne et al. [41]). The migration process is driven by the K^+ gradient, which leads to the extrusion of one Cl^- ion together with a K^+ ion. In the model this mechanism is implemented in both pyramidal cell compartments by means of two K^+ and Cl^- currents, having the expressions (Wei et al., 2014 [27]):

$$I_K = \gamma_j U_{KCC2} \ln\left(\frac{[\mathrm{K}^+]_i[\mathrm{Cl}^-]_i}{[\mathrm{K}^+]_o[\mathrm{Cl}^-]_o}\right) \tag{3.12}$$

$$I_{Cl} = -\gamma_j U_{KCC2} \ln\left(\frac{[\mathrm{K}^+]_i[\mathrm{Cl}^-]_i}{[\mathrm{K}^+]_o[\mathrm{Cl}^-]_o}\right) \tag{3.13}$$

where $U_{KCC2} = 0.3$ mM/s is the cotransporter strength, estimated using the peak conductances given in Lauf et al., 2000 [47], $\gamma_j = S_j/(FV_j)$ is a conversion factor from concentration units (mM/s) to current units (mA/cm^2), F is Faraday's constant, and S_j and V_j are the total surface area and the total intracellular volume of compartment j, respectively.

3.5.3 Ion diffusion: longitudinal and to the bath

The ions accumulated in intra- and extracellular spaces can diffuse to both neighbouring compartments within the same cell and to distal brain regions. The first kind of diffusion is referred to as *longitudinal diffusion* [48], and the related contributions to model concentrations are calculated using Fick's first law:

$$\frac{d[X_i]}{dt} = D_X \times \sum_{j=1}^{N} \frac{([X_j] - [X_i]) \times S_{ij}}{L_{ij} \times V_i} \tag{3.14}$$

where $[X_i]$ is the intra- or extracellular concentration of species X in compartment i, D_X is the longitudinal diffusion constant for X, S_{ij} is the flux area between the adjacent compartments i and j, L_{ij} is the distance between the centers of compartments i and j, and V_i is the volume of compartment i. Longitudinal diffusion is implemented for K^+, Na^+, Ca^{2+}, and Cl^-; the diffusion constant for each species is given in [49]. If the net flow to compartment i is positive, the right-hand side of equation (3.14) is positive and $[X_i]$ increases; if the net flow is negative, $[X_i]$ decreases. The sum is made over the total number N of compartments adjacent to i.

In addition, due to various processes including transport into capillaries and potassium regulation by glial cells, ions can diffuse to more distant regions. Such a phenomenon is referred to as *diffusion to the bath* and is modeled as a diffusive exchange of ions between the extracellular space and a fictitious bath. As a consequence of brain vasculature complexity, the time constant of the joint processes governing this kind of diffusion is likely to be much slower than in the longitudinal diffusion case, where ions are exchanged virtually instantaneously. To take this into account, the diffusion constant is rescaled with a factor $s = 5 \times 10^3$. Ion concentrations in the bath are assumed to be constant and equal to the initial extracellular concentrations. Diffusion to the bath is modeled for K^+, Na^+ and Cl^- using, again, Fick's first law:

$$\frac{d[X_i]_o}{dt} = \frac{1}{s} \times \frac{D_X \times ([X]_{bath} - [X_i]_o) \times S_i}{(dr_i/2) \times V_i} \tag{3.15}$$

where $[X_i]_o$ is the extracellular concentration of species X in compartment i, $[X]_{bath}$ is the concentration of X in the bath, $S_i = 2\pi L_i(r_i + dr_i)$ is the flux area for compartment i, $V_i = \alpha\pi r_i^2 L_i$ is the extracellular volume of compartment i, and $dr_i = r_i(\sqrt{\alpha + 1} - 1)$ is the thickness of the extracellular space; S_i, V_i and dr_i are functions of the radius r_i and length L_i of compartment i.

It should be pointed out that realistic diffusion of ions in the brain is governed by electrodiffusion (Nernst, 1888 [50]), and therefore ion diffusion should be modeled according to the Nernst-Planck equation, which extends Fick's law to the case where the diffusing particles are moved with respect to the fluid by electrostatic forces [51]. Nevertheless, the work of Halnes et al., 2013 [52], shows that transport of ions under conditions of intense neuronal activity is in fact dominated by diffusion rather than by electrical fields, hence justifying the use of Fick's first law.

3.5.4 Glial buffering of $[\mathbf{K}^+]_o$

Glial cells, once believed to play a passive role in the CNS, are in reality active regulators of numerous functions in the brain, including clearance of synaptic neurotransmitters and extracellular ion concentration maintenance [53]. Due to their unusually high permeability to potassium ions, glial cells are well suited for K^+ buffering [54], [55]. They have the ability to intake and traverse potassium from regions of high concentration to regions of low concentration, keeping $[K^+]$

low in the extracellular environment.

Potassium buffering is modeled by a reaction scheme simulating the glial potassium uptake system (Kager et al. [44]):

$$\begin{aligned}
\frac{d[\mathrm{K}^+]_o}{dt} &= -k_2 \times [\mathrm{K}^+]_o \times [B] + k_1 \times [KB] && (3.16)\\
\frac{d[B]}{dt} &= -k_2 \times [\mathrm{K}^+]_o \times [B] + k_1 \times [KB] && (3.17)\\
\frac{d[KB]}{dt} &= k_2 \times [\mathrm{K}^+]_o \times [B] - k_1 \times [KB] && (3.18)
\end{aligned}$$

where $[B]$ is the free buffer, $[KB]$ the bound buffer, and k_1 and k_2 the backward and forward rate constants, respectively. Initial conditions and rate constants as defined in Gentiletti et al. [49].

3.6 Simulation results

In Fig. 3.3 simulation results obtained with the minimal model and experimental data are compared. The time course of the depolarizing current applied to the model interneuron to trigger seizure-like events is shown in the middle panel of Fig. 3.3B (red line). The current produces a strong discharge in the interneuron at seizure onset ($t = 13$ s) with an initial firing rate of ~300 Hz. Simultaneously, normal background activity in the model pyramidal cell ceases because of the strong inhibitory action. The principal neuron remaines inactive for about 7 seconds, after which irregular spiking begins and reaches the maximum frequency of ~8 Hz in about 11 seconds since the beginning of the episode. During the seizure the spike amplitude in the interneuron gradually decreases. This set of changes couples with an initial sharp increase of the extracellular potassium concentration, which reaches the maximum value of ~9 mM within the first seconds of the episode and moderately decreases later on.

It can be observed that model results are in qualitative and quantitative agreement with the experimental seizure induced in the isolated guinea pig brain (Fig. 2.6 and 3.3A). The *in vitro* interneuron discharges at an initial rate of ~400 Hz, which progressively decreases, while the maximum firing frequency

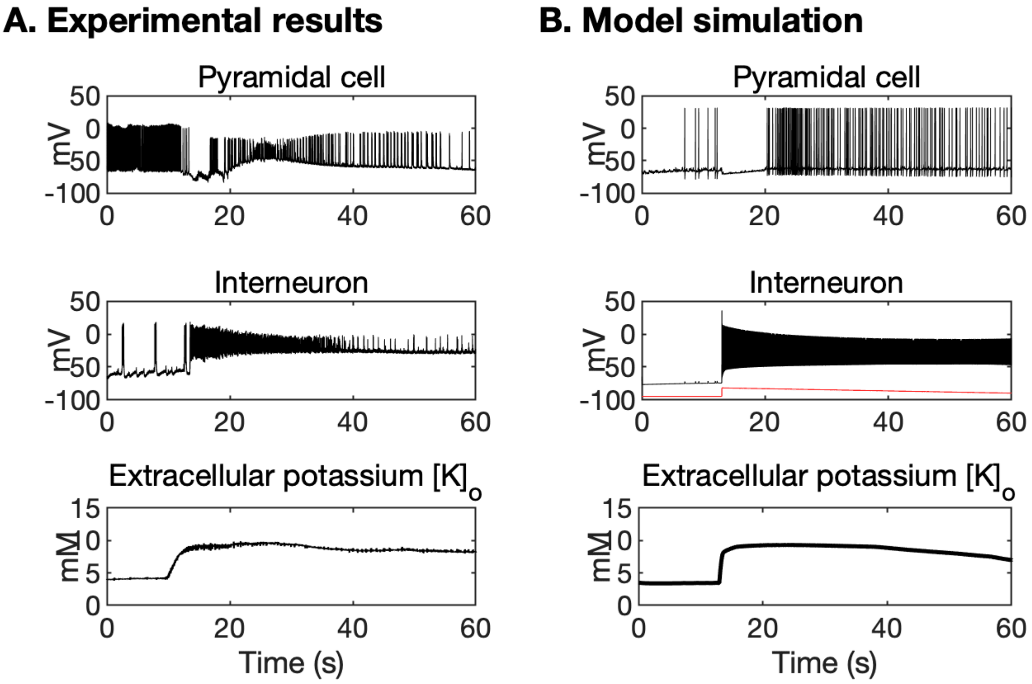

Figure 3.3: Comparison of experimental data (A) and model simulation results (B). Top panels: pyramidal cell voltage traces. Middle panel: interneuron voltage traces. Bottom panels: extracellular potassium concentration traces. The time course of the depolarizing current triggering the seizure in the model is shown in the right middle panel (red line). At seizure onset the interneuron fires strong discharges, while the pyramidal cell becomes silent for a few seconds, after which tonic activity is resumed. The extracellular potassium concentration rises up within the first seconds of the epileptic episode and remains elevated until the end of the simulation.

reached by the pyramidal cell during the irregular spiking phase is ∼9 Hz. The extracellular potassium concentration in the preparation attains its maximum value of ∼9.5 mM a few seconds after seizure onset and subsequently decays towards slightly lower values.

3.6.1 Seizure patterns and ion concentration changes

The cell firing patterns *in silico* are determined by both membrane and synaptic currents, as well as non-synaptic mechanisms. Fig. 3.4 illustrates the time course of intra- and extracellular ion concentrations and reversal potentials for K^+, Na^+ and Cl^- in the model cells, and shows the evident relation between seizure-like activity and ion concentration changes. At seizure onset a sharp rise of the extracellular potassium concentration and potassium reversal potential is observed (Fig. 3.4, first column). The strong interneuron action inhibites the pyramidal cell by means of $GABA_A$ receptor-mediated currents, which elevate

(a) Pyramidal cell

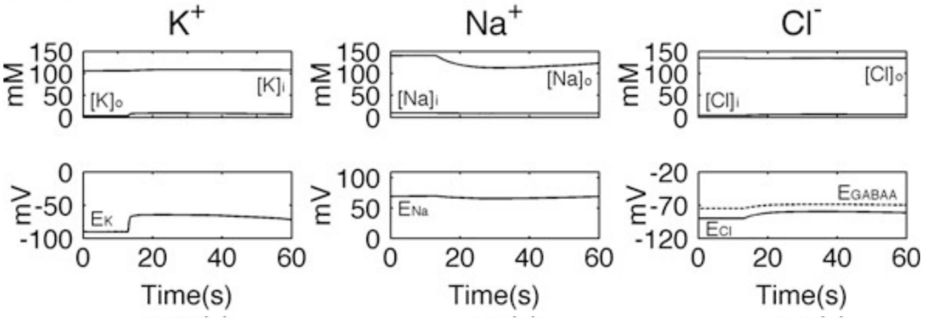

(b) Interneuron

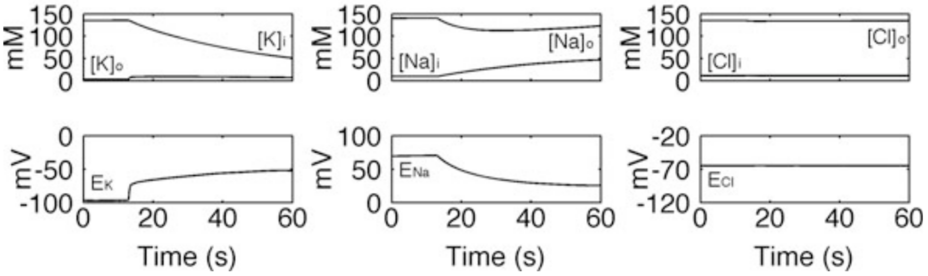

Figure 3.4: Ion dynamics in the model pyramidal cell (a) and interneuron (b) during simulated seizures in the model. For each cell type, intra- and extracellular concentrations are shown in the top panels and the corresponding reversal potentials in the bottom panels.

intracellular chloride and GABA$_\mathrm{A}$ reversal potential in the principal neuron (Fig. 3.4, third column, top panel). As the seizure progresses, the sodium reversal potential in the interneuron declines, causing the amplitude of spikes to decrease (Fig. 3.4, second column, bottom panel). Later on the non-synaptic mechanisms responsible for extracellular potassium clearance start operating, leading to a decrease in potassium reversal potential and neuronal activity in the pyramidal cell (Fig. 3.4, first column, top panel).

3.6.2 Sources and balance of $[\mathrm{K}^+]_o$

In the model the $[\mathrm{K}^+]_o$ trace can be split into the sum of its individual components. From equation (3.8) it follows that the contribution of a specific K$^+$ membrane current $I_{K,j}$ to the extracellular potassium concentration in a certain compartment from time t_1 to t_2 equals:

$$[\mathrm{K}^+]_{o,j} = \int_{t_1}^{t_2} \frac{I_{K,j}(t)}{z \times F \times V} dt \tag{3.19}$$

where $[K^+]_{o,j}$ is the potassium contributed by $I_{K,j}$, V is the extracellular compartment volume, and $z = 1$ for K^+. In order to identify the main sources of extracellular potassium accumulation in both pyramidal cell and interneuron, contributions were calculated using equation (3.19). In the interneuron, the dominant contribution to $[K^+]_o$ comes from action potential firing (current I_{Kdr} in Fig. 3.5, top panel, red diamonds), while the potassium leak current flux is negligible (top panel, blue circles). The Na^+-K^+ pump potassium current removes extracellular K^+ ions, its contribution is therefore negative (top panel, green stars). The resulting potassium flow, calculated as the sum of the three aforementioned components, is shown in Fig. 3.5, bottom panel.

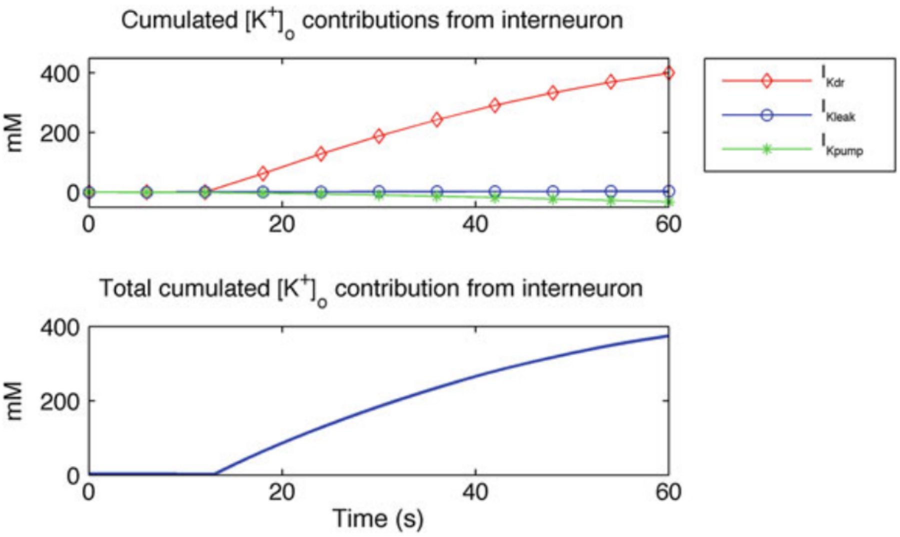

Figure 3.5: Top panel: single contributions to $[K^+]_o$ in the interneuron soma. Red: action potential firing; blue: potassium leak current flux; green: Na^+-K^+ pump potassium current flux. Bottom panel: total amount of extracellular potassium contributed by the interneuron soma.

In the pyramidal cell soma, leak and voltage-gated potassium currents fluxes are negligible, and the dominant role is played by the KCC2 cotransporter K^+ current (Fig. 3.6, top panel, black triangles). Since $[K^+]_o$ reaches high levels during seizure-like activity, the potassium KCC2 current becomes negative and acts in fact as a clearance mechanism by transporting both K^+ and Cl^- ions into the cell. As in the interneuron, the Na^+-K^+ pump reduces $[K^+]_o$ (top

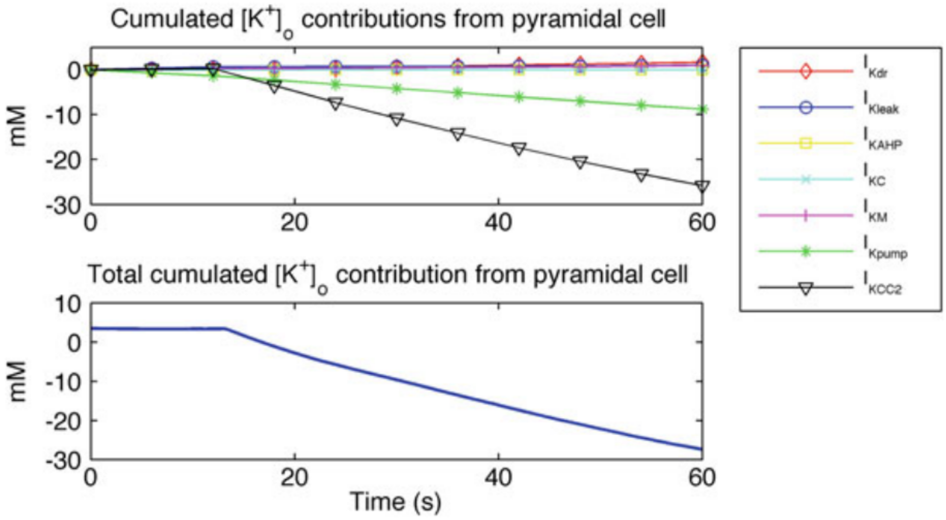

Figure 3.6: Top panel: contributions to $[K^+]_o$ in the principal neuron soma. Red: action potential firing; blue: potassium leak current flux; yellow: I_{KAHP} current flux; cyan: I_{KC} current flux; magenta: I_{KM} current flux; green: Na^+-K^+ pump potassium current flux; black: potassium KCC2 current flux. Bottom panel: total amount of extracellular potassium contributed by the pyramidal soma.

panel, green stars). The total K^+ flow is shown in Fig. 3.6, bottom panel.

In addition to membrane currents, Na^+-K^+ pump and KCC2, extracellular potassium accumulation is also influenced by glial buffering, longitudinal diffusion and diffusion to the bath. The individual components shaping the $[K^+]_o$ trace in the common extracellular somatic compartment are shown in Fig. 3.7, top panel. The net extracellular potassium, obtained by adding up all fluxes, is depicted in Fig. 3.7, bottom panel, and corresponds to the time course observed during the model seizure (Fig. 3.3B). It is evident that the most relevant contribution to $[K^+]_o$ comes from interneuronal firing (top panel, red diamonds); as for the potassium clearance mechanisms, the dominant role is played by diffusive processes (pink circles and black crosses). The analysis of individual $[K^+]_o$ components demonstrates that extracellular potassium accumulation is the outcome of a fine balance between a number of distinct mechanisms operating simultaneously.

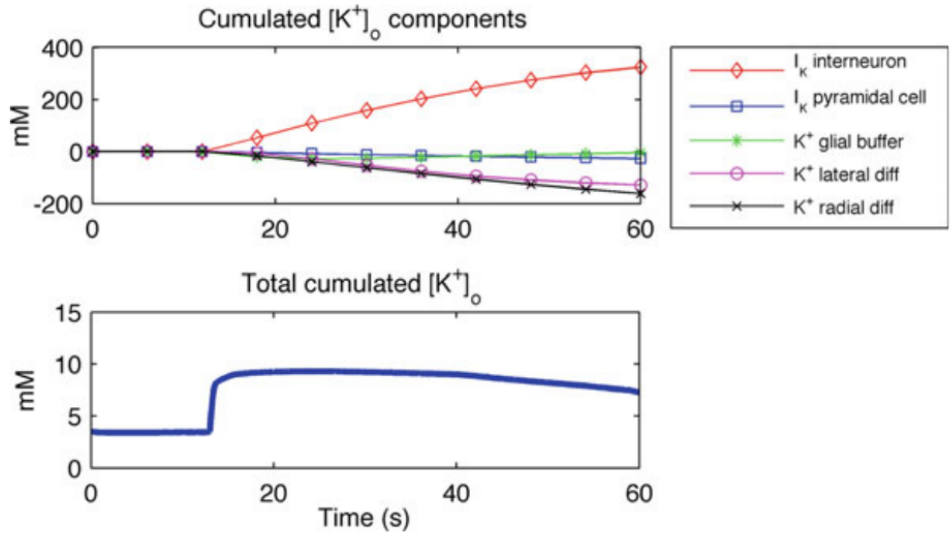

Figure 3.7: Top panel: potassium fluxes contributed by the pyramidal cell soma, interneuron soma, glial buffer and diffusion (longitudinal and to the bath, here referred to as "lateral" and "radial", respectively). Potassium clearance is dominated by diffusion (magenta circles and black crosses). Bottom panel: net cumulated extracellular K^+ concentration.

3.6.3 Alteration of K^+ clearance mechanisms

Through the model, it is possible to investigate how the impairment of a certain extracellular potassium clearance mechanism affects cells behavior. This can be achieved by removing the mechanism from the full setup and then performing simulations with the resulting altered model. On account of such manipulations, insight into the relevance of the excluded processes can be gained.

Simulation results obtained running the model excluding glial buffering are shown in Fig. 3.8. In the absence of glial cells, $[K^+]_o$ increases sharply at seizure onset and reaches a value of ~25 mM (bottom trace). This causes a *depolarization block* in the pyramidal cell until the end of the simulation (top trace). A depolarization block is a condition in which neuronal firing is prevented by a long-lasting depolarization induced by elevated extracellular K^+. After the principal cell enters the block, the interneuron keeps firing (middle trace), however the spike amplitude is significantly reduced. Later on, the

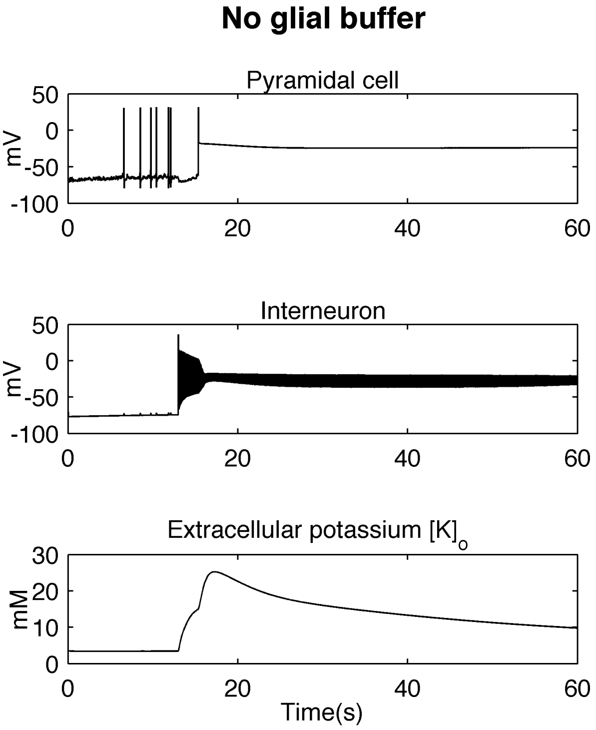

Figure 3.8: Voltage and extracellular potassium traces obtained with the altered model excluding glial buffering.

combined action of the Na^+-K^+ pump and K^+ diffusion causes $[K^+]_o$ to decrease towards ~10 mM at second 60 (bottom trace).

When diffusion to the bath of potassium is neglected, the outcome shown in Fig. 3.9 is produced. Here again the pyramidal cell enters a permanent depolarization block at seizure onset (top trace), but the corresponding value reached by the excessive $[K^+]_o$ is ~10 mM (bottom trace), less than in the previous scenario. The interneuron discharges with gradually decreasing spike amplitude until second 40, after which it becomes depolarized until firing is prevented (middle trace). $[K^+]_o$ increases throughout the whole simulation, proving that glial buffer and Na^+-K^+ pump alone are not sufficient to clear potassium effectively.

Lastly, Fig. 3.10 illustrates the model behavior in the absence of the Na^+-K^+ pump. When the pump is missing, even a moderate extracellular potassium concentration increase (~0.5 mM) with respect to the baseline provokes abnormal firing in the pyramidal cell at the beginning of the simulation (top trace). A few seconds after seizure onset $[K^+]_o$ reaches a value above 10 mM, and

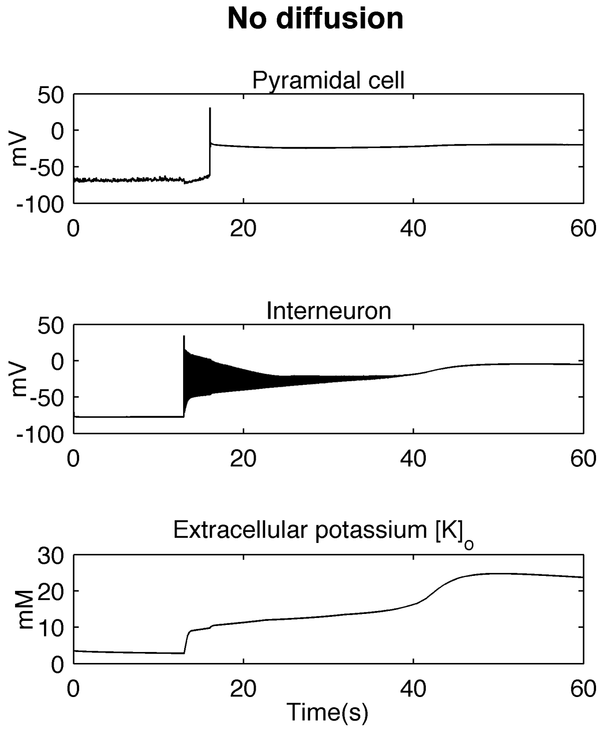

Figure 3.9: Voltage and extracellular potassium traces obtained with the altered model excluding diffusion to the bath. $[K^+]_o$ generalized increase (bottom trace) shows that the glial buffer and Na^+-K^+ pump alone are not able to fully regulate potassium homeostasis.

pyramidal cell activity is blocked. The interneuron fires until second ~43 and then becomes stuck in the depolarized state (middle trace). The $[K^+]_o$ time course is similar to the one reproduced by the full model, but the maximum concentration reached by potassium is slightly higher, as reported in Table 3.2.

The results discussed in this section show that removing any of the potassium clearance mechanisms has a significant impact on model dynamics. Omittance of potassium diffusion to the bath or glial buffering leads to elevated extracellular potassium, which results in highly depolarized membrane potentials. Elimination of the Na^+-K^+ pump eventually blocks neuronal activity in both cells, but the extracellular potassium concentration trace does not deviate considerably compared to the intact model. This suggests that in the *in silico* representation diffusion processes and glial buffering are more effective in clearing extracellular potassium than the Na^+-K^+ pump.

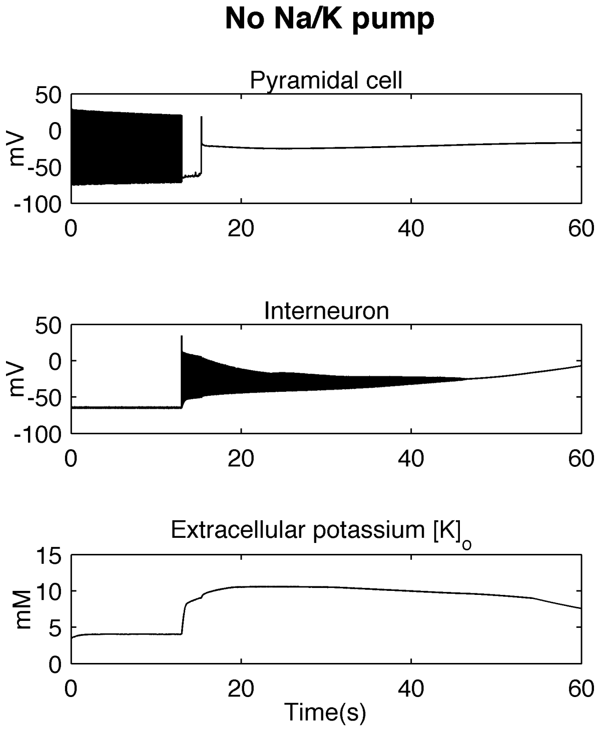

Figure 3.10: Voltage and extracellular potassium traces obtained with the altered model excluding the Na^+-K^+ pump.

Model	$[K^+]_o$ max value (mM)	$[K^+]_o$ final value (mM)
Full model	~9.3	~7.3
No glial buffer	~25.8	~10.5
No diffusion	~23.5	~23.5
No Na^+-K^+ pump	~10.7	~6.9
No ion dynamics	3.5	3.5

Table 3.2: Maximum and final ($t = 60$ s) $[K^+]_o$ values in the full and altered models.

3.6.4 The model with fixed ion concentrations

In order to assess the actual relevance of ion dynamics in model seizures initiation and progression, all ion fluxes were nullified by setting to zero the right-hand sides of differential equations (3.8), (3.15) and (3.16) – (3.18). Under such conditions the interneuron and pyramidal cell interact only by means of synaptic connections, and communication via the common extracellular space is precluded. In particular, $[K^+]_o$ remains constant and equal to the baseline value. Results are shown in Fig. 3.11: the sustained interneuron activity (middle trace) has a strong inhibitory effect on the pyramidal cell, which is reduced to neuronal silence (top trace). The model with constant ion concentrations cannot, therefore, recreate the experimental traces (Fig. 2.6 and 3.3A). This

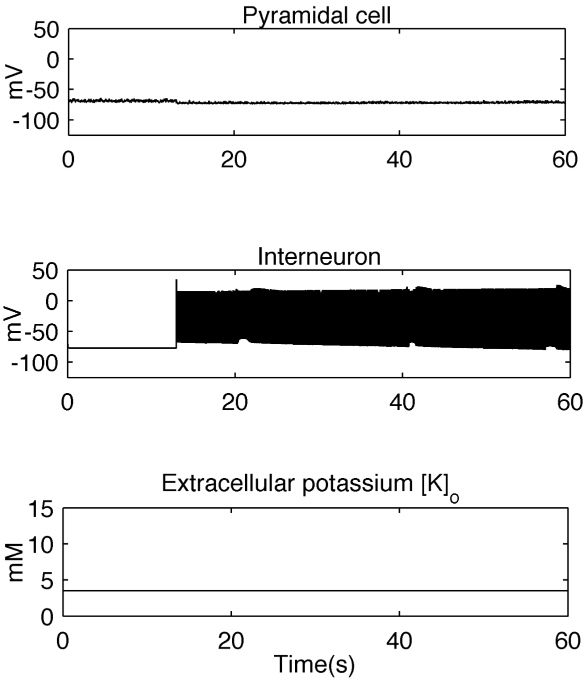

Figure 3.11: Simulation results obtained with the constant ion concentrations model.

proves that ion dynamics is an essential component to reproduce the experimental seizure patterns in the model.

Chapter 4

The extended model

4.1 Why is the extension needed?

Even though the minimal model can reproduce many of the features observed experimentally in the *in vitro* guinea pig brain during seizures, it is too simplified to render the real system's wide range of complexity. In the first place, the considered neuronal network consists of the least possible number of cells – just two. Surprisingly, even with such a reduced setup it is possible to obtain simulation results strongly resemblant real neurons pathological patterns. This can be possibly explained with the fact that during epileptic episodes large populations of neurons synchronize, and therefore the overall behavior can be recreated by just a few representative elements [29]. On the other hand, the mechanisms responsible for the transition from normal state to epileptic regime in the brain might be in fact related to network phenomena, which cannot be investigated using the minimal model.

The model described in Chapter 3 does not incorporate many properties of real neurons processes and cell microenvironment characteristics. It does not consider, for example, the electroneutrality of CNS milieu. The electroneutrality principle requires that positive and negative ion charges do not deviate appreciably in a macroscopic volume of tissue [56], or equivalently the net charge is "very small" compared to either the cations total charge or the anions total charge. The accuracy of the principle depends on the total charge present in a certain CNS portion and the portion size: it is exact only when there are no electric potential differences across the space, but it is true to a good approximation whenever the space volume is sufficiently large. In practice, the electroneutrality assumption holds for regions as large as a mammalian cell [57]. Since electroneutrality can significantly influence neuronal stability at rest, it is an important feature to include in computational representations of CNS regions.

Another important aspect is represented by cell volume changes during ictal activity. It has been found that both neurons and glial cells swell under conditions of abnormal neuronal firing ([58], [59], [60]). The marked ion concentration changes during seizures lead to the shrinkage of the extracellular space, which in turn causes extracellular concentrations ($[K^+]_o$ in particular) to elevate, contributing to seizure evolution. Because of their potential relevance, cell volume changes should be implemented in computational models of epilepsy.

The minimal model fails to reproduce the bursting phase recorded in the *in toto* preparation, which arises in the interneuron and pyramidal cell in the late part of experimental seizures [31]. The sequence of events “low voltage fast activity – irregular spiking – rhythmic bursting” is observed in experimental LPF signals, as well as in human focal seizures. It has also been shown in hippocampal slices that elevated potassium may transform the firing pattern from tonic to bursting [61]. Rhythmic bursting appears therefore to be a substantial component of ictal patterns, which accurate computational reproductions of epilepsy should not leave out of consideration.

Ictal episodes, once initiated, evolve and terminate presumably due to activity-dependent ion concentration shifts and homeostatic mechanisms eventually restoring physiological levels. In the model described in Chapter 3 seizure termination is not reproduced: if the simulation time is extended from 60 s to 300 s, the results shown in Fig. 4.1 are obtained. $[K^+]_o$ stabilizes at a value ~6.8 mM at ~100 s (bottom panel), causing the interneuron to enter a depolarization block (middle panel). The pyramidal cell (top panel) starts sustained activity at seizure onset, and then fires fast spikes indefinitely. In order to obtain a realistic representation of the epileptic behavior, a faithful *in silico* model

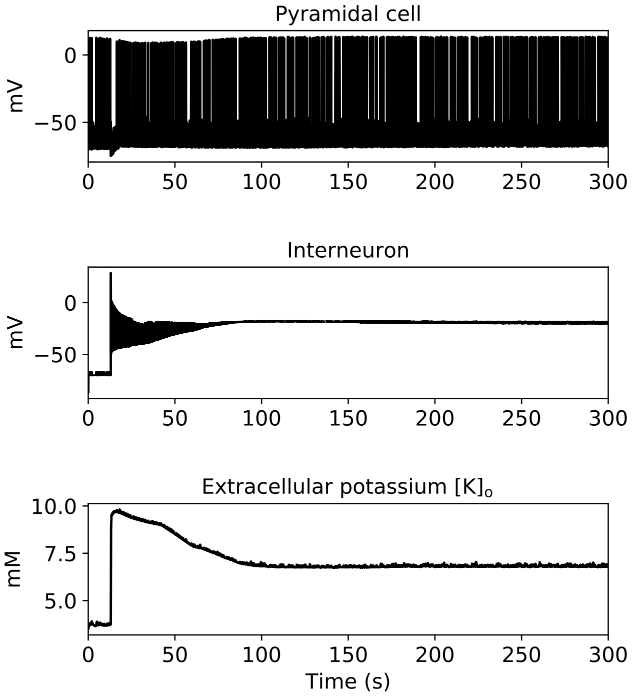

Figure 4.1: Seizure termination cannot be recreated in the minimal model. When the simulation end time is protracted to second 300, the interneuron enters a permanent depolarization block, $[K^+]_o$ becomes steadily elevated above the baseline level, and the principal cell uninterruptedly fires strong discharges after seizure onset.

should secure the seizure termination phase.

4.2 Extended model structure and cells morphology

In hippocampal circuits interneurons are present in lower number with respect to principal cells. In particular, it was estimated that in the rat CA1 region the ratio of pyramidal cells to interneurons is approximately 92:8 $\approx$ 10:1 (Bezaire et al., 2013, [30]). This means that a good *in silico* representation of the biological picture should ideally include at least 10 pyramidal cells and one interneuron. However, to avoid incurring a heavy computational burden, a ratio of 4:1 pyramidal cells to interneurons is considered in the extended model, which therefore consists of a total number of five neurons. Individual cells morphology and the model structure are depicted in Fig. 4.2. Each pyramidal neuron is an exact replica of the model excitatory cell described in Chapter 3, consisting of two compartments: one representing the soma with length 20 μm and diameter 15 μm, and one modeling the dendritic tree with length 450 μm and diameter 6.88 μm. The interneuron is simplified with respect to the previous model by neglecting the dendrite, judged not to add significant contribution to cells behavior. The new inhibitory cell is thus made up of a single compartment representing the soma, with length 20 μm and diameter 15 μm. As in the original setup, the cells are enclosed by a bath modeling remote brain areas. To each cylinder corresponds an extracellular compartment in which ion dynamics of K^+, Na^+, Ca^{2+}, Cl^- and non-synaptic mechanisms are implemented. Diffusive exchange of sodium and potassium ions is allowed to take place between extracellular compartments, as illustrated in Fig. 4.2 and 4.3. Extracellular compartments are imagined to be adjacent. Within single cells, longitudinal diffusion of ions between contiguous compartments, both intra- and extracellular, is implemented. Additionally bicarbonate ions HCO_3^-, contributing to $\mathrm{GABA_A}$ currents, and impermeant anions A^- are included. Intra- and extracellular bicarbonate concentrations are fixed, while anions concentrations dynamics is limited to volume changes. Epileptic activity is again triggered by means of a depolarizing current ramp applied to the interneuron, sufficiently large to produce intense firing at seizure onset. The current has initial amplitude of 0.8 nA and linearly decreases towards 0.02 nA during 30 seconds.

4.3 Anions and electroneutrality

The law of electroneutrality states that in any single ion solution a sum of negative electrical charges attracts an equal sum of positive electrical charges. When applied to single cell compartments the principle of electroneutrality can be read as:

$$\sum_X z_X [X]_{i,j} = 0 \tag{4.1}$$

$$\sum_X z_X [X]_{o,j} = 0 \tag{4.2}$$

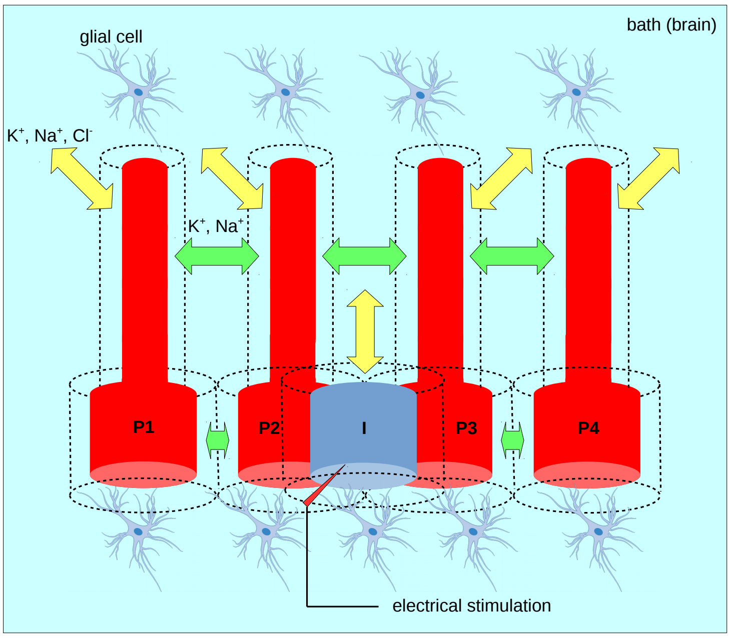

Figure 4.2: Extended model structure. Four entorhinal cortex pyramidal cells (red) and an interneuron (blue) are surrounded by a bath representing remote brain regions. Each compartment is surrounded by its own extracellular space (dashed lines) in which ion dynamics is implemented. Longitudinal diffusion is modeled in multi-compartmental cells only, and diffusion to the bath (yellow arrows) is implemented in all cylinders for K^+, Na^+ and Cl^-. In addition K^+ and Na^+ ions can be exchanged between neighboring extracellular spaces (green arrows). Seizures in the model are triggered by a depolarizing current input to the interneuron. Picture not in scale. Pi and I stand respectively for the i-th pyramidal cell ($i = 1,...,4$) and interneuron.

where $[X]_{i,j}$ and $[X]_{o,j}$ denote the intra- (i) and extracellular (o) concentrations of ion species X in compartment j, z_X is the valence of X, and sums are made over all species. In the previous model version the electroneutrality condition is not fulfilled at time $t = 0$; in order to guarantee it in the new design, anions A^- were introduced following the work of Somjen et al. in [62] and [46]. Anions are assumed to be impermeant, i.e. no flow across the cell membrane takes place; for simplicity, their diffusion is also neglected. In the new model therefore the full form of equations (4.1) and (4.2) is:

$$[K^+]_i + [Na^+]_i - [Cl^-]_i + 2[Ca^{2+}]_i - [HCO_3^-]_i - [A^-]_i = 0 \tag{4.3}$$

$$[K^+]_o + [Na^+]_o - [Cl^-]_o + 2[Ca^{2+}]_o - [HCO_3^-]_o - [A^-]_o = 0 \tag{4.4}$$

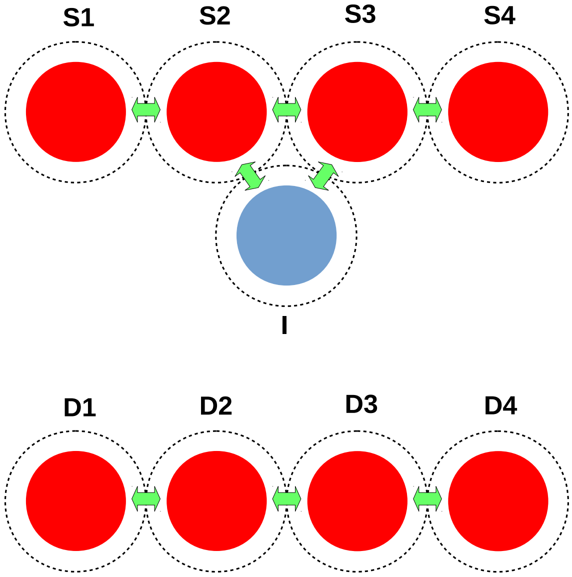

Figure 4.3: Ion exchange between neighboring extracellular spaces (green arrows). Si and Di indicate respectively the i-th pyramidal cell soma and dendrite, $i = 1,...,4$. I denotes the interneuron soma.

4.4 Volume fraction redefinition

In order to conform to the canonical definition used in experimental studies and other computational frameworks, the size of the ECS is here estimated by the ratio α between the extracellular and the total space volume:

$$\alpha = \frac{V_o}{V_{tot}} = \frac{V_o}{V_o + V_i} \tag{4.5}$$

where V_i, V_o and V_{tot} denote the intra-, extracellular and total volumes, respectively. In the model α is chosen to be 0.131, as determined experimentally by McBain et al. in [63] for CA1 pyramidal cells when $[\mathrm{K}^+]_o = 3.5$ mM. From (4.5) it follows that the extracellular space volume for a given cell compartment is given by

$$V_o = \frac{\alpha}{1-\alpha} V_i = \beta V_i \tag{4.6}$$

with $\beta = \frac{\alpha}{1-\alpha} = \frac{0.131}{1-0.131}$ ~0.15.

4.5 Cells biophysics

Passive electrical properties of all model cells are as in the former version. Reversal potentials of K^+, Na^+, Cl^-, and Ca^{2+} obey equation (3.2), and leak currents for K^+, Na^+, and Cl^- have the mathematical expressions (3.3) – (3.5). The specific axial resistance R_a and specific membrane capacitance C_m parameters take the values given in Section 3.2. The resting membrane potential is -62 mV in pyramidal cells and -70 mV in the interneuron. Based on R_a and pyramidal cells geometry, the somatodendritic coupling conductance g_c was calculated to be 1.5 mS.

The four pyramidal cells have the same active currents as in the original model: I_{NaT}, I_{Kdr}, I_{CaL}, I_{KAHP}, and I_{KC} in both compartments; I_{NaP} and I_{KM} in somas. The interneuron soma has the I_{NaT} and I_{Kdr} currents. Conductances, activation curves, time constants and gating exponents are given in Gentiletti et al. [64].

4.6 Synapses and network topology

The four pyramidal cells and the interneuron are synaptically connected as in Fig. 4.4. In particular:

- all pyramidal cells receive background input modeled as a Poisson spike train, different in each cell, activating an excitatory synapse placed in the middle of each pyramidal dendrite at a rate of 5 Hz (black lines in Fig. 4.4);
- an inhibitory $\mathrm{GABA_A}$ synapse receiving input from the interneuron is placed in the middle of each pyramidal soma (green lines);
- four excitatory AMPA synapses simulating the excitatory feedback from principal neurons are placed in the middle of the interneuron (purple lines);
- three excitatory AMPA synapses simulating mutual excitatory interactions between principal neurons are placed in the middle of each pyrami-

dal dendrite (orange lines, only three of such connections outgoing from a single cell are shown, the remaining are omitted for graphic simplicity).

The time course of synaptic conductances is modeled with the double exponential function given in equation (3.6), where $g_{max} = weight \times factor$, $factor$ being defined so that the normalized peak is 1. The rise and decay time constants are $\tau_1 = 2$ ms and $\tau_2 = 6$ ms respectively for all synapses. Synaptic weights and reversal potentials for all connections are given in Table 4.1. As in the former setup, inhibitory synaptic transmission is made dependent on chloride and bicarbonate. The inhibitory synaptic reversal potential E_{GABAA} is as in equation (3.7). A synaptic inhibitory response is generated in postsynaptic cells when the interneuron membrane potential crosses the threshold value of -10 mV.

Synaptic action	Type	Synaptic weight (μS)	Reversal potential (mV)
Background activity	E	0.0005	0
Inhibition	I	0.0003	E_{GABAA} – eq. (3.7)
Excitatory feedback	E	0.001	0
Mutual interaction	E	0.0006	0

Table 4.1: Synaptic weights and reversal potentials in the extended model. “E” and “I” stand for “excitatory” and “inhibitory”, respectively.

4.7 Non-synaptic mechanisms

The extended representation includes the same non-synaptic mechanisms implemented in the minimal model:

- accumulation of K^+, Na^+, Ca^{2+}, Cl^- and A^- ions in all intra- and extracellular compartments modeled according to equation (3.8);

- diffusion between compartments (longitudinal diffusion), intra- or extracellular, in pyramidal cells, based on equation (3.14), for K^+, Na^+, Ca^{2+}, and Cl^-; diffusion constants as in [64];

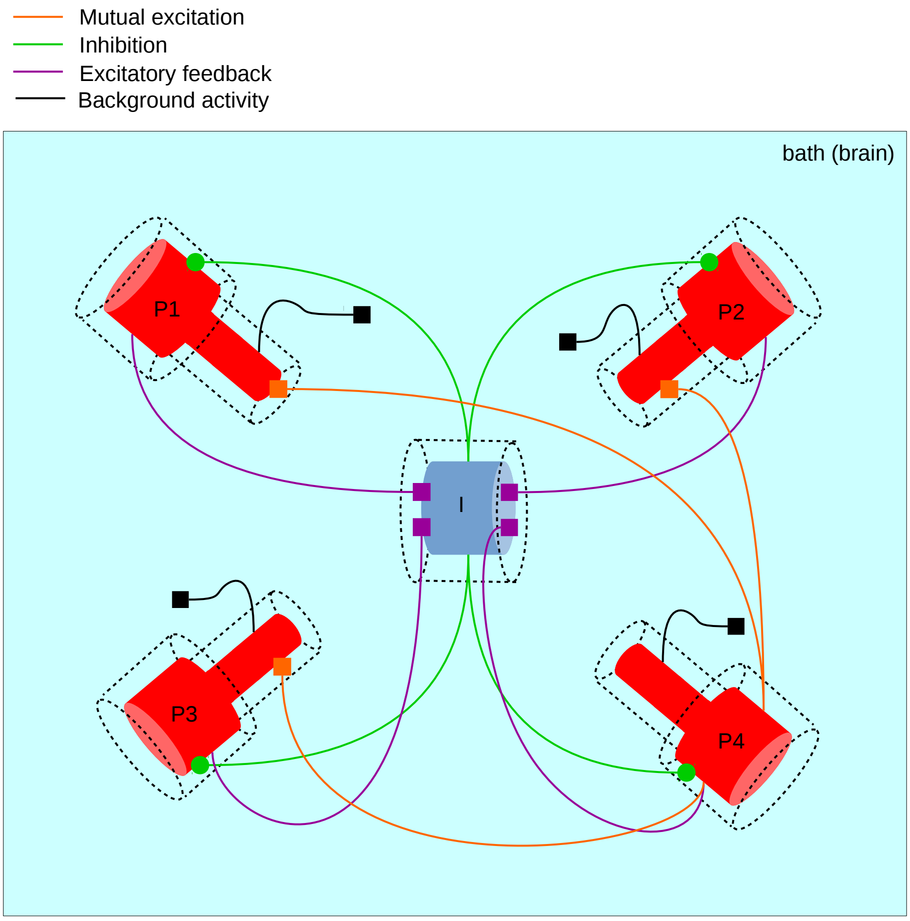

Figure 4.4: Extended model synaptic network. Four different types of synaptic connection are implemented: excitatory background input (black lines); inhibitory synaptic input from the interneuron to pyramidal cells (green lines); excitatory feedback from principal neurons to the interneuron (purple lines); one-to-all excitatory synapses between pyramidal cells (orange lines, only 3 out of 12 total connections are shown).

- diffusion to the bath implemented in all cells governed by equation (3.15) for K^+, Na^+, and Cl^-; diffusion constants and scaling factor as in [64];
- Na^+-K^+ pump in all compartments modeled using equations (3.9) – (3.11); parameter $I_{max} = 0.01\ \mathrm{mA/cm^2}$, Michaelis' constants for Na^+ and K^+ as in the former version;
- K^+-Cl^- KCC2 cotransporter in pyramidal cells; potassium and chloride currents defined by equations (3.12) and (3.13) respectively, cotransporter strength parameter as previously;
- glial buffering of $[K^+]_o$ in all extracellular compartments according to

equations (3.16) – (3.18); initial conditions and rate constants as in [64].

In addition, diffusive exchange between neighboring extracellular spaces, calcium pump and buffering and volume changes are incorporated, as described below.

4.7.1 Ion exchange between shells

In real brain tissue ion diffusion between neighboring extracellular regions takes place, referred to as *radial diffusion*. In the extended *in silico* representation, extracellular compartments are regarded as concentric “shells” around neurons. Radial diffusion between adjacent shells is modeled for K^+ and Na^+ ions only, and is described by the following differential equation based on Fick’s first law:

$$\frac{d[X]_{o,i}}{dt} = \frac{D_X \times \sum_{j=1}^{N}([X]_{o,j} - [X]_{o,i}) \times S_{ij}}{dr_i \times V_i} \tag{4.7}$$

where $[X]_{o,i}$ is the extracellular concentration of species X in shell i, and the sum is made over the N bordering shells as depicted in Fig. 4.5. The i-th shell extracellular volume V_i and thickness dr_i are expressed as functions of the intracellular compartment radius r_i and length L_i, and are given by $V_i = \beta\pi r_i^2 L_i$ and $dr_i = r_i(\sqrt{\beta+1} - 1)$. S_{ij} is the surface contact area between shells i and j, defined as the area of the lateral surface subtended by the inner diameter in shell j which is orthogonal to the axis connecting the compartments centers; this is calculated to be ∼15% of shell i total outer surface. Here again the electrostatic drift of ions is neglected, as the contribution to ion movement due to electric potential gradients in the extracellular space is small compared to diffusion.

4.7.2 Calcium pump and buffer

Calcium pump and buffer changing intracellular Ca^{2+} are modeled according to Somjen et al., 2008, [25]. The calcium pump extruding Ca^{2+} from cells is

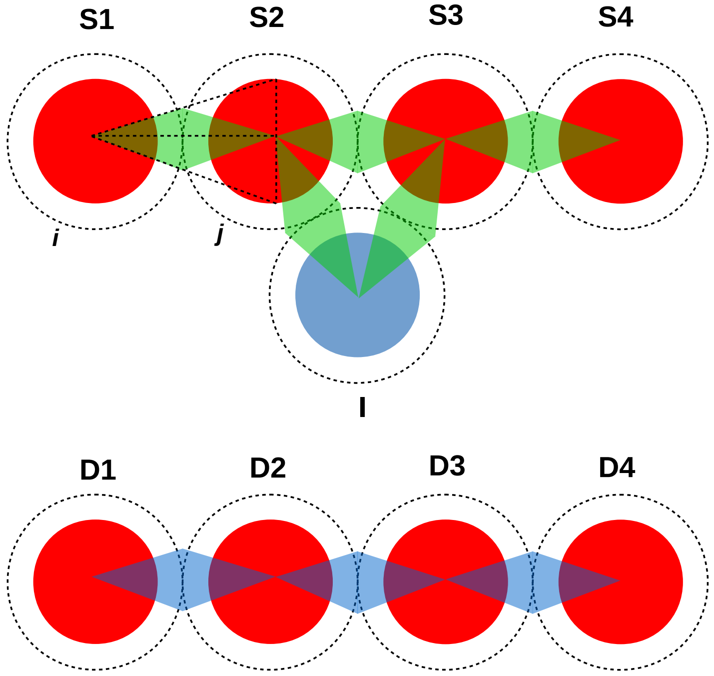

Figure 4.5: Exchange of K^+ and Na^+ ions between shells surrounding somatic and dendritic compartments. The contact surface area between two neighboring shells i and j is calculated to be ∼15% of shell i total outer surface. Si and Di indicate respectively the i-th pyramidal cell soma and dendrite, i = 1,...,4. I denotes the interneuron soma.

modeled as a Ca^{2+} transmembrane current:

$$I_{CaPump} = \frac{I_{max}}{1 + \frac{K_{pump}}{[\mathrm{Ca}^{2+}]_i}} \tag{4.8}$$

with $I_{max} = 2.55$ mA/cm^2 and $K_{pump} = 0.0069$ mM. Intracellular Ca^{2+} is buffered by a first order chemical Ca^{2+} buffer having total concentration $[B]_i$ and an equilibrium constant K_d. Calcium buffering is fast and assuming equilibrium conditions the relationship between total and free intracellular calcium concentration, $[\mathrm{Ca}^{2+}]_{i,tot}$ and $[\mathrm{Ca}^{2+}]_i$, is given by Borgdorff, 2002 [65]:

$$[\mathrm{Ca}^{2+}]_{i,tot} = [\mathrm{Ca}^{2+}]_i \frac{[B]_i + K_d + [\mathrm{Ca}^{2+}]_i}{K_d + [\mathrm{Ca}^{2+}]_i} \tag{4.9}$$

where $[B]_i = 1.562\ \mathrm{mM} \times (V_{i,rest}/V_i)$, V_i is the intracellular compartment volume, $V_{i,rest}$ is the intracellular compartment volume at rest, and $K_d = 0.008$ mM.

4.7.3 Cell volume dynamics

It has been observed experimentally that neurons swell during a wide variety of pathologies, including trauma, ischemia, hypoxia, seizures, and spreading depression ([29], [66], [67]). Cell volume changes can in fact even occur during normal activity, and the magnitude of neuronal swelling during individual action potentials has been estimated ([68], [69]).

The driving force causing neuron volume to vary is an imbalance between the intra- and extracellular total concentrations [70], and the actual physiological mechanism that translates concentration disproportions into swelling is an influx of water across the neuronal membrane which makes the cell expand. Volume changes are modeled based on Somjen et al., 2008, [25]. To quantify the concentration gradient between intra- and extracellular compartments, the intra- and extracellular *bulk concentrations* are defined as

$$\Pi_i = [\mathrm{K}^+]_i + [\mathrm{Na}^+]_i + [\mathrm{Cl}^-]_i + [\mathrm{Ca}^{2+}]_i + [\mathrm{HCO}_3^-]_i + [\mathrm{A}^-]_i \tag{4.10}$$

$$\Pi_o = [\mathrm{K}^+]_o + [\mathrm{Na}^+]_o + [\mathrm{Cl}^-]_o + [\mathrm{Ca}^{2+}]_o + [\mathrm{HCO}_3^-]_o + [\mathrm{A}^-]_o \tag{4.11}$$

When concentration gradients are maintained and cells are at rest, the osmotic gradient is null and

$$\Pi_i = \Pi_o \tag{4.12}$$

During epileptic seizures ion concentration gradients oscillate, and if $\Pi_i > \Pi_o$ a net flux of ions into the cells is generated, disrupting equilibrium. To compensate for the imbalance that occurs, the cells swell. The breakdown of ion gradients can also be associated with a condition where $\Pi_i < \Pi_o$, corresponding to cell shrinkage [71]. In the model cells, volume constraints are set: the extracellular space volume (V_o), initially 15% of the intracellular volume (V_i), is not allowed to diminish beyond 4%; the intracellular space can reduce up to 90% of the initial volume. For each compartment conservation of total volume must be fulfilled:

$$V_{tot} = V_i + V_o \tag{4.13}$$

The rates of intra- and extracellular volume changes are proportional to the difference in osmotic pressure between intra- and extracellular compartments:

$$\frac{dV_i}{dt} = \Delta \tag{4.14}$$

$$\frac{dV_o}{dt} = -\Delta \tag{4.15}$$

where

$$\Delta = c\frac{(\Pi_i - \Pi_o)}{\tau} \tag{4.16}$$

and $\tau = 250$ ms. The constant c is introduced for units conversion and is equal to 1 μm^3/mM, hence units of Δ are μm^3/ms. Volume changes affect concentrations but not the total mass of each ion within a compartment. Conservation of mass requires the following additional fluxes

$$J^i_{X,vol} = -\frac{\Delta}{V_i}[X]_i \tag{4.17}$$

$$J^o_{X,vol} = \frac{\Delta}{V_o}[X]_o \tag{4.18}$$

to be incorporated into the right-hand side of equation (3.8) for each ion species X.

4.8 Initial concentrations and equilibrium without stimulation

When no external stimulation is applied equilibrium in the model results from the interplay between leak and active currents, ion pumps, KCC2 cotransporter, ion buffering and diffusion. Initial values of $[\mathrm{Na}^+]_i$, $[\mathrm{Ca}^{2+}]_i$, $[\mathrm{Na}^+]_o$, $[\mathrm{K}^+]_o$,

Ion species	Intracellular (mM)	Extracellular (mM)
K^+	136.5	3.5
Na^+	10	140
Cl^-	3.5	136.5
Ca^{2+}	5×10^{-5}	2
HCO_3^-	15	11
A^-	128	0

Table 4.2: Initial intra- and extracellular concentrations for all ion species in all model cells.

$[\mathrm{Ca}^{2+}]_o$ and $[\mathrm{A}^-]_o$ are based on Somjen et al., 2008, and the initial value of $[\mathrm{HCO}_3^-]_i$ is according to Doyon et al. 2011. Chloride concentraions were set to satisfy thermodynamic equilibrium of KCC2, i.e., $[\mathrm{Cl}^-]_o = [\mathrm{K}^+]_i$ and $[\mathrm{Cl}^-]_i = [\mathrm{K}^+]_o$, giving $E_{Cl} = E_K$. The remaining ones, i.e., $[\mathrm{K}^+]_i$, $[\mathrm{A}^-]_i$ and $[\mathrm{HCO}_3^-]_o$, were solved to fulfill electroneutrality and osmotic equilibrium conditions (eq. (4.1) – (4.2) and (4.12) respectively):

$$[\mathrm{K}^+]_i = \frac{-3[\mathrm{Ca}^{2+}]_i + 3[\mathrm{Ca}^{2+}]_o + 2[\mathrm{K}^+]_o - 2[\mathrm{Na}^+]_i + 2[\mathrm{Na}^+]_o}{2} \tag{4.19}$$

$$[\mathrm{A}^-]_i = \frac{[\mathrm{Ca}^{2+}]_i + 3[\mathrm{Ca}^{2+}]_o - 2[\mathrm{HCO}_3^-]_i + 2[\mathrm{Na}^+]_o}{2} \tag{4.20}$$

$$[\mathrm{HCO}_3^-]_o = -[\mathrm{A}^-]_o + 2[\mathrm{Ca}^{2+}]_o - [\mathrm{K}^+]_i + [\mathrm{K}^+]_o + [\mathrm{Na}^+]_o \tag{4.21}$$

As a result, the initial concentrations are as in Table 4.2. As in the minimal model, it should be noted that ion concentrations and membrane potentials at rest deviate slightly from perfect equilibrium conditions, both with and without background excitatory synaptic input. This is due to the presence of ion pumps, ion buffers and diffusion, which induce small oscillations around the baseline values that cannot be exactly compensated.

4.9 LFP calculation

Local field potentials are calculated in the new model based on all transmembrane currents in all cells using the following equation (Nunez and Srinivasan, 2006, [56]):

$$\phi(r,t) = \frac{1}{4\pi\sigma}\sum_{n=1}^{N}\frac{I_n(t)}{\mid r - r_n \mid} \tag{4.22}$$

where I_n is a point current source at position r_n, taken as a compartment midpoint position, r is the electrode position, and $\sigma = 0.3$ S/m is the extracellular conductivity (Linden et al., 2014, [72]). The electrode is located in the middle of the somatic layer of interneuron and pyramidal cells, about 16 μm from the soma centers of two neighboring pyramidal cells. Currents from the interneuron are taken with the weight 0.2 to decrease their contribution. Also, the influence of the injected current on LFP is removed. The amplitude of the simulated LFP signal is an order of magnitude smaller than in the experimental data. This is partly due to current point-source approximation and partly because of the small number of cells in the modeled network.

4.10 Simulation results

All model equations are integrated in the NEURON environment with a fixed integration step of 0.025 ms. Seizure-like events simulated with the extended model are shown in Fig. 4.6. The ramp current triggering the epileptic episode starts depolarizing the interneuron at second 60 (Fig. 4.6C, blue trace), producing fast spiking at an initial rate of ∼270 Hz and generating small amplitude fast activity in the LFP signal (Fig. 4.6A). The sustained interneuronal discharge enhances extracellular potassium diffusing to the pyramidal cells network, and gives rise to their irregular firing after about 10 seconds since seizure onset (Fig. 4.6B, only one out of four voltage traces is shown). The tonic phase of the seizure is also reflected in the LFP signal. As the ictal event progresses, the firing regime in both pyramidal cells and interneuron evolves into bursting. Burst discharges keep being fired with gradually decreasing frequency until epileptic activity in the network ceases spontaneously, resulting in a period of silence lasting about 30 seconds. At second ∼150 the background activity reemerges in principal cells, and slowly settles back around the baseline firing rate.

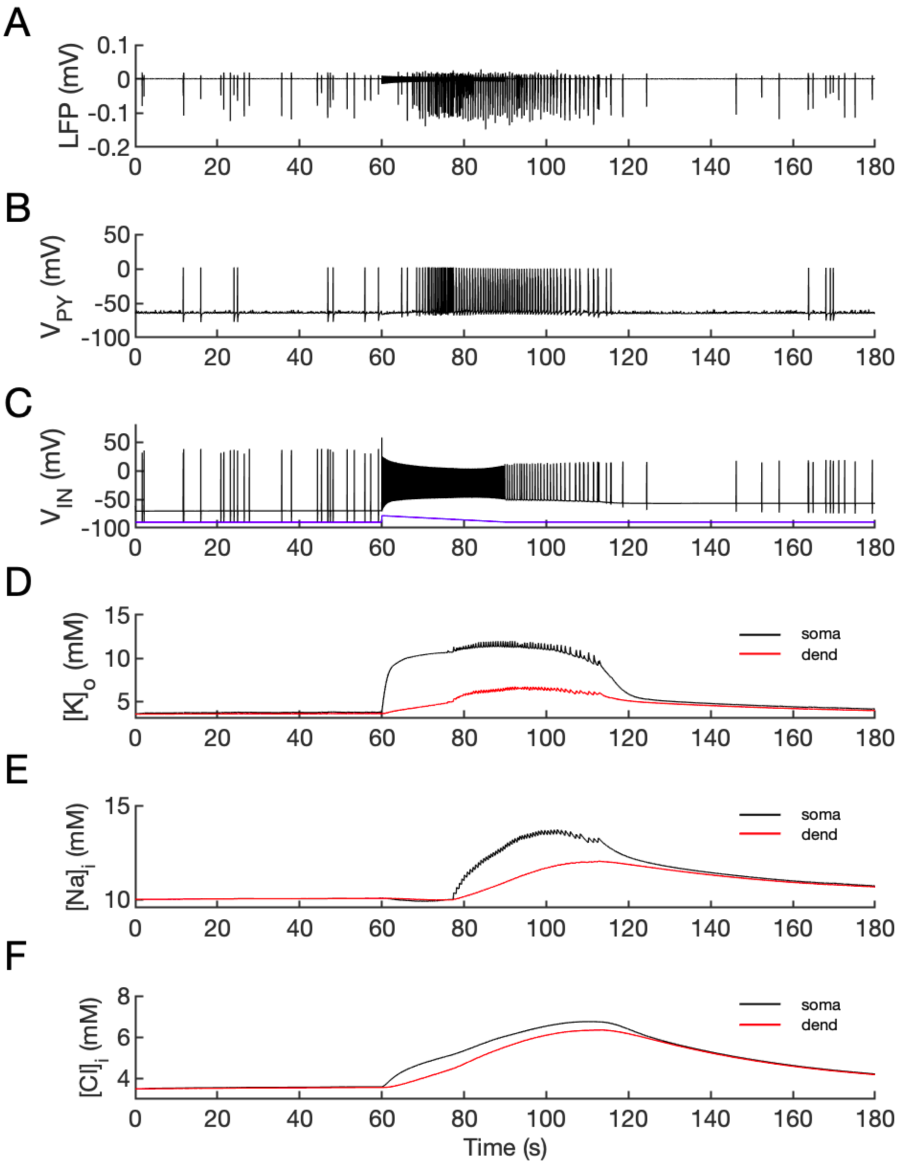

Figure 4.6: Model behavior during seizure-like episodes. A: LFP signal, B: pyramidal cell soma membrane potential, C: interneuron membrane potential, D: extracellular potassium concentration, E: pyramidal cell intracellular sodium concentration, F: pyramidal cell intracellular chloride concentration. PY and IN stand for pyramidal neuron and interneuron respectively. The fast spiking phase in pyramidal cells (B, second 70 to around second 77) is associated with the sharp rise of $[K^+]_o$ (D) triggered, in turn, by the strong firing of the interneuron (C). Tonic firing switches into bursting after about 17 seconds from seizure initiation. At approximately second 120 the seizure terminates and a transient window of diminished neuronal excitability lasting 30 seconds is observed in all cells, as well as in the LFP signal (A-C). Alongside seizure evolution, ion concentrations exhibit significant shifts from the baseline values (D-F).

In Fig. 4.7 experimental recordings (Fig. 4.7A) and seizure patterns obtained with the new model (Fig. 4.7B) are compared, including the experimen-

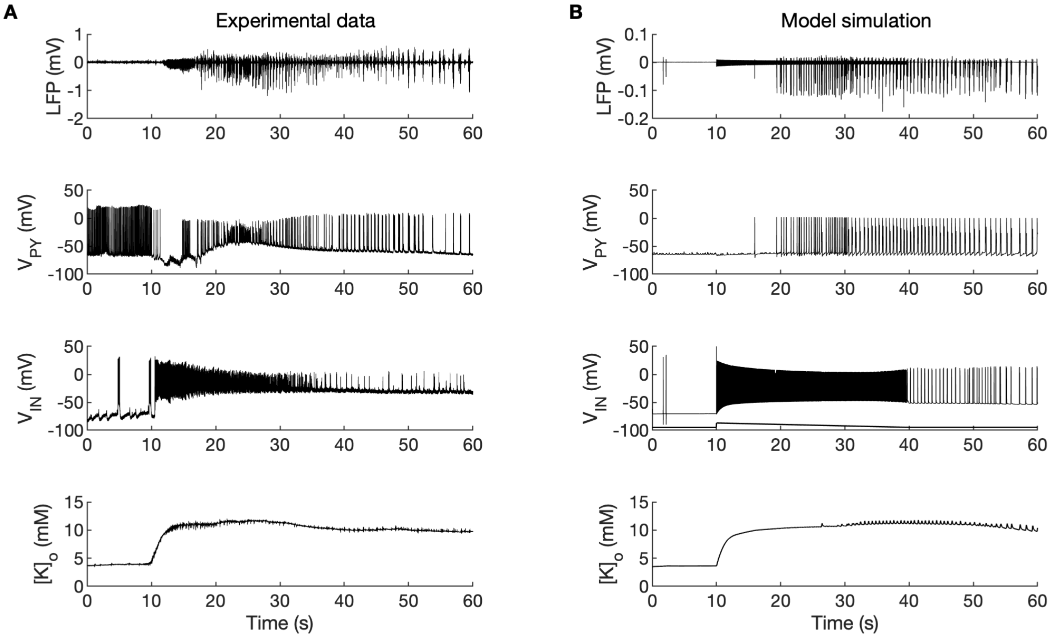

Figure 4.7: Experimental data (A) and extended model simulation (B). From top to bottom: LFP signal, pyramidal cell soma and interneuron voltage traces, extracellular potassium. During the experiment, the pyramidal cell in A was stimulated with a positive current to emphasize the role of inhibitory interneurons (Gnatkovsky et al, 2008, [28]) - not reproduced by the model.

tal and the *in silico* LFP signals. Here the seizure termination phase is not visible, as each of the experimental traces comes from different seizures and they don't terminate at the same time. Besides, seizure termination will be analyzed later in Section 4.10.4. As explained in Chapter 2, the strong preictal firing of the pyramidal cell in the experimental recording (Fig. 4.7A, V_{PY} trace, second 0 to 10), is an artificially triggered response to highlight synaptic inhibition at seizure onset, and it is not included in the model. The experimental traces have been described in detail in Sections 2.2.1 and 3.6. Here again it is noticeable that the simulation results match in many regards the experimental data, including LFP signal characteristics, cellular firing patterns and extracellular potassium time course.

The cells membrane voltage time evolution during epileptic discharges is coupled to changes of the intra- and extracellular ion concentrations. While in Chapter 3 the main focus is how extracellular K^+ ions shape seizure dynamics, here the role of Cl^- and Na^+ ions is also analyzed. In particular, the

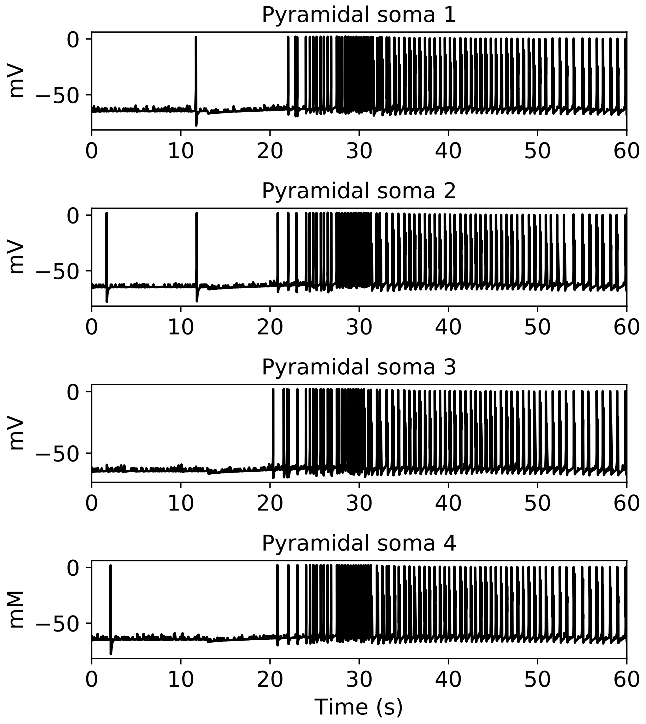

Figure 4.8: Intracellular voltage traces of all pyramidal somas. Due to the mutual synaptic interactions between principal neurons, all cell voltages display a similar qualitative and quantitative time course.

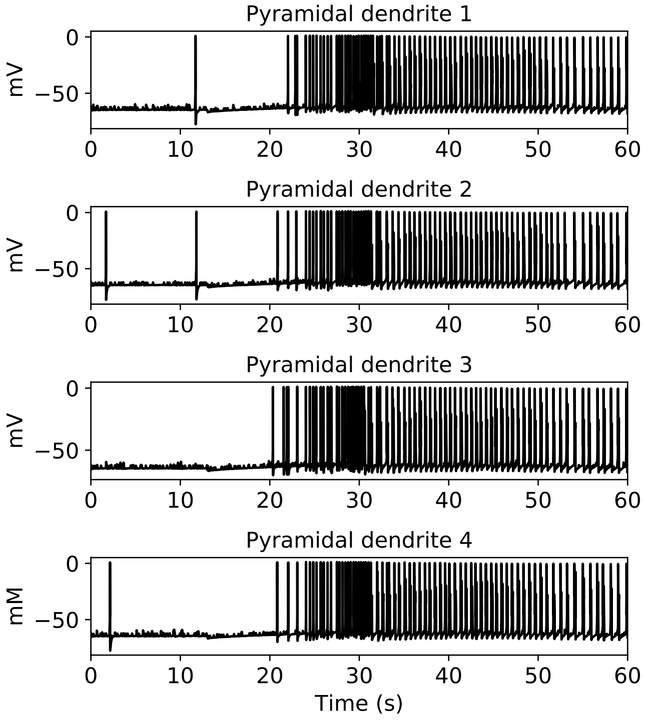

Figure 4.9: Intracellular voltage traces of all pyramidal dendrites.

contribution of intracellular Cl^- and intracellular Na^+ ions to seizure activity in pyramidal cells is addressed in Sections 4.10.1 and 4.10.4, respectively. Simulation results show that:

- $[\mathrm{K}^+]_o$ sharply increases in somas at seizure onset, stays elevated during the tonic and bursting phase and decreases towards the end of the episode (Fig. 4.6D);
- $[\mathrm{Na}^+]_i$ increases during the tonic phase in both somatic and dendritic pyramidal compartments, is steadily maintained at high level during bursting and diminishes around the offset of the seizure (Fig. 4.6E);
- $[\mathrm{Cl}^-]_i$ progressively increases since seizure onset and starts decreasing only when epileptic activity terminates (Fig. 4.6F).

4.10.1 The role of $[\mathrm{Cl}^-]_i$

In order to assess the role of intracellular chloride, chloride dynamics was excluded from the model, and simulation results thus obtained were compared to the results with Cl^- dynamics present (Fig. 4.10). To remove the stochastic component, this analysis does not consider the excitatory background input to pyramidal cells. Chloride accumulation in principal neurons depends on the combined effect of Cl^- currents and the KCC2 cotransporter, the latter being related to both chloride and potassium concentrations. It is here important to notice that, as predicted by equations (3.12) and (3.13), the direction of K-Cl cotransport operated by the KCC2 protein is determined by the ratio $r = [\mathrm{K}^+]_i[\mathrm{Cl}^-]_i/[\mathrm{K}^+]_o[\mathrm{Cl}^-]_o$. In particular,

- if $[\mathrm{Cl}^-]_i > [\mathrm{K}^+]_o \;\Rightarrow\; r > 1 \;\Rightarrow$ Cl^- and K^+ ions are extruded from the cell;
- if $[\mathrm{Cl}^-]_i < [\mathrm{K}^+]_o \;\Rightarrow\; r < 1 \;\Rightarrow$ Cl^- and K^+ ions enter the cell;
- if $[\mathrm{Cl}^-]_i = [\mathrm{K}^+]_o \;\Rightarrow\; r \approx 1 \;\Rightarrow$ no cotransport of Cl^- and K^+ ions occurs (equilibrium condition).

With fixed chloride concentrations (Fig. 4.10A), the reversal potentials of chloride (E_{Cl}) and receptor GABA$_\mathrm{A}$ (E_GABAA), blue and red lines in the second panel of Fig. 4.10A, are constant. Therefore:

- interneuronal activity is sustained (Fig. 4.10A, third panel), resulting in the continuous inhibition of pyramidal cells;
- steady firing of the interneuron makes $[\mathrm{K}^+]_o$ rise above the $[\mathrm{Cl}^-]_i$ level, kept fixed at 3.5 mM (Fig. 4.10A, fourth panel);
- K^+ and Cl^- are transported into the cells by KCC2 (Fig. 4.10A, bottom panel), which reduces $[\mathrm{K}^+]_o$;
- as a consequence of $[\mathrm{K}^+]_o$ reduction and continuous inhibition, pyramidal cells stay inactive and the seizure is not generated.

In the reference model, conversely, chloride concentrations dynamically change, and the seizure-like event is produced (Fig. 4.10B, top panel). It shows that intracellular chloride accumulation may have multiple effects on neuronal excitability. As shown in Fig. 4.10B, second panel, when $[\mathrm{Cl}^-]_i$ increases in pyramidal cells the chloride reversal potential E_{Cl} (blue line) becomes elevated, according to equation

$$E_{Cl} = \frac{RT}{zF} \ln\left(\frac{[\mathrm{Cl}^-]_o}{[\mathrm{Cl}^-]_i}\right) = \frac{RT}{F} \ln\left(\frac{[\mathrm{Cl}^-]_i}{[\mathrm{Cl}^-]_o}\right) \tag{4.23}$$

($z = -1$ for Cl^-), and is hence pushed towards the pyramidal membrane potential. This in turn makes the cell more excitable, since the chloride leak current (which is hyperpolarizing) is reduced. Analogously, the GABA$_\mathrm{A}$ reversal potential also increases and approaches the principal neuron membrane potential (red line in Fig. 4.10B, second panel). In this way the postsynaptic inhibitory current diminishes, and excitability is enhanced. Finally, the prevalence of $[\mathrm{K}^+]_o$ over $[\mathrm{Cl}^-]_i$ during ictal activity (Fig. 4.10B, fourth panel) implies that the direction of the KCC2-mediated ions cotransport is, as in Fig. 4.10A, inward. Enhanced chloride accumulation within the cells acts, though, as a repellor of the Cl^- and K^+ inflow, causing $[\mathrm{K}^+]_o$ to increase and building up neuronal excitability (Fig. 4.10B, third panel).

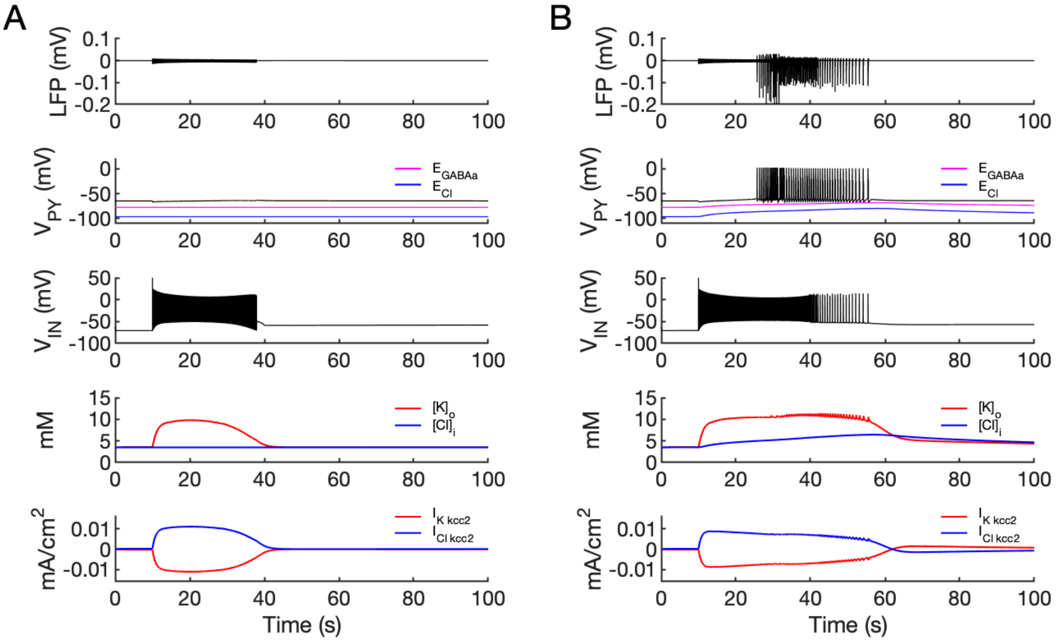

Figure 4.10: Comparison of the model without (A) and with (B) chloride dynamics. From top to bottom: LFP signal, pyramidal cell membrane potential, interneuron membrane potential, extracellular potassium concentration and intracellular chloride concentration, chloride and potassium KCC2 currents in the pyramidal soma. Equilibrium potentials of chloride and GABA$_\mathrm{A}$ are shown in the second panel. The background excitatory input was removed to exclude the stochastic component. A. To remove chloride dynamics, Cl$^-$ accumulation mechanisms were blocked and chloride concentrations were fixed at their reference values. Without chloride accumulation the pyramidal cells remain inhibited by the intereuron discharge. Additionally, elevated [K$^+$]$_o$ and fixed [Cl$^-$]$_i$ promote K$^+$ influx via KCC2 (bottom panel, red), thus lowering [K$^+$]$_o$ and preventing the generation of epileptic activity. B. With chloride accumulation the interneuron discharge leads to increase of both E_{Cl} and E_{GABAA} reducing the hyperpolarizing $I_{Cl,leak}$ and I_{GABAA} currents and enhancing excitability. Increased [Cl$^-$]$_i$ reduces K$^+$ influx via KCC2 leading to higher [K$^+$]$_o$ and initiating the seizure-like event.

4.10.2 Volume changes during *in silico* ictal activity

The cell volume changes observed in the model reflect neuronal geometry dynamics during simulated seizures. Fig. 4.11 – 4.13 show the time course of the intra- and extracellular relative cell volume in the interneuron, pyramidal soma and pyramidal dendrite respectively, throughout the *in silico* ictal event (again, only a single pyramidal soma and a single dendrite are analyzed, the behavior of the other principal cells being analogous). For a certain cell compartment the *relative cell volume* γ, expressed in percentage, is defined as the ratio between the compartment volume V, being function of time t, and the compartment

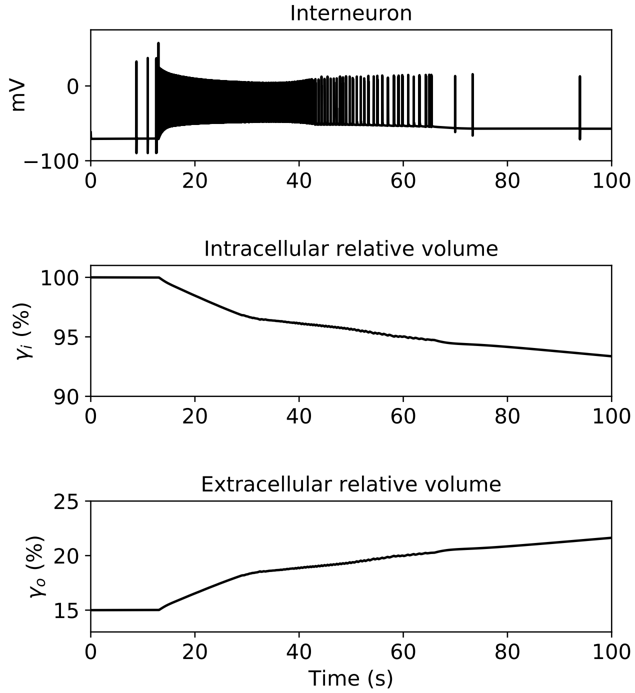

Figure 4.11: Intra- (γ_i) and extracellular (γ_o) relative volume time course in the model interneuron. At seizure onset (second 13) the imbalance deriving from enhanced neuronal activity causes the interneuron to shrink: the intracellular volume (middle panel) decreases and the extracellular volume correspondingly increases (bottom panel). The trend is maintained until the end of the simulation.

intracellular volume at rest $V_{i,rest}$ (constant):

$$\begin{aligned} \gamma_i(t) &= \frac{V_i(t)}{V_{i,rest}} && (4.24) \\ \gamma_o(t) &= \frac{V_o(t)}{V_{i,rest}} = 1 + \beta - \gamma_i(t) && (4.25) \end{aligned}$$

for both intra- (i) and extracellular (o) spaces. The second equality in (4.25) follows from the observation that the total cylinder volume V_{tot} must be conserved, and it equals $V_{tot} = V_i(t) + V_o(t) = V_{i,rest} + V_{o,rest} = V_{i,rest} + \beta V_{i,rest} = (1+\beta)V_{i,rest}$. Therefore:

$$\begin{aligned} \frac{V_{tot}}{V_{i,rest}} &= \frac{V_i(t) + V_o(t)}{V_{i,rest}} = \frac{V_i(t)}{V_{i,rest}} + \frac{V_o(t)}{V_{i,rest}} = && (4.26) \\ &= \gamma_i(t) + \gamma_o(t) = 1 + \beta = 1.15 \end{aligned}$$

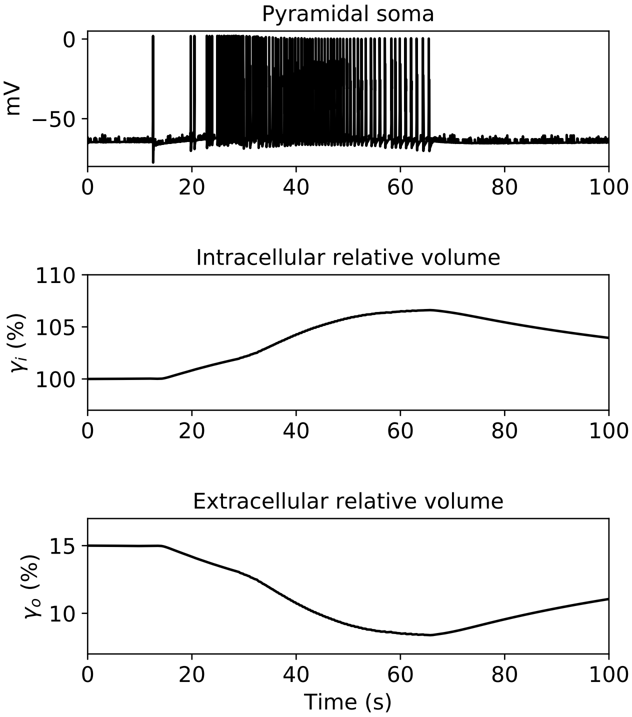

Figure 4.12: Intra- (γ_i) and extracellular (γ_o) relative volume time course in the model pyramidal soma. When epileptic activity is initiated at second 13, the cell compartment begins to swell and increases its initial intracellular volume of ∼8% at seizure termination (second ∼65). After the seizure-like event cessation, intra- and extracellular volumes begin to drift back to preictal levels.

At rest the cell volume does not change, and $\gamma_i = 1$, $\gamma_o = \beta = 0.15$. When $\gamma_i > 1$, it follows from equation (4.25) that $\gamma_o < \beta$, and the cell intracellular compartment swells; conversely if $\gamma_i < 1$, $\gamma_o > \beta$ and the cylinder shrinks. Before seizure onset (second 13 in Fig. 4.11 – 4.13), volume dynamics is quite stable in all compartments, being only influenced by background activity. At seizure onset the imbalance generated by the strong firing causes the interneuron to shrink (Fig. 4.11, middle and bottom panels) and the pyramidal soma and dendrite to swell (Fig. 4.12 and Fig. 4.13). When the seizure-like event terminates around second 65, the pyramidal soma and dendrite relative extracellular volumes reach a minimum value of ∼8% and ∼13.5% respectively, while the interneuron keeps shrinking. During the postictal period the pyramidal cell volumes are being restored towards the baseline values; the interneuron volume, however, steadily decreases until the end of the simulation. Such a behavior results from the current injected into the interneuron and does not relate to

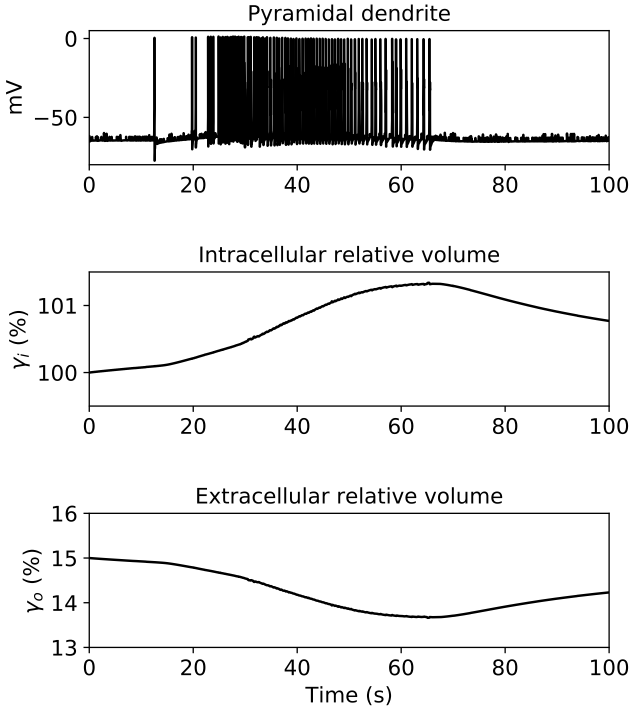

Figure 4.13: Intra- (γ_i) and extracellular (γ_o) relative volume time course in the model pyramidal dendrite displays the same qualitative behavior observed in the pyramidal soma. The maximum increase of the cylinder's initial intracellular volume is of ∼1.5%, attained at seizure termination.

any physiological effects. This was resolved in later versions of the model [64].

4.10.3 Spontaneous bursting activity and bursting mechanism

Bursting is a particular activation pattern of neurons in the central nervous system which differs from regular spiking activity. The experimental bursting phase recorded in the *in vitro* guinea pig brain is analyzed in detail by Trombin et al. in [36]. In the extended model simulation shown in Fig. 4.7 the transition from irregular spiking to bursting regime takes place in pyramidal cells around second 30, similarly as in *in vitro* data. This is shown in Fig. 4.14 for a reference pyramidal neuron soma (top panel). In the interneuron (bottom panel), the transition occurs at second ∼42.5, slightly later than observed experimentally in Fig. 4.7. Throughout the whole bursting phase in the interneuron, firing is characterized by the generation of *quadruplets*, i.e. dis-

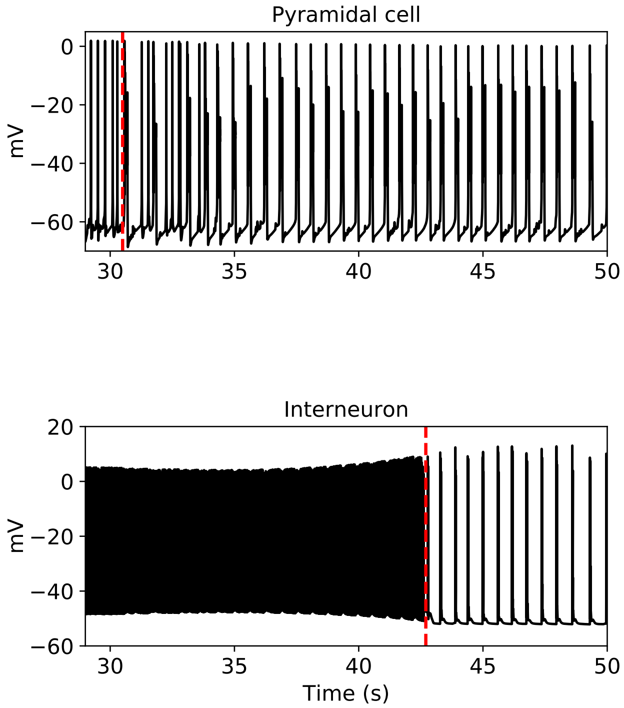

Figure 4.14: Transition from tonic firing to bursting in the extended model, marked by the red dashed vertical lines (detail of the simulation shown in Fig. 4.7). Top panel: pyramidal soma. Bottom: interneuron.

charges composed by four discrete action potentials each, while pyramidal cells give rise to quasi-periodic signals resembling short-lasting (∼140 ms) paroxysmal depolarizing shifts with spikes riding on a depolarization envelope. The average *interburst interval*, i.e. the time interval separating two consecutive bursting events, is estimated in the model pyramidal soma and interneuron to be initially around 700 ms. The average *intraburst interval*, i.e. the interval separating two consecutive spikes within single burts, is estimated to be ∼7 ms in the interneuron. In Fig. 4.15 a detail of the extracellular K^+ trace during the bursting phase in the interneuron (bottom panel, black) and pyramidal soma (bottom panel, red) is compared to the $[K^+]_o$ time course during the simulated seizure (middle). The pyramidal soma and interneuron $[K^+]_o$ traces are almost indistinguishable because of the fast K^+ radial diffusion between extracellular shells mechanism. It can be noticed that the transition to the bursting phase in the pyramidal network at second ~ 30 (marked by the red dashed vertical lines in the top and middle panels of Fig. 4.15) correlates with the appearence

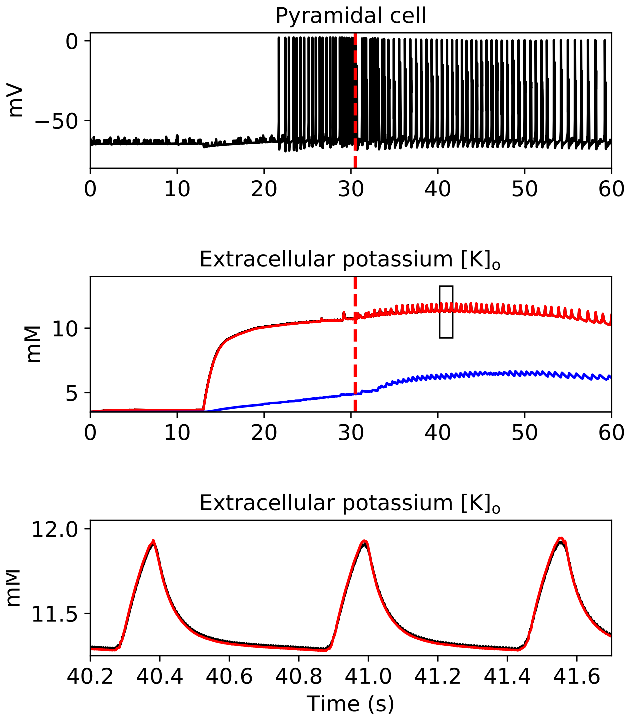

Figure 4.15: Top panel: pyramidal cell voltage trace during the simulated seizure. Middle: pyramidal soma (red), interneuron (black) and pyramidal dendrite (blue) extracellular potassium concentration traces during the simulated seizure. Due to fast extracellular K^+ diffusion in the model, pyramidal soma and interneuron traces almost overlap. Bursting-related behavior is visible since second ~30 (red dashed lines). Bottom: detail of the bursting phase in the pyramidal soma (red) and interneuron (black), as highlighted by the black rectangle in the middle panel (40.2-41.6 seconds). Compared to the irregular spiking phase, when single action potentials are emitted, the number of released K^+ ions during firing of bursts is higher, resulting in sharper $[K^+]_o$ waveforms (amplitude $\sim$ 0.7 mM).

of higher-amplitude $[K^+]_o$ waveforms ($\sim$ 0.7 mM) compared to the tonic firing period, reflecting the increase of K^+ release during each burst with respect to single spikes.

In physiological systems bursting patterns are thought to be generated by the action of two linked subsystems, a fast and a slow one [73]. Most spiking neurons can be forced to burst if artificially stimulated with a current that slowly drives the membrane potential above and below the firing threshold. Many neuronal cells, however, can exhibit an intrinsic bursting behavior, produced by slow membrane currents modulating fast spiking activity. Typically, the slow currents build up during continuous spiking, hyperpolarize the cell and eventually result in the spike train termination. Afterwards, while the cell is quiescent the hyperpolarizing currents slowly decay, the cell recovers and another burst discharge is fired. The bursting signal recorded in the *in vitro* guinea pig brain, as well as the one generated by the extended computational model, have an intrinsic nature. In the model bursting activity critically depends on the interplay between the fast excitatory persistent sodium current I_{NaP} and the slow inhibitory potassium muscarinic current I_{KM}, both present in all pyramidal somas. Fig. 4.16 shows the fast I_{NaP} current and the slow I_{KM} during the bursting phase. In the top panel the I_{NaP} (red curve) and I_{KM} (blue curve) currents time course during the simulated seizure in a reference pyramidal cell is shown. As long as network cells are in the irregular spiking regime and until second ∼30, the dynamics is clearly fast and dominated by the I_{NaP} current. At the transition from tonic firing to bursting, it can be noticed that the peak values of the I_{KM} current increase significantly compared to the irregular spiking phase and start overcoming the I_{NaP} current (bottom panel). The burst generation mechanism in the model can be summarized by the following steps:

- the build up of $[K^+]_o$ during the tonic firing phase reduces the driving force of K^+ currents responsible for membrane repolarization, resulting in weaker hyperpolarizing K^+ currents;
- the subsequent enhanced excitability leads to the generation of bursts, sustained by both transient and persistent sodium currents;
- the prolonged depolarization activates the slow potassium I_{KM} current, which increases during a single burst and eventually repolarizes the membrane, terminating the discharge;
- high $[K^+]_o$ initiates the next burst and the cycle repeats.

Fig. 4.17 illustrates the activation gate of the I_{KM} current conductance during tonic firing (A) and bursting (B) in a pyramidal cell. In each column the cell membrane potential (top) and activation gate of I_{KM} (bottom) are shown. During tonic firing the value of the gating variable $m \approx 0$, and the activation gate is closed. Prolonged depolarization of the cell during bursting leads to gate

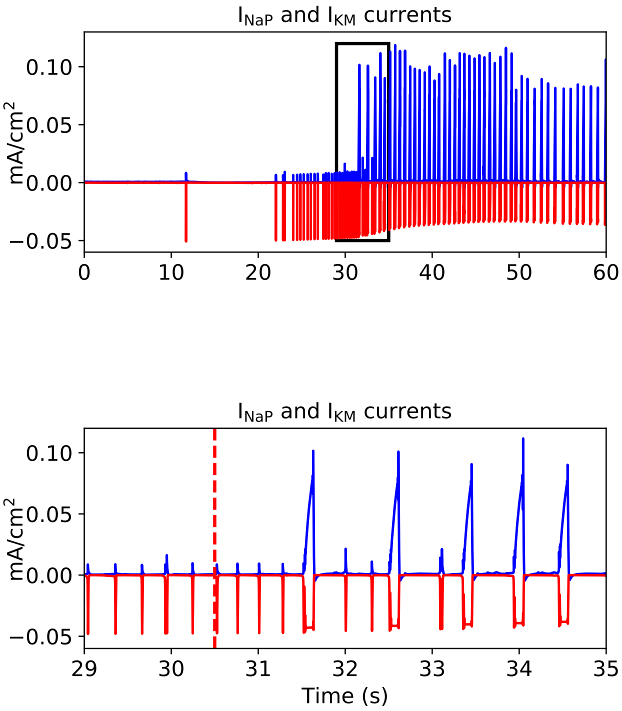

Figure 4.16: Intrinsic bursting activity is generated in the model by the joint action of the I_{NaP} and I_{KM} currents in principal neurons somas. Top panel: I_{NaP} (red) and I_{KM} (blue) currents time course during the simulated seizure in a pyramidal cell soma. During the tonic firing phase I_{NaP} is dominant over I_{KM}. Bottom panel: detail of the current traces as highlighted by the black rectangle in the top panel (29-35 seconds). Soon after spiking switches to bursting at second ~30 (red dashed line), a significant increase of the I_{KM} current peak values is recorded, and slow dynamics (I_{KM}) takes the lead over fast dynamics (I_{NaP}).

opening and I_{KM} current activation, which eventually terminates the burst. For a more in depth analysis of the model dynamics during the bursting phase, see [64].

4.10.4 Seizure termination

Different mechanisms have been suggested to contribute to seizure termination but there is no consensus among researchers regarding which one plays a dominant role. In the model, seizure-like events terminate spontaneously on account of two factors: rise in $[\mathrm{Na}^+]_i$ and decrease of $[\mathrm{K}^+]_o$. Elevated $[\mathrm{Na}^+]_i$ leads to increased Na^+-K^+ pump activity, according to equations (3.9) – (3.11). Both

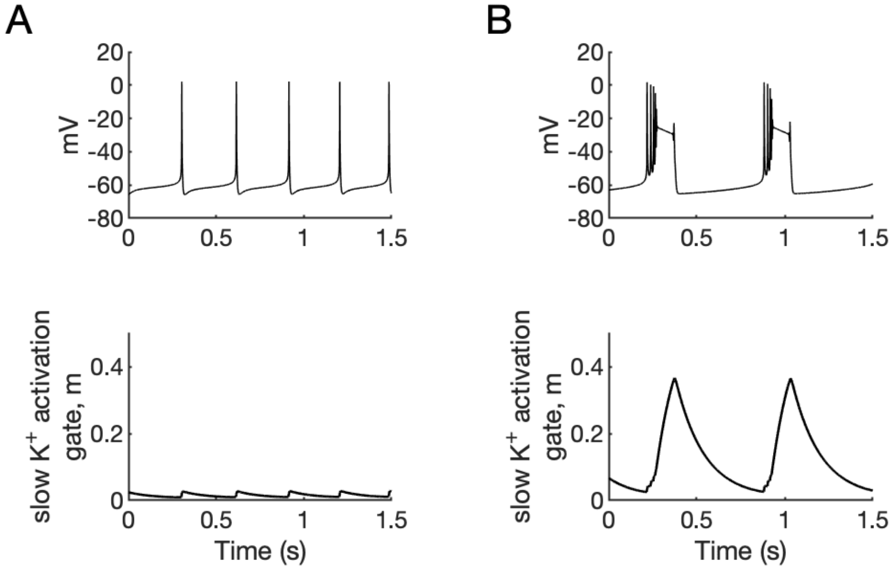

Figure 4.17: Comparison of tonic firing (A) and bursting (B) in a model pyramidal cell. Top: membrane potential. Bottom: activation gate of I_{KM}. Simulations performed using an isolated pyramidal cell model with concentrations of all ions fixed at their reference values except (A): $[K^+]_{o,soma} = 11$ mM, $[K^+]_{o,dend} = 3.75$ mM, (B): $[K^+]_{o,soma} = 11$ mM, $[K^+]_{o,dend} = 5$ mM.

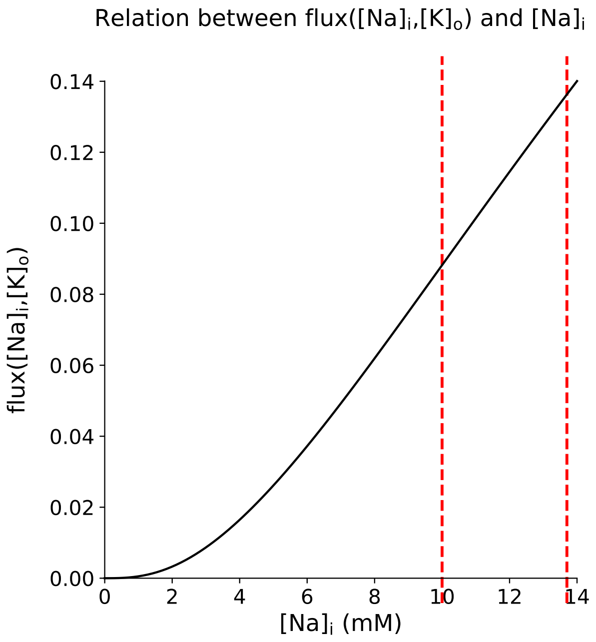

Figure 4.18: Relation between the Na$^+$-K$^+$ pump current and $[Na^+]_i$ in the model cells. The quantity $flux([Na^+]_i, [K^+]_o)$ is dimensionless. In this figure, $[K^+]_o$ is fixed at 10.5 mM. The Na$^+$-K$^+$ pump action strength is positively correlated with the intracellular Na$^+$ concentration, which builds up from 10 mM (baseline level) to 13.7 mM during the simulated seizure (red dashed lines).

I_{Na} and I_K pump currents are proportional to the term $flux([\mathrm{Na}^+]_i, [\mathrm{K}^+]_o)$:

$$flux([\mathrm{Na}^+]_i, [\mathrm{K}^+]_o) = \frac{1}{\left(1 + \frac{Km_K}{[\mathrm{K}^+]_o}\right)^2} \times \frac{1}{\left(1 + \frac{Km_{Na}}{[\mathrm{Na}^+]_i}\right)^3} \tag{4.27}$$

where Km_K and Km_{Na} are constant and $[\mathrm{K}^+]_o$ does not remarkably deviate from high values during sustained ictal activity – for the purpose of this explanation $[\mathrm{K}^+]_o$ can be thought to be fixed at 10.5 mM. It is therefore easy to observe that (Fig. 4.18) as $[\mathrm{Na}^+]_i$ increases from its baseline level (10 mM) up to approximately 13.7 mM, so does $flux([\mathrm{Na}^+]_i, [\mathrm{K}^+]_o)$, resulting in stronger I_{Na} and I_K pump currents. In a single cycle of the Na^+-K^+ pump, three sodium ions are extruded from and two potassium ions are transported into the cell. Accordingly, the pump current is hyperpolarizing. The enhanced pump action

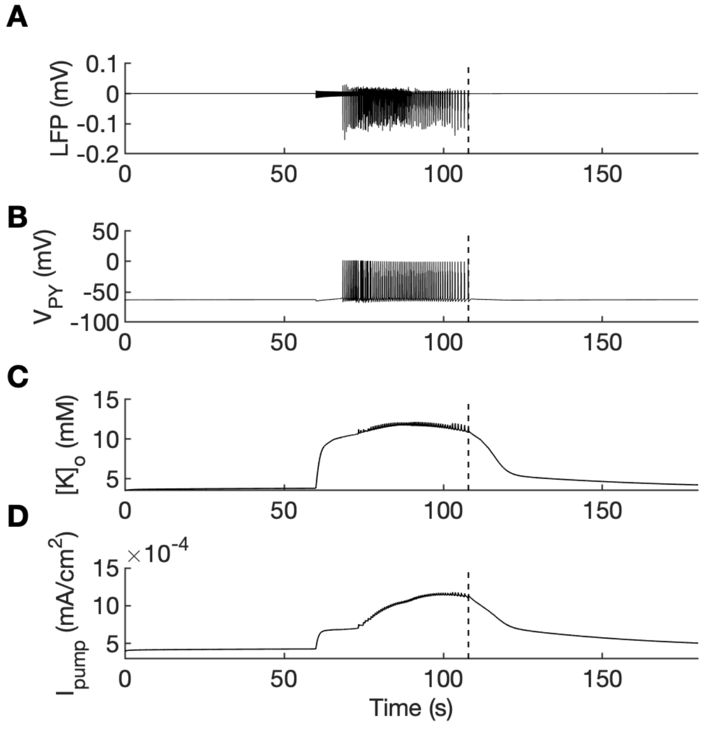

Figure 4.19: Role played by the Na^+-K^+ pump in seizure termination. A. LFP signal. B. Pyramidal cell membrane potential. C. Extracellular potassium in the pyramidal soma. D. Total Na^+-K^+ pump current. In this figure the background input was removed from the simulation to clearly exhibit sudden termination marked by the vertical broken lines. The progressive increase of the total (hyperpolarizing) pump current during the bursting phase, fueled by the intracellular sodium concentration build-up, leads to reduction of neuronal excitability and enhanced $[\mathrm{K}^+]_o$ clearance. As a result, new bursting oscillations are eventually prevented to occur in all neurons and ictal activity terminates.

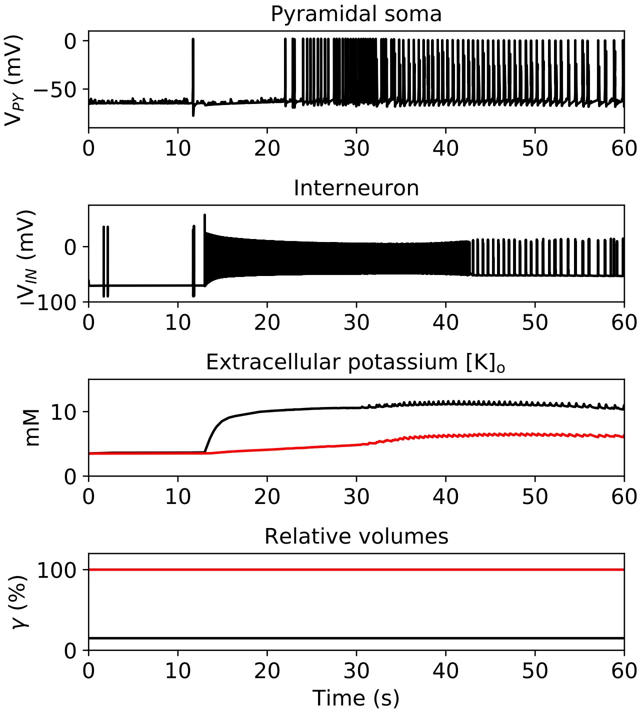

Figure 4.20: Removing volume dynamics from the extended model does not result in noticeable deviations from the main simulation results. From top to bottom: pyramidal soma voltage; interneuron voltage; principal neuron soma (black) and dendrite (red) $[K^+]_o$ traces; intra- (red) and extracellular (black) relative cell volumes, expressed in percentage.

contributes, therefore, to

- reduction of cell excitability
- faster decrease of $[K^+]_o$

These two effects eventually prevent the start of a new burst and lead to the epileptic episode termination. The link between Na^+-K^+ pump and seizure termination is shown in Fig. 4.19. Background excitatory input to pyramidal cells was here removed to eliminate noise sources. Panel D illustrates the time evolution of the total $(I_K + I_{Na})$ pump current, denoted "I_{pump}", during the modeled epileptic event. The vertical dashed line marks seizure offset in each panel. The steady increase of I_{pump} during the bursting phase steadily reduces cells excitability, causing the bursts to progressively slow down and ultimately stop around second 110 (panels A and B).

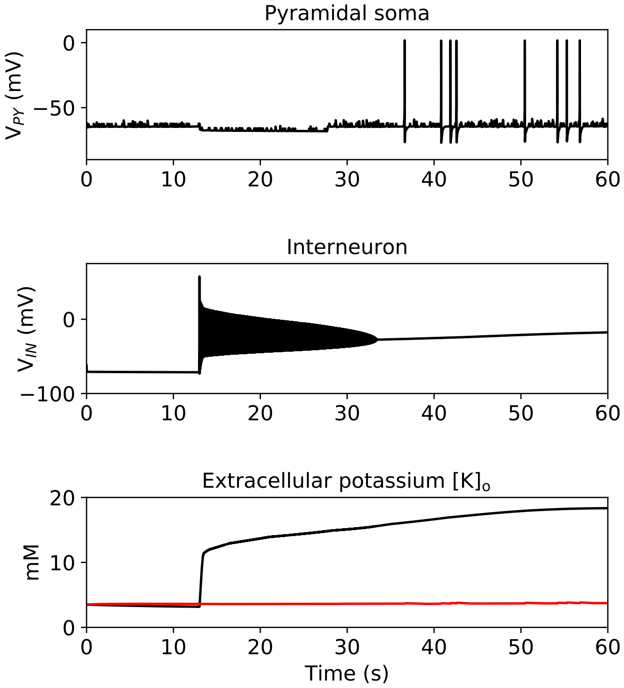

Figure 4.21: Preventing the radial diffusion of K^+ ions between shells results in excessive potassium accumulation within the region surronding the interneuron (bottom panel, black), and allows pyramidal cells to maintain the resting $[K^+]_o$ level (red). As a consequence, the interneuron soon becomes unable to repolarize and enters a block and principal neurons fail to generate seizure-like activity (top).

4.10.5 Selective removal of components in the extended model

Following the same approach as in Chapter 3, simulations were run after excluding from the extended model single biophysiological components. This allows to assess the relevance of the removed mechanisms by comparing the derived model response to the full setup. The role of the components here considered was not analyzed previously, as they are present only in the extended model.

Fig. 4.20 shows the effects of volume changes removal. Fixing both intra- (bottom panel, red line) and extracellular (bottom panel, black) cell volumes in all model compartments does not significantly affect the main simulation: the interneuron (second panel from the top) displays the canonical behavior, as well as the pyramidal cell (top panel). Likewise, the pyramidal soma (third panel from top, black) and dendrite (red) $[K^+]_o$ traces do not appreciably deviate from those of Fig. 4.7.

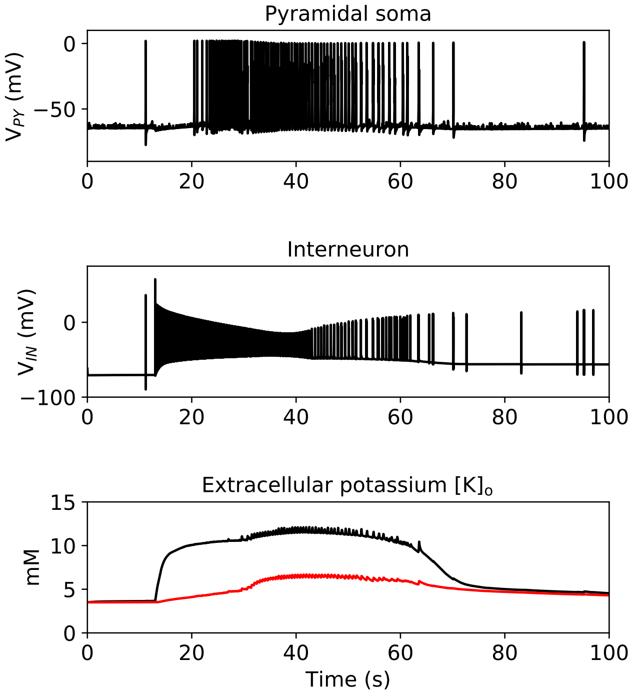

Figure 4.22: Preventing the radial diffusion of Na^+ ions between shells does not radically change the main simulation results. Pyramidal cells voltage (top panel) and soma and dendrite extracellular potassium traces (black and red lines in the bottom panel, respectively) display the usual patterns. The interneuron membrane potential also preserves the canonical behavior, however, the trace upper envelope is lowered during the bursting phase with respect to the reference results (middle). This is due to the decline in $[Na^+]_o$, and thus E_{Na}, caused by the block of sodium ions inflow from adjacent areas.

Neglecting K^+ and Na^+ radial diffusion between neighboring extracellular shells produces the output in Fig. 4.21 and 4.22, respectively. When K^+ ions are not allowed to propagate to adjacent extracellular compartments, the excessive potassium concentration produced by the enhanced interneuron activity cumulates and is retained within the shell surrounding the interneuron. The extracellular potassium concentration in the interneuron (Fig. 4.21, bottom panel, black line) therefore strongly increases, ultimately reaching abnormally elevated values, while in pyramidal neurons it remains close to the baseline level (red line). As a result, the interneuron enters a permanent depolarization block at second ~33 (middle), and pyramidal cells fail to be recruited into ictal activity and only generate isolated, sporadic discharges (top). This indicates that in the extended model the diffusive exchange of K^+ ions between

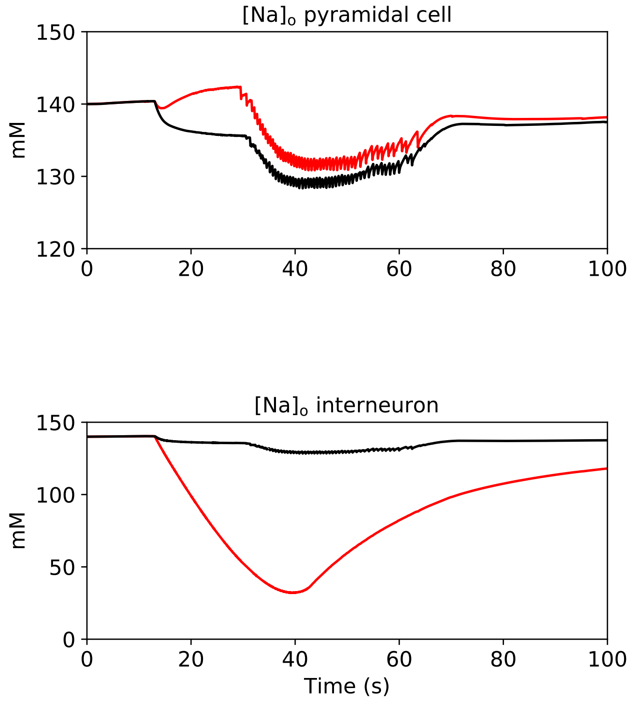

Figure 4.23: Comparison of the model $[\mathrm{Na}^+]_o$ traces with (black lines) and without (red lines) diffusion of Na^+ ions between shells, in pyramidal cells (top) and interneuron (bottom). While $[\mathrm{Na}^+]_o$ is not significantly impacted by diffusion prevention in principal neurons, it is markedly affected in the interneuron.

shells is essential. Conversely, impeding the exchange of Na^+ ions does not lead to considerable alterations with respect to the reference results. Under such conditions, the extracellular Na^+ ions cannot distribute and stay confined to the respective outer-membrane regions. This visibly influences the interneuron spike amplitude during seizure-like activity, as highlighted by Fig. 4.22, middle panel. When the exchange of extracellular Na^+ between shells is allowed (black line in Fig. 4.23), $[\mathrm{Na}^+]_o$ does not diverge substantially from the baseline level. However, when inflow of Na^+ ions from neighboring cells is blocked, the Na^+ ions accumulate inside the cell and the extracellular sodium concentration considerably drops (∼100 mM gradient) until second ∼40, and then starts recovering (red) due to pump activity. As predicted by the Nernst reversal potential equation for sodium, the marked decline in $[\mathrm{Na}^+]_o$ compared to the main simulation is reflected in the interneuron voltage trace. Since $[\mathrm{Na}^+]_o$ has a lower value than in the unaltered model, so does E_{Na}, and therefore the membrane potential trace appears to be more "squeezed" during the bursting

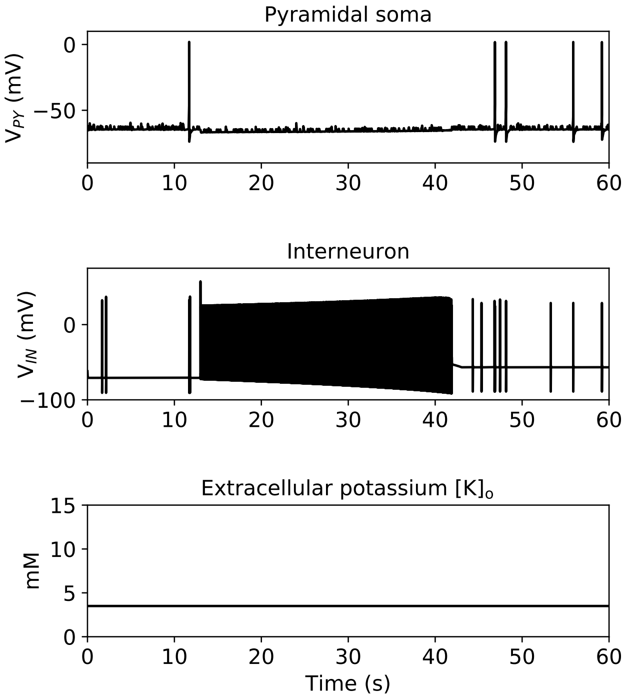

Figure 4.24: Constant ion concentrations in the extended model. When ion dynamics is excluded from computation, the model is unable to reproduce seizure episodes. This confirms the results obtained with the minimal model, i.e. that the incorporation of ion concentration changes is essential to faithfully recreate the experimental traces.

phase (Fig. 4.22, middle). Pyramidal cells, on the other hand, are not significantly impacted by the model variation, and maintain intact both membrane potential behavior (Fig. 4.22, top panel) and $[\mathrm{Na}^+]_o$ time course (Fig. 4.23, top), displaying only relatively low magnitude deviations (∼5 mM) from the reference model sodium concentrations (black versus red line).

Finally, nullifying all ion fluxes leads to the outcome shown in Fig. 4.24. In the absence of ion dynamics the cells in the network can only exchange synpatic inputs, and $[\mathrm{K}^+]_o$ remains constant in every compartment (bottom panel). The intense inhibitory activity promoted by the interneuron (middle) prohibits principal neurons firing, and prevents the development of the seizure event (top). These findings reinforce the results previously obtained with the minimal model, and confirm that real epileptic seizure genesis, evolution and termination as observed in the experimental recordings critically depend on ion concentration changes.

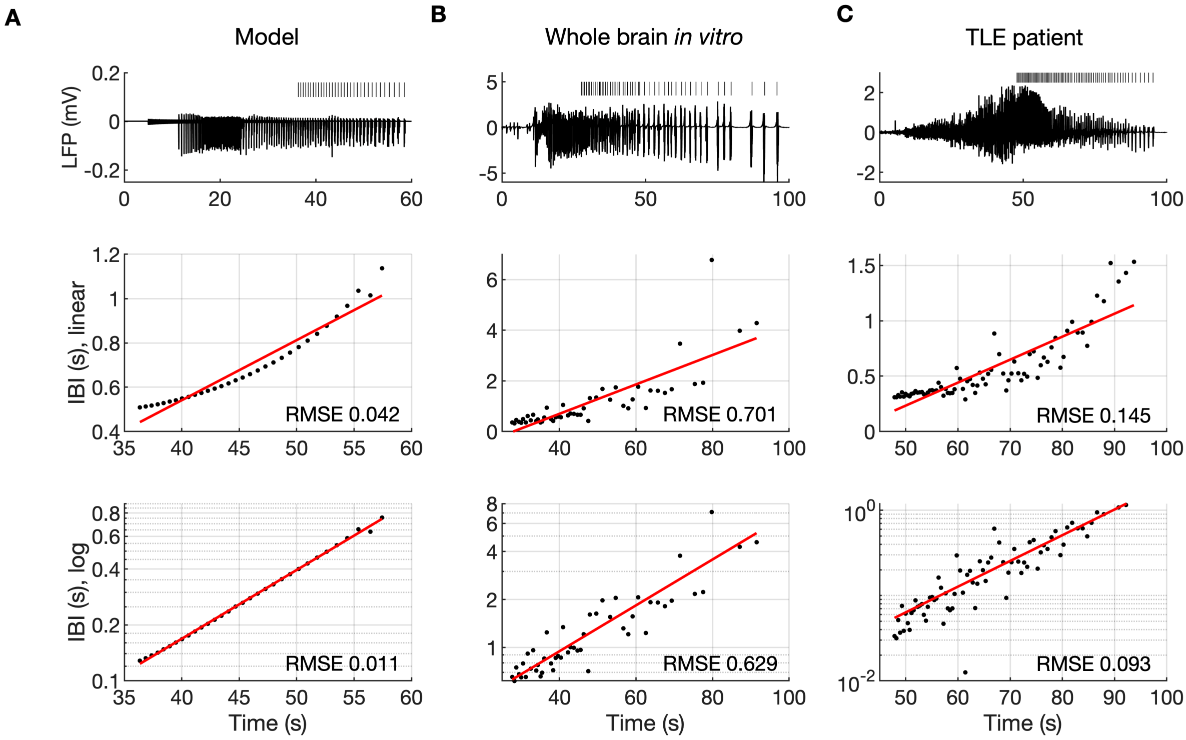

Figure 4.25: Inter-burst interval time course in the model (A), guinea pig brain preparation (B), and human temporal lobe epilepsy (C). Data in C has been kindly made available by Laura Tassi, Epilepsy Surgery Center, Niguarda Hospital, Milano, Italy. Top panel: LFP signal and burst discharges distribution marked by the vertical bars on top of the trace. Middle: IBI length as a function of time, linear scale. Bottom: IBI in logarithmic scale. In all three cases, exponential decay of the bursting frequency is clearly visible from the graphs and confirmed by the root mean square error (RMSE), computed for both linear and exponential fit (red curves). The linear and exponential fits were obtained using the `polyfit` and the `fminsearch` Matlab procedures, respectively.

4.10.6 Model predictions

As observed in previous sections, when the epileptic event approaches its offset in the model, burst discharges are fired with increasingly slow frequency (Fig. 4.6B). Equivalently, the interburst interval (IBI) gets progressively longer. To describe this process quantitatively the scaling law describing the slowing down behavior was analyzed. For this purpose, IBI time distribution data was gathered performing a simulation without the background noise in order to get fluctuation-free IBI data. Furthermore, a depolarizing current of 6 pA was applied to all pyramidal somas to maintain seizure duration as in the model with noise. Simulation results are shown in Fig. 4.25A. The onset of each burst discharge is marked by a vertical bar on top of the LFP trace. Fig. 4.25A middle and bottom panels show the model IBI time course, in linear and logarithmic y-axis scale respectively; the exponential pattern is evident in both graphs. Fig. 4.25B and C illustrate the results of the same analysis using (B) the *in vitro* brain preparation and (C) a human temporal lobe epilepsy sample. The seizure in C was recorded by means of intracerebral electrodes (courtesy of Laura Tassi, Epilepsy Surgery Center, Niguarda Hospital, Milano, Italy). All three IBI datasets were fitted using both linear and exponential models:

$$IBI(t) = A + Bt \qquad (4.28)$$

$$IBI(t) = A + Be^{Ct} \qquad (4.29)$$

The root mean square error (RMSE), which measures the differences between the values predicted by a mathematical model and the observed ones, was computed for each scenario. The lower errors obtained for model (4.29) compared to (4.28) confirm in all cases the exponential growth of the function $IBI(t)$ in time. In this way, the prediction obtained with the computational model was confirmed by the experimental data in two different epileptic systems. It increases confidence that the model has captured the essential properties of the real seizures.

4.10.7 Potential epilepsy therapy

Despite the recent introduction of new antiepileptic drugs, approximately one third of the patients with epilepsy suffer from seizures resistant to pharmacological treatment ([74], [75]). This urges the need for novel, more efficient therapies. Recent studies highlight the promising characteristics of nanomaterials as excellent candidate tools for precision medicine development ([76], [77]). In the context of epilepsy treatment, a nanoparticle system could be possibly employed as an integrated extracellular potassium clearance agent which might successfully control neuronal excitability. This idea was tested by means of the extended model. Artificial potassium regulation was implemented as an ad-

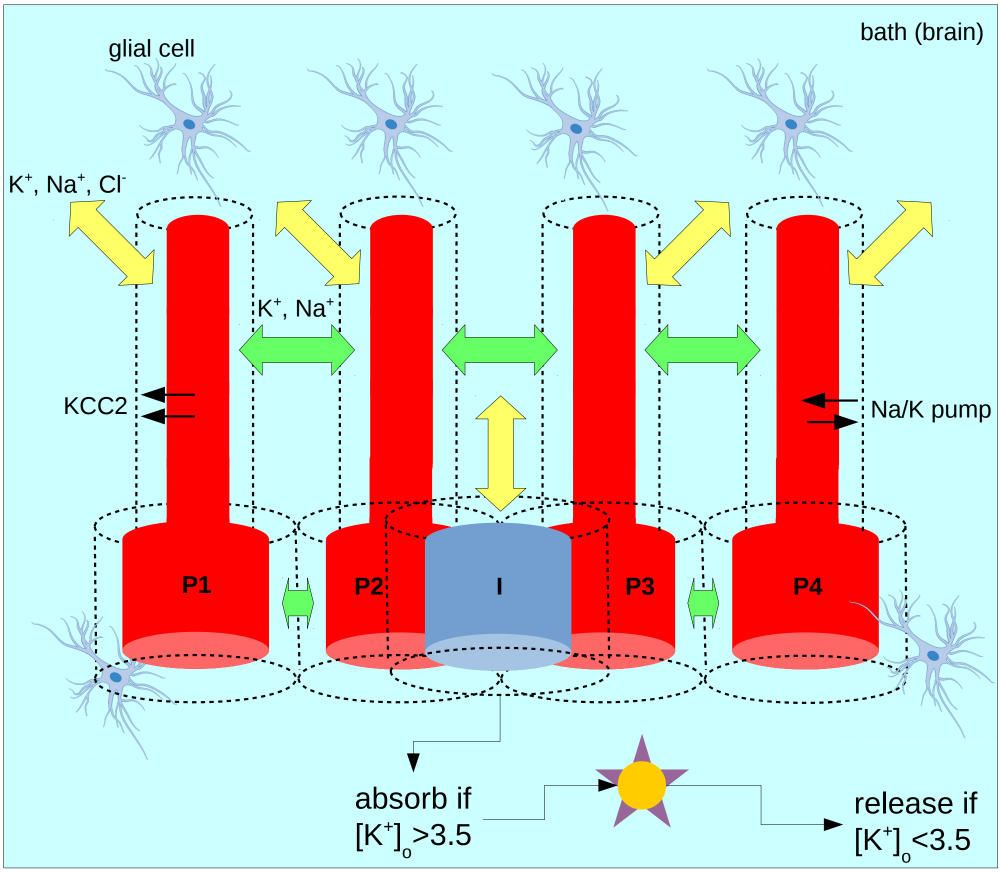

Figure 4.26: Modified model with the nanoparticle potassium buffer system. The artificial agent (purple and yellow starfish) activates and clears excessive potassium ions in each extracellular compartment when $[\mathrm{K}^+]_o$ is above the threshold value of 3.5 mM, and releases it otherwise.

ditional buffer component in all cells' external compartments, with activation threshold equal to the $[\mathrm{K}^+]_o$ baseline level (3.5 mM) and buffering speed of $k_{NANO} = 0.05$ mM/ms. The integrated extracellular potassium concentration dynamics reads:

$$\frac{d[\mathrm{K}^+]_o}{dt} = \frac{\sum I_K}{F \times V} - k_{NANO} \tag{4.30}$$

The modified model setup is illustrated in Fig. 4.26, where the nanoparticle agent is represented by the purple and yellow starfish.

Simulations results are shown in Fig. 4.27. The strong interneuronal firing (middle trace), that would normally cause the extracellular potassium increase and the subsequent pyramidal cells activation, fails here to trigger a seizure-like event; this is due to the enhanced $[\mathrm{K}^+]_o$ clearance action mediated by the nanoparticles. The extracellular potassium concentration trace (bottom panel) remains at its baseline level in pyramidal dendrites (red line), and slightly increases in somas (black) at seizure onset, but it is immediately depleted and mainatiend low by the artificial buffer. As a result, pyramidal cells (top panel) are not recruited into increased excitability, and exhibit only sporadic firing of single spikes when the inhibitory interneuron action diminishes. The introduction of the artificial $[\mathrm{K}^+]_o$ regulation mechanism led therefore to successful seizure control in the model. In reality, the hypothetical buffer here proposed would be able to recognize the potassium concentration level in the medium surrounding cells, absorb the K^+ ions in excess, and release them (up to an appropriate level) in the neuronal environment once normal brain functioning is restored. Nanoparticle therapies already exist as alternative means for drug and gene delivery, and their use as ion absorption components may be feasible in the future.

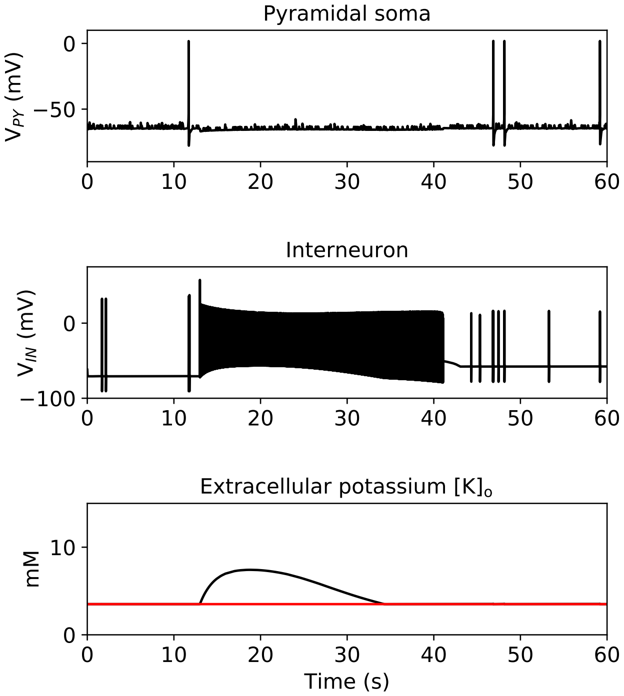

Figure 4.27: Simulation results of the model including the nanoparticle potassium clearance mechanism. Despite the strong interneuron discharge (middle panel), the extracellular potassium in the pyramidal dendrites (bottom panel, red line) remains equal to the baseline level, while in somas (black) it moderately increases, to be soon depleted by the artificial buffer. As a result, principal neurons (top) are subject to sole inhibition and do not develop epileptiform activity.

Chapter 5

Conclusions

The ultimate goal of this work is to elucidate the processes responsible for epileptic seizure dynamics (initiation, progression and termination) in the human brain by means of realistic computer simulations. Real human brain recordings are often corrupted by artifacts and noise. In addition, intracellular and ion concentrations data is impossible to record in humans. Accordingly, traces obtained by inducing ictal activity to the *in vitro* isolated guinea pig brain were used as a reference. This preparation, described in Chapter 2, exhaustively reproduces human focal epilepsy patterns, and allows the extraction of highly accurate voltage and ion concentrations data. To start with, a simplified *in silico* model consisting of just two neurons, one excitatory and one inhibitory, and ion concentration dynamics was implemented (Chapter 3); subsequently, the model was extended to a five-cells neuronal network and equipped with additional biolgical components to make the representation as close as possible to physical reality (Chapter 4). The following section discusses and summarizes the main findings which can be drawn from the analysis here conducted.

5.1 Discussion and summary

The "potassium accumulation hypothesis" suggests that focal seizures may be triggered and maintained by the rise of extracellular potassium [78]. It has been recently proposed that increase in $[\mathrm{K}^+]_o$ may be mediated by enhanced interneuronal firing [79]. This view overturns the traditional concept according to which epileptic seizures originate from the prevalence of excitation over inhibition, and is supported by a number of animal model studies (e.g. [28], [80], [81], [82], [83], [84] and [85]), as well as epileptic patients presurgical data ([86]). Computer simulations performed with either the simplified or the extended model confirm the idea that the leading role in epileptogenesis is indeed played by inhibitory cells. It is important to point out that, prior to this work, the link between elevated $[K^+]_o$ and seizure generation has been explored in several other computational models incorporating ion concentration dynamics, e.g. [27], [62], [87], [88], [89] and [90]. The approach to epileptogenesis in those studies is, however, different than the one adopted in the present models, where emphasis is put on the role of inhibition in seizure initiation. Accordingly in the models here described, network activity is triggered by a depolarizing current virtually injected into the interneuron. In other studies ictal activity arises instead from the direct stimulation of pyramidal cells ([87], [88], [62]) or from external modulation of the extracellular K^+ and oxygen concentrations ([27]). The models introduced in Chapter 3 and 4 prove that epileptic events originated by strong inhibitory activity can progress and terminate without receiving any additional external inputs on account of continuous feedback mechanisms between ion components and neuronal activity.

The analysis here presented points therefore to the importance of non-synaptic mechanisms in epilepsy, especially ion concentration dynamics. Notably, the model versions with constant ion concentrations fail in reproducing the experimental results (Fig. 3.11 and 4.24), and show that changes in ion concentrations are an essential physiological mechanism of seizure generation. This reinforces the concept that seizure initiation, maintenance and termination are causally related to ion concentration changes, and confirms that realistic models of epilepsy aiming to explain the complex interactions between neurons under pathophysiological conditions should incorporate ion fluctuations. Furthermore, simulations run with the model described in Chapter 4 reveal the specific function played by K^+, Cl^- and Na^+ ions throughout the seizure-like event. The intense interneuron activity during the preictal period builds up the extracellular potassium and intracellular chloride concentrations in pyramidal cells (Fig. 4.10B). Elevated $[K^+]_o$ makes the K^+ reversal potential approach the cells membrane voltage, which weakens hyperpolarizing potassium currents and depolarizes the neurons; higher $[Cl^-]_i$ enhances neuronal excitability by acting on the hyperpolarizig Cl^- leak current, the $GABA_A$ reversal potential and the KCC2 cotransporter (see Section 4.10.1). K^+ and Cl^- ions are therefore responsible for both the onset of the seizure fast spiking phase and its maintenance in principal neurons. Intracellular Na^+ concentration changes, on the other hand, are a key factor for seizure termination. When $[Na^+]_i$ increases in principal cells in the late phase of the seizure, the Na^+-K^+ pump action is reinforced; since the pump current is hyperpolarizing the ictal event eventually sets off (see Section 4.10.4). This result is compatible with the experimental hypothesis advanced by Jensen et al. in [91] that progressive accumulation of Na^+ in intracellular regions leads to neuronal firing extinction, and it is also aligned with the findings of other computational studies, such as those discussed in [26], [92] and [93]. Jensen's hypothesis has never been directly tested experimentally, but it has been shown by Haas and Jefferys that reduction of oxygen flow, which diminishes pump activity, can prolong ictal discharges ([11]). Nevertheless, various other mechanisms have been suggested to contribute to seizure termination, e.g. acidosis, glutamate depletion, increased network synchrony and release of adenosine. On the whole, it is likely that multiple ion, synaptic and neuronal components cooperate to bring seizures to an end [94].

The power of computer models relies not only on their ability to faithfully reproduce experimental data, but also on offering researchers virtual replicas of the experiment which are not subject to the limitations imposed by reality, and can thus be freely manipulated. In the context of computational neuroscience, such reproductions may be used to assess the contributions of single processes to network behaviour, study the consequences of neurobiological components alteration, validate model predictions by comparing simulations with animal or human brain recordings, and test new therapeutic strategies to tackle neurological disorders. All these possibilities have been explored throughout this work. In Section 3.6.2 simulations reveal the very fine balance existing between potassium release, uptake and diffusion: the resulting $[K^+]_o$ trace can be split into the sum of its parts making possible the identification of the predominant components at play. The investigation shows that in the simplified model diffusive processes are the main extracellular K^+ clearance agent. The selective removal of physiological elements from the models, analyzed in Sections 3.6.3 and 4.10.5, enables to assess the relevance of single mechanisms to specific behaviors and to predict the consequences of hampered functions. For example, excluding the glial cells buffering action (Fig. 3.8) would result in a permanent depolarization block caused by excessive extracellular potassium accumulation. In Section 4.10.4 a novel hypothesis of seizure termination mechanism has been described. It has not been directly tested experimentally, and the modeling results may contribute to the design of new experiments. In Section 4.10.6 it has been shown that in the extended model the bursting frequency decays exponentially. This feature was not originally implemented and manifested spontaneously as a product of the interaction between the simulated neurobiological components. Interestingly, the exponential pattern is confirmed by both *in vitro* and human data. Finally, with the insight that high $[K^+]_o$ is related to seizures occurrence, the models can be used to test if the addition of a fictitious potassium clearence component, which may be recreated employing nanoparticles, can prevent the development of epileptic events. The postulate has been demonstrated adapting the approach followed by Suffczynski et al. in [95] to the extended model, as described in Section 4.10.7.

In conclusion, the main results of this thesis can be summarized as follows:

- The computer models in Chapter 3 and 4 validate the “potassium accumulation hypothesis” and support the new view on epileptogenesis focusing on the relevance of inhibitory networks.

- Ion concentration dynamics is of pivotal importance for epileptic modeling and should be included in computational representations, as demonstrated by both model versions.

- Simulations run with the model in Chapter 4 point to the specific function of K^+, Cl^- and Na^+ ions in epilepsy. In particular:

  ✓ extracellular K^+ and intracellular Cl^- are directly associated to seizure initiation;

- ✓ extracellular K^+ is important for seizure maintenance, and the transition from tonic firing to bursting is made possible by the interplay of K^+ and Na^+ currents;
- ✓ intracellular Na^+ in pyramidal cells is linked to seizure termination via its influence on the Na^+-K^+ pump action.

5.2 Model limitations and future developments

Notwithstanding the fact that the computational models presented in this work can reproduce many features observed in the whole guinea pig brain *in vitro* during induced seizures, simulations are unavoidably based on simplifications of the real system. In the first place, for the sake of calculation efficiency the extended neuronal network consists of a relatively small number of neurons, just five. It might be surprising that such a simplified model is actually able to recreate pathophysiological behaviors strongly resemblant those observed in real cells. This can be justified by the observation that during epileptic events large populations of neurons synchronize, and therefore the network patterns can be appropriately captured even by a few representative units. Nevertheless, in order to reduce the gap between simulation layer and reality, future model implementations might consider the incorporation of a higher number of inhibitory and excitatory cells.

Another issue is related to network stability in the absence of stimulation. Both in the minimal and extended model, cells' membrane potential and ion concentrations are not exactly stable at rest, and small deviations from the equilibrium conditions due to ion pumps, leak and cotransporter currents, and diffusion mechanisms are observed. From the structural point of view, the lack of absolute stability could not be systematically avoided, and derives from the need to choose certain parameter values over others to correctly reproduce the experimental data, but which do not necessarily ensure global balance among the totality of model components.

With the aim of recreating the enhanced firing of inhibitory cells observed experimentally at seizure onset, the interneuron is artificially stimulated by the injection of a depolarizing current. In real systems, seizures occur either spontaneously or as a consequence of proconvulsant drugs application. The true mechanisms leading to the reinforcement of inhibitory activity at the transition from normal brain function to epileptic behavior are not known, but might be related to network phenomena and can be investigated in future model versions.

In addition to concentration gradients, diffusing ions in the brain are also subject to electrostatic forces and their movement is described by the Nernst-Planck equation. The pre-implemented diffusion equation in the NEURON simulator is, however, based on the Fick's first law and assumes that electric potential differences in the extra- or intracellular space are ignorable compared to concentration gradients. Although this approximation is worth mentioning, as explained in Chapter 3 and based on [52], neglecting ion electrostatic drift should not have severe consequences on the simulation results, especially under conditions of intense neuronal activity.

It has been recently shown that epileptiform activity in the hippocampus can spread without chemical or electric synaptic transmission, at a propagation speed not compatible with ion diffusion [15]. Computer simulations revealed that this may be due to electric field transmission, which also contributes to neuronal activity synchronization. Cell communication via electric fields is not implemented in the models presented in the thesis. Even though during seizure initiation this mechanism is likely not to play a dominant role, it may significantly influence seizure progression and termination. Further model developments might therefore benefit from the inclusion of electric field transmission.

Finally, the question remains open whether the present study can actually provide insight into the mechanisms of seizure generation in genuine *in vivo* conditions, or even in human epilepsy. The experimental seizure patterns here considered closely resemble those recorded in human temporal lobe epilepsy, suggesting that ion concentrations changes may also play a critical role in real patients' seizures. In particular, it has been shown that seizures in temporal lobe epilepsy patients are initiated with increased firing of inhibitory cells ([86]). Additionally, the prediction generated by the extended model regarding the IBI time evolution was confirmed experimentally, increasing confidence in the model results. In summary, despite model limitations, the similarity shared by simulation results and experimental data is a strength of this study, and shows how integrating highly reliable *in vitro* recordings with realistic computer simulations may ultimately lead to new insights in understanding how seizures start, evolve and terminate.

List of author's papers

[1] Damiano Gentiletti, Marco de Curtis, Vadym Gnatkovsky, and Piotr Suffczynski. Modeling of seizure transitions with ion concentration dynamics. *BMC Neuroscience*, 16(S1), P242, Dec 2015. doi: 10.1186/1471-2202-16-s1-p242.

[2] Piotr Suffczynski, Damiano Gentiletti, Vadym Gnatkovsky, and Marco de Curtis. Extracellular potassium and focal seizures – insight from in silico study. In Amy Cochran Peter Erdi, Basabdatta Sen Bhattacharya, editor, *Computational Neurology and Psychiatry*, volume 6 of *Springer Series in Bio-/Neuroinformatics*, pages 49–72. Springer International Publishing, 2017. doi: 10.1007/978-3-319-49959-8_3.

[3] D. Gentiletti, P. Suffczynski, V. Gnatkovsky, and M. de Curtis. Changes of Ionic Concentrations During Seizure Transitions – A Modeling Study. *Int J Neural Syst*, 27(4):1750004, Jun 2017. doi: 10.1142/S0129065717500046.

[4] Damiano Gentiletti, Piotr Suffczynski, Vadym Gnatkovski, and Marco De Curtis. Mechanisms of focal seizure generation in a realistic small-network model with ionic dynamics. *BMC Neuroscience*, 18(S1):P45, Aug 2017.

[5] Damiano Gentiletti, Marco de Curtis, Vadym Gnatkovsky, and Piotr Suffczynski. Focal seizures are organized by feedback between neural activity and ion concentration changes. *bioRxiv* 2021.03.18.435995, 2021. doi: 10.1101/2021.03.18.435995.

Bibliography

[1] R. S. Fisher, W. van Emde Boas, W. Blume, C. Elger, P. Genton, P. Lee, and J. Engel. Epileptic seizures and epilepsy: definitions proposed by the International League Against Epilepsy (ILAE) and the International Bureau for Epilepsy (IBE). *Epilepsia*, 46(4):470–472, Apr 2005.

[2] E. Magiorkinis, K. Sidiropoulou, and A. Diamantis. Hallmarks in the history of epilepsy: epilepsy in antiquity. *Epilepsy Behav*, 17(1):103–108, Jan 2010.

[3] D. G. Hirtz, D. J. Thuman, J. Lee, K. Gwinn-Hardy, S. C. Hong, M. Mohamed, A. R. Chaudhuri, and R. Zalutsky. How Common Are the "Common" Neurologic Disorders? *Neurology*, 68(5)(326–37), 2007.

[4] M. J. Eadie. Shortcomings in the current treatment of epilepsy. *Expert Rev Neurother*, 12(12):1419–1427, Dec 2012.

[5] W. Truccolo, J. A. Donoghue, L. R. Hochberg, E. N. Eskandar, J. R. Madsen, W. S. Anderson, E. N. Brown, E. Halgren, and S. S. Cash. Single-neuron dynamics in human focal epilepsy. *Nat. Neurosci.*, 14(5):635–641, May 2011.

[6] J. G. R. Jefferys, P. Jiruska, M. de Curtis, and Avoli M. Limbic network synchronization and temporal lobe epilepsy. *Jasper's basic mechanisms of the epilepsies*, pages 176–286, 2012.

[7] R. Tatti, M. S. Haley, O. K. Swanson, T. Tselha, and A. Maffei. Neurophysiology and regulation of the balance between excitation and inhibition in neocortical circuits. *Biological Psychiatry*, 81(10):821–831, May 2017.

[8] J. G. Jefferys and H. L. Haas. Synchronized bursting of CA1 hippocampal pyramidal cells in the absence of synaptic transmission. *Nature*, 300(5891):448–450, Dec 1982.

[9] A. Konnerth, U. Heinemann, and Y. Yaari. Nonsynaptic epileptogenesis in the mammalian hippocampus in vitro. I. Development of seizurelike activity in low extracellular calcium. *J. Neurophysiol.*, 56(2):409–423, Aug 1986.

[10] M. S. Jensen and Y. Yaari. The relationship between interictal and ictal paroxysms in an in vitro model of focal hippocampal epilepsy. *Ann. Neurol.*, 24(5):591–598, Nov 1988.

[11] H. L. Haas and J. G. Jefferys. Low-calcium field burst discharges of CA1 pyramidal neurones in rat hippocampal slices. *J. Physiol. (Lond.)*, 354:185–201, Sep 1984.

[12] D. Johnston and S. M. S. Wu. Foundations of Cellular Neurophysiology. *The MIT Press*, 1995.

[13] D. M. Durand, E. H. Park, and A. L. Jensen. Potassium diffusive coupling in neural networks. *Philos. Trans. R. Soc. Lond., B, Biol. Sci.*, 365(1551):2347–2362, Aug 2010.

[14] D. Aur and M. S. Jog. Neuroelectrodynamics: Understanding the brain language. *IOS Press*, 74:1–235, 2010.

[15] M. Zhang, T. P. Ladas, C. Qiu, R. S. Shivacharan, L. E. Gonzalez-Reyes, and D. M. Durand. Propagation of epileptiform activity can be independent of synaptic transmission, gap junctions, or diffusion and is consistent with electrical field transmission. *J. Neurosci.*, 34(4):1409–1419, Jan 2014.

[16] A. L. HODGKIN and A. F. HUXLEY. A quantitative description of membrane current and its application to conduction and excitation in nerve. *J. Physiol. (Lond.)*, 117(4):500–544, Aug 1952.

[17] R. D. Traub, J. G. Jefferys, R. Miles, M. A. Whittington, and K. Toth. A branching dendritic model of a rodent CA3 pyramidal neurone. *J. Physiol. (Lond.)*, 481 (Pt 1):79–95, Nov 1994.

[18] M. Baszczak and S. Kasicki. A single compartment neuron model with activity-dependent conductances during NMDA induced activity. *Acta Neurobiol Exp (Wars)*, 65(2):183–190, 2005.

[19] B. H. Jansen and V. G. Rit. Electroencephalogram and visual evoked potential generation in a mathematical model of coupled cortical columns. *Biol Cybern*, 73(4):357–366, Sep 1995.

[20] W. W. Lytton. Computer modelling of epilepsy. *Nat. Rev. Neurosci.*, 9(8):626–637, Aug 2008.

[21] J. V. Raimondo, R. J. Burman, A. A. Katz, and C. J. Akerman. Ion dynamics during seizures. *Front Cell Neurosci*, 9:419, 2015.

[22] F. Frohlich, M. Bazhenov, V. Iragui-Madoz, and T. J. Sejnowski. Potassium dynamics in the epileptic cortex: new insights on an old topic. *Neuroscientist*, 14(5):422–433, Oct 2008.

[23] A. P. Fertziger and J. B. Ranck. Potassium accumulation in interstitial space during epileptiform seizures. *Exp. Neurol.*, 26(3):571–585, Mar 1970.

[24] E. H. Park and D. M. Durand. Role of potassium lateral diffusion in non-synaptic epilepsy: a computational study. *J. Theor. Biol.*, 238(3):666–682, Feb 2006.

[25] G. G. Somjen, H. Kager, and W. J. Wadman. Computer simulations of neuron-glia interactions mediated by ion flux. *J Comput Neurosci*, 25(2):349–365, Oct 2008.

[26] G. P. Krishnan and M. Bazhenov. Ionic dynamics mediate spontaneous termination of seizures and postictal depression state. *J. Neurosci.*, 31(24):8870–8882, Jun 2011.

[27] Y. Wei, G. Ullah, and S. J. Schiff. Unification of neuronal spikes, seizures, and spreading depression. *J. Neurosci.*, 34(35):11733–11743, Aug 2014.

[28] V. Gnatkovsky, L. Librizzi, F. Trombin, and M. de Curtis. Fast activity at seizure onset is mediated by inhibitory circuits in the entorhinal cortex in vitro. *Ann. Neurol.*, 64(6):674–686, Dec 2008.

[29] G. G. Somjen. Ions in the Brain: Normal Function, Seizures, and Stroke. *Oxford University Press, USA*, 2004.

[30] M. J. Bezaire and I. Soltesz. Quantitative assessment of CA1 local circuits: knowledge base for interneuron-pyramidal cell connectivity. *Hippocampus*, 23(9):751–785, Sep 2013.

[31] M. de Curtis, A. Manfridi, and G. Biella. Activity-dependent pH shifts and periodic recurrence of spontaneous interictal spikes in a model of focal epileptogenesis. *J. Neurosci.*, 18(18):7543–7551, Sep 1998.

[32] L. Uva, L. Librizzi, F. Wendling, and M. de Curtis. Propagation dynamics of epileptiform activity acutely induced by bicuculline in the hippocampal-parahippocampal region of the isolated Guinea pig brain. *Epilepsia*, 46(12):1914–1925, Dec 2005.

[33] M. de Curtis, D. Pare, and R. R. Llinas. The electrophysiology of the olfactory-hippocampal circuit in the isolated and perfused adult mammalian brain in vitro. *Hippocampus*, 1(4):341–354, Oct 1991.

[34] M. de Curtis, G. Biella, C. Buccellati, and G. Folco. Simultaneous investigation of the neuronal and vascular compartments in the guinea pig brain isolated in vitro. *Brain Res. Brain Res. Protoc.*, 3(2):221–228, Nov 1998.

[35] M. Muhlethaler, M. de Curtis, K. Walton, and R. Llinas. The isolated and perfused brain of the guinea-pig in vitro. *Eur. J. Neurosci.*, 5(7):915–926, Jul 1993.

[36] F. Trombin, V. Gnatkovsky, and M. de Curtis. Changes in action potential features during focal seizure discharges in the entorhinal cortex of the in

vitro isolated guinea pig brain. *J. Neurophysiol.*, 106(3):1411–1423, Sep 2011.

[37] L. Uva, S. Saccucci, M. Chikhladze, L. Tassi, V. Gnatkovsky, G. Milesi, M. Morbin, and M. De Curtis. A Novel Focal Seizure Pattern Generated in Superficial Layers of the Olfactory Cortex. *J. Neurosci.*, 37(13):3544–3554, Mar 2017.

[38] M. de Curtis and V. Gnatkovsky. Reevaluating the mechanisms of focal ictogenesis: The role of low-voltage fast activity. *Epilepsia*, 50(12):2514–2525, Dec 2009.

[39] E. Fransen, A. A. Alonso, and M. E. Hasselmo. Simulations of the role of the muscarinic-activated calcium-sensitive nonspecific cation current INCM in entorhinal neuronal activity during delayed matching tasks. *J. Neurosci.*, 22(3):1081–1097, Feb 2002.

[40] W. Rall. Branching dendritic trees and motoneuron membrane resistivity. *Exp. Neurol.*, 1:491–527, Nov 1959.

[41] J. A. Payne, C. Rivera, J. Voipio, and K. Kaila. Cation-chloride co-transporters in neuronal communication, development and trauma. *Trends Neurosci.*, 26(4):199–206, Apr 2003.

[42] J. Voipio, M. Pasternack, B. Rydqvist, and K. Kaila. Effect of gamma-aminobutyric acid on intracellular pH in the crayfish stretch-receptor neurone. *J. Exp. Biol.*, 156:349–360, Mar 1991.

[43] N. Doyon, S. A. Prescott, A. Castonguay, A. G. Godin, H. Kroger, and Y. De Koninck. Efficacy of synaptic inhibition depends on multiple, dynamically interacting mechanisms implicated in chloride homeostasis. *PLoS Comput. Biol.*, 7(9):e1002149, Sep 2011.

[44] H. Kager, W. J. Wadman, and G. G. Somjen. Simulated seizures and spreading depression in a neuron model incorporating interstitial space and ion concentrations. *J. Neurophysiol.*, 84(1):495–512, Jul 2000.

[45] M. Roberts, M. Reiss, and G. Monger. Advanced Biology. *Nelson Thornes, England*, 2000.

[46] H. Kager, W. J. Wadman, and G. G. Somjen. Seizure-like afterdischarges simulated in a model neuron. *J Comput Neurosci*, 22(2):105–128, Apr 2007.

[47] P. K. Lauf and N. C. Adragna. K-Cl cotransport: properties and molecular mechanism. *Cell. Physiol. Biochem.*, 10(5-6):341–354, 2000.

[48] N. T. Carnevale and M. L. Hines. The NEURON Book. *Cambridge, UK: Cambridge University Press*, 2004.

[49] D. Gentiletti, P. Suffczynski, V. Gnatkovsky, and M. de Curtis. Changes of Ionic Concentrations During Seizure Transitions – A Modeling Study. *Int J Neural Syst*, 27(4):1750004, Jun 2017. doi: 10.1142/S0129065717500046.

[50] W. H. Nernst. Zur Kinetik der Lösung befindlichen Körper: Theorie der Diffusion. *Z. Phys. Chem.*, 3:613–37, 1888.

[51] B. J. Kirby. Micro- and Nanoscale Fluid Mechanics: Transport in Microfluidic Devices. *Cambridge University Press*, 2010. Chapter 11: Species and Charge Transport.

[52] G. Halnes, I. Ostby, K. H. Pettersen, S. W. Omholt, and G. T. Einevoll. Electrodiffusive model for astrocytic and neuronal ion concentration dynamics. *PLoS Comput. Biol.*, 9(12):e1003386, 2013.

[53] M. G. Kozoriz, D. C. Bates, S. R. Bond, C. P. Lai, and D. M. Moniz. Passing potassium with and without gap junctions. *J. Neurosci.*, 26(31):8023–8024, Aug 2006.

[54] K. C. Chen and C. Nicholson. Spatial buffering of potassium ions in brain extracellular space. *Biophys. J.*, 78(6):2776–2797, Jun 2000.

[55] Z. Q. Xiong and J. L. Stringer. Sodium pump activity, not glial spatial buffering, clears potassium after epileptiform activity induced in the dentate gyrus. *J. Neurophysiol.*, 83(3):1443–1451, Mar 2000.

[56] P. L. Nunez and R. Srinivasan. Electric Fields of the Brain: The Neurophysics of EEG. *Oxford University Press*, page 122, 2006.

[57] S. B. Hladky and M. A. Barrand. Fluid and ion transfer across the blood-brain and blood-cerebrospinal fluid barriers; a comparative account of mechanisms and roles. *Fluids Barriers CNS*, 13(1):19, Oct 2016.

[58] T. Olsson, M. Broberg, K. J. Pope, A. Wallace, L. Mackenzie, F. Blomstrand, M. Nilsson, and J. O. Willoughby. Cell swelling, seizures and spreading depression: an impedance study. *Neuroscience*, 140(2):505–515, Jun 2006.

[59] I. Dietzel, U. Heinemann, G. Hofmeier, and H. D. Lux. Transient changes in the size of the extracellular space in the sensorimotor cortex of cats in relation to stimulus-induced changes in potassium concentration. *Exp Brain Res*, 40(4):432–439, 1980.

[60] I. Dietzel, U. Heinemann, G. Hofmeier, and H. D. Lux. Stimulus-induced changes in extracellular Na+ and Cl- concentration in relation to changes in the size of the extracellular space. *Exp Brain Res*, 46(1):73–84, 1982.

[61] Z. J. Zhang, J. Koifman, D. S. Shin, H. Ye, C. M. Florez, L. Zhang, T. A. Valiante, and P. L. Carlen. Transition to seizure: ictal discharge is preceded by exhausted presynaptic GABA release in the hippocampal CA3 region. *J. Neurosci.*, 32(7):2499–2512, Feb 2012.

[62] H. Kager, W. J. Wadman, and G. G. Somjen. Conditions for the triggering of spreading depression studied with computer simulations. *J. Neurophysiol.*, 88(5):2700–2712, Nov 2002.

[63] C. J. McBain, S. F. Traynelis, and R. Dingledine. Regional variation of extracellular space in the hippocampus. *Science*, 249(4969):674–677, 1990.

[64] Damiano Gentiletti, Marco de Curtis, Vadym Gnatkovsky, and Piotr Suffczynski. Focal seizures are organized by feedback between neural activity and ion concentration changes. *bioRxiv* 2021.03.18.435995, 2021. doi: 10.1101/2021.03.18.435995.

[65] Borgdorff A. J. *Calcium dynamics in hippocampal neurones.* PhD thesis, University of Amsterdam, 2002.

[66] R. D. Andrew and B. A. MacVicar. Imaging cell volume changes and neuronal excitation in the hippocampal slice. *Neuroscience*, 62(2):371–383, Sep 1994.

[67] R. D. Fields. Signaling by neuronal swelling. *Sci Signal*, 4(155):tr1, Jan 2011.

[68] B. C. Hill, E. D. Schubert, M. A. Nokes, and R. P. Michelson. Laser interferometer measurement of changes in crayfish axon diameter concurrent with action potential. *Science*, 196(4288):426–428, Apr 1977.

[69] K. Iwasa, I. Tasaki, and R. C. Gibbons. Swelling of nerve fibers associated with action potentials. *Science*, 210(4467):338–339, Oct 1980.

[70] N. Hubel and G. Ullah. Anions Govern Cell Volume: A Case Study of Relative Astrocytic and Neuronal Swelling in Spreading Depolarization. *PLoS ONE*, 11(3):e0147060, 2016.

[71] T. Mazel, F. Richter, L. Vargova, and E. Sykova. Changes in extracellular space volume and geometry induced by cortical spreading depression in immature and adult rats. *Physiol Res*, 51 Suppl 1:85–93, 2002.

[72] H. Linden, E. Hagen, S. Leski, E. S. Norheim, K. H. Pettersen, and G. T. Einevoll. Lfpy: a tool for biophysical simulation of extracellular potentials generated by detailed model neurons. *Frontiers in Neuroinformatics*, 7(41), 2014.

[73] E. M. Izhikevich. Dynamical Systems in Neuroscience - The Geometry of Excitability and Bursting. *The MIT Press*, 2007.

[74] R. Mohanraj and M. J. Brodie. Outcomes in newly diagnosed localization-related epilepsies. *Seizure*, 14(5):318–323, Jul 2005.

[75] W. Loscher and D. Schmidt. Modern antiepileptic drug development has failed to deliver: ways out of the current dilemma. *Epilepsia*, 52(4):657–678, Apr 2011.

[76] Laura De Matteis, Rafael Martín-Rapún, and Jesús M. de la Fuente. Nanotechnology in personalized medicine: A promising tool for alzheimer's disease treatment. *Current Medicinal Chemistry*, 25(35):4602–4615, December 2018.

[77] N. Sanvicens and M. P. Marco. Multifunctional nanoparticles–properties and prospects for their use in human medicine. *Trends Biotechnol.*, 26(8):425–433, Aug 2008.

[78] Allen P. Fertziger and James B. Ranck. Potassium accumulation in interstitial space during epileptiform seizures. *Experimental Neurology*, 26(3):571–585, March 1970.

[79] Marco de Curtis and Massimo Avoli. GABAergic networks jump-start focal seizures. *Epilepsia*, 57(5):679–687, April 2016.

[80] D. W. Grasse, S. Karunakaran, and K. A. Moxon. Neuronal synchrony and the transition to spontaneous seizures. *Experimental Neurology*, 248:72–84, October 2013.

[81] M. Lévesque, R. Herrington, S. Hamidi, and M. Avoli. Interneurons spark seizure-like activity in the entorhinal cortex. *Neurobiology of Disease*, 87:91–101, March 2016.

[82] V. Lopantsev and M. Avoli. Participation of GABAA-mediated inhibition in ictallike discharges in the rat entorhinal cortex. *Journal of Neurophysiology*, 79(1):352–360, January 1998.

[83] M. L. Miri, M. Vinck, R. Pant, and J. A. Cardin. Altered hippocampal interneuron activity precedes ictal onset. *eLife*, 7, November 2018.

[84] I. Toyoda, S. Fujita, A. K. Thamattoor, and P. S. Buckmaster. Unit activity of hippocampal interneurons before spontaneous seizures in an animal

model of temporal lobe epilepsy. *Journal of Neuroscience*, 35(16):6600–6618, April 2015.

[85] J. Ziburkus, J. R. Cressman, E. Barreto, and S. J. Schiff. Interneuron and pyramidal cell interplay during in vitro seizure-like events. *Journal of Neurophysiology*, 95(6):3948–3954, June 2006.

[86] B. Elahian, N. E. Lado, E. Mankin, S. Vangala, A. Misra, K. Moxon, I. Fried, A. Sharan, M. Yeasin, R. Staba, R. Bragin, M. Avoli, M. R. Sperling, J. Engel, and S. A. Weiss. Low-voltage fast seizures in humans begin with increased interneuron firing. *Annals of Neurology*, 84(4):588–600, October 2018.

[87] M. Bazhenov, I. Timofeev, M. Steriade, and T. J. Sejnowski. Potassium model for slow (2-3 Hz) in vivo neocortical paroxysmal oscillations. *J. Neurophysiol.*, 92(2):1116–1132, Aug 2004.

[88] A. Buchin, A. Chizhov, G. Huberfeld, R. Miles, and B. S. Gutkin. Reduced efficacy of the KCC2 cotransporter promotes epileptic oscillations in a subiculum network model. *The Journal of Neuroscience*, 36(46):11619–11633, November 2016.

[89] F. Frohlich, M. Bazhenov, I. Timofeev, M. Steriade, and T. J. Sejnowski. Slow state transitions of sustained neural oscillations by activity-dependent modulation of intrinsic excitability. *Journal of Neuroscience*, 26(23):6153–6162, June 2006.

[90] E. C. Y. Ho and W. Truccolo. Interaction between synaptic inhibition and glial-potassium dynamics leads to diverse seizure transition modes in biophysical models of human focal seizures. *Journal of Computational Neuroscience*, 41(2):225–244, August 2016.

[91] M. S. Jensen and Y. Yaari. Role of intrinsic burst firing, potassium accumulation, and electrical coupling in the elevated potassium model of hippocampal epilepsy. *Journal of Neurophysiology*, 77(3):1224–1233, March 1997.

[92] G. P. Krishnan, G. Filatov, A. Shilnikov, and M. Bazhenov. Electrogenic properties of the na+/k+ atpase control transitions between normal and pathological brain states. *Journal of Neurophysiology*, 113(9):3356–3374, May 2015.

[93] A. V. Chizhov, A. V. Zefirov, D. V. Amakhin, E. Y. Smirnova, and A. V. Zaitsev. Minimal model of interictal and ictal discharges “epileptor-2”. *PLOS Computational Biology*, 14(5):e1006186, May 2018.

[94] Fred A. Lado and Solomon L. Moshé. How do seizures stop? *Epilepsia*, 49(10):1651–1664, October 2008.

[95] Piotr Suffczynski, Damiano Gentiletti, Vadym Gnatkovsky, and Marco de Curtis. Extracellular potassium and focal seizures—insight from in silico study. In Amy Cochran Peter Erdi, Basabdatta Sen Bhattacharya, editor, *Computational Neurology and Psychiatry*, volume 6 of *Springer Series in Bio-/Neuroinformatics*, pages 49–72. Springer International Publishing, 2017. doi: 10.1007/978-3-319-49959-8_3.